A HYBRID APPROACH TO FLOODING AND DAMAGED SHIP DYNAMICS

by

Zhiliang Gao

A thesis submitted in fulfillment of the requirements for the degree of Doctor of Philosophy

Department of Naval Architecture and Marine Engineering

Universities of Glasgow and Strathclyde

May, 2012

Abstract

This thesis presents the development and application of a numerical tool that couples a Navier-Stokes (NS) solver and a seakeeping solver to study the behaviour of a damaged ship upon flooding.

Firstly, an NS solver that combines the volume of fluid (VOF) method with dynamic mesh techniques was developed to calculate the interactive dynamics of a damaged ship and floodwater. The VOF method was used to capture the fluid interface. The dynamic mesh techniques were employed to update the mesh following transient ship motions. To validate its performance in addressing complex free surface motion, the solver was firstly applied to several simple test cases including dam break, tank sloshing and compartment flooding. The benchmarking studies confirm that the present method is effective in solving free surface flow problems even with strong non-linearity. Then the solver was used to simulate the flooding process of a damaged barge which was fixed or freely floated in calm water. In comparison with the experimental data, both the ship and floodwater motions are well predicted by the present method.

Then, a hybrid method, which couples the present NS solver and another in-house seakeeping solver based on potential flow method, was developed to study damaged ship flooding in waves. The dynamics of water flooding and sloshing in the ship compartments were calculated by the NS solver, whereas the hydrodynamic forces induced by the sea on the external hull surface were calculated using the seakeeping solver. The hybrid approach was tested by simulating the roll decay of a damaged Ro-Ro ferry and free motion of the ferry in regular beam seas. Validation against experimental data shows that the proposed method ensures acceptable numerical

accuracy in flooding simulations while reducing the computational cost. In addition, the interactive dynamics of ship, sea wave, water flooding and sloshing were analyzed using the hybrid method.

In conclusion, the proposed hybrid method provides a reliable and efficient tool for analyzing flooding and damaged ship dynamics. Its application could assist in understanding of the intricate flooding mechanism that remains limited for ship researchers, designers and safety authorities.

Acknowledgements

I would like to express my deep gratitude to my supervisor, Professor Dracos Vassalos, for his academic support, guidance and constructive criticism throughout the course of my research. His help in financial support over the past four years is gratefully acknowledged.

I am especially thankful to my “unofficial” supervisor, Dr. Qiuxin Gao, for his continuous support, innumerable discussions and valuable suggestions towards my study as well as his sincere friendship brought in my daily life. My thanks also go to Dr. Andrzej Jasionowski for sharing his research code PROTEUS3 and allowing the progress of code integration. I sincerely thank Professor Osman Turan and Professor Alberto Francescutto for reviewing this thesis and providing many helpful suggestions for its improvement.

Many thanks are due to my colleagues in NAME and SSRC for making my life in Glasgow fruitful, joyful and rewarding, in particular to Mrs. Thelma Will and Mrs. Linda Mackay for the arrangement of administrative and financial matters.

I wish to thank Professor Zaojian Zou who was the supervisor of my master’s degree. He taught me how to acquire knowledge, how to work and how to be a decent man. His inculcation significantly influences the remaining part of my life.

Finally, I want to dedicate this thesis to my wife Yaling and our parents. I am quite sure that I could not have completed this work without their unconditional love, patient encouragement and sustained understanding during my stay abroad.

Table of Contents

List of Figures

List of Tables

Nomenclature

Abbreviations

2-D	two-dimensional
3-D	three-dimensional
4-DOF	four degrees of freedom
5-DOF	five degrees of freedom
6-DOF	six degrees of freedom
BS	body-fixed coordinate system
CN	Crank-Nicolson
CFD	computational fluid dynamics
CICSAM	compressive interface capturing scheme for arbitrary meshes
CD	central differencing
CV	control volume
FCT	flux corrected transport
FLAIR	flux line-segment model for advection and interface reconstruction
FV	finite volume
GMRES	generalized minimal residual
GS	global coordinate system
HPC	high performance computer
HRIC	high resolution interface capturing
ILUT	preconditioner of incomplete LU factorization with threshold
ITTC	international towing tank conference
LS	level set
MAC	marker and cell

MPI	message passing interface
NS	Naiver-Stokes
NVD	normalized variable diagram
OST	ortho-semi-torsional
PISO	pressure-implicit with splitting of operators
PLIC	piecewise linear interface calculation
RAO	roll response amplitude operator
RS	reference coordinate system
SCL	space conservation law
SIMPLE	semi-implicit method for pressure-linked equations
SIMPLEC	SIMPLE-consistent
SIMPLER	SIMPLE revised
SLIC	simple line interface calculation
SPH	smoothed particle hydrodynamics
TVD	total variational diminishing
UD	upwind differencing
VOF	volume of fluid

Roman Symbols

a_{nb}	off-diagonal coefficients of the discretised equation
a_q	diagonal coefficients of the discretised equation
$\boldsymbol{A}_f$	area vector of the CV face
A_{jk}	added mass
b	source term
B_{jk}	damping coefficient
Co_{lim}	limit of the cell Courant number
Co_q	cell Courant number
E_f	volumetric flux at the CV face

$\boldsymbol{F}$	resultant vector of external forces acting on the body
$\boldsymbol{F}_{\mathrm{B}}$	buoyancy force
$\boldsymbol{F}_{\mathrm{D}}$	diffraction force
$\boldsymbol{F}_{\mathrm{G}}$	gravitational force
$\boldsymbol{F}_{\mathrm{FK}}$	Froude-Krylov force
$\boldsymbol{F}_{\mathrm{R}}$	radiation force
$\boldsymbol{F}_{\mathrm{W}}$	internal liquid load
g	gravitational acceleration
G	centre of body mass
Im	imaginary part of the subsequent expression
$\boldsymbol{J}_G$	tensor of inertia moments of the body with respect to G described in the GS
$\boldsymbol{J}'_G$	tensor of inertia moments of the body with respect to G described in the BS
K_0	incident wave number
m	mass of the body
$\boldsymbol{M}_G$	resultant vector of external moments acting on the body with respect to G
$\boldsymbol{n}$	unit vector normal to S
n_j	generalized normal
P	pressure
Pe	Peclet number
$\boldsymbol{r}$	position vector of a point on S_B
$\boldsymbol{r}_G$	position vector of G
Re	real part of the subsequent expression
S	surface of CV
S_B	body surface
S_C	surface of floodable compartment
S_H	wetted surface of the hull
$\boldsymbol{T}_T$	transformation matrix from the BS to the GS
$\boldsymbol{u}$	fluid velocity vector

$\boldsymbol{u}_S$ velocity vector of CV face

U_0 mean forward speed of the ship

$\boldsymbol{U}_G$ velocity vector of G

V volume of CV

Greek Symbols

α fluid volume fraction

β Euler angle of rotation around Z-axis or yaw angle of the body

γ Euler angle of rotation around x-axis or roll angle of the body

θ Euler angle of rotation around y'-axis or pitch angle of the body

δt time step

δV change of CV volume

ϕ_{D} spatial potential of diffraction

ϕ_{I} spatial potential of incident wave

ϕ_{R} spatial potential of radiation

Φ_{D} diffraction potential

Φ_{I} incident wave potential

η_{I} elevation of incident wave

φ heading angle

μ effective viscosity

μ_1 viscosity of water

μ_2 viscosity of air

ρ effective density

ρ_1 density of water

ρ_2 density of air

σ phase angle of wave

ω encounter frequency

ω_0 circular frequency of incident wave

$\boldsymbol{\Omega}$	angular velocity vector of the body
χ	general variable
ξ_I	amplitude of incident wave
∇	gradient operator
Δ	Laplace operator

Chapter 1

Introduction

1.1 Background

The maritime tragedies that have occurred over the years (e.g., the losses of the *European Gateway* in 1980, *Herald of Free Enterprise* in 1987, *Estonia* in 1994, *Express Samina* in 2000, *al-Salam Boccaccio* 98 in 2006 and *Costa Concordia* in 2012, etc.) have motivated large-scale investigations into the survivability of damaged ships. The study within the European research project SAFEDOR (2005-2009) reveals that the risk to human life due to flooding is the dominant issue concerning safety in passenger ships. Although a clear understanding of the flooding dynamics of a damaged ship has long since been recognized as essential to establish proper life-saving measures and evacuation procedures, it remains limited for ship researchers, designers and safety authorities.

During the flooding process, a ship's motion affects water flooding and sloshing in its compartment; conversely, the liquid loads acting on the compartment also influence the motion of the ship. The method of using a model test to study this complex dynamic problem has the disadvantages of high expense, low efficiency and system errors, etc. On the other hand, numerical simulation of the coupled motion of damaged ship and floodwater is advancing rapidly. However, numerical tools developed so far normally neglect a number of effects (e.g., transient and non-linear effects of floodwater, geometry effect of damaged opening and compartment, etc.),

so they fail to predict the ship behaviour reliably for ships in a damaged condition. A high fidelity numerical tool to tackle the intricate flooding problem is required.

Over the past two decades, with improvements in the capabilities of high-performance computers (HPCs), the computational fluid dynamics (CFD) method has developed rapidly. With this method, all of the flow characteristics and parametric effects can be considered in the numerical simulation. In the areas of conventional ship hydrodynamics (i.e., resistance, propulsion, seakeeping and manoeuvring), the so-called numerical tank based on the CFD method has become an important supplement to the traditional model test. Therefore, applying CFD method to study the behaviour of damaged ships upon flooding is viable and promising.

Although CFD method can ensure high fidelity in the numerical simulation, its application to flooding is very time-consuming even with HPCs. The motivation of this work is to develop a numerical tool, which can capture more inherent phenomena while consuming relatively less computational resources, to study the flooding of a damaged ship. To pursue this aim, a Navier-Stokes (NS) solver is firstly developed to calculate the interactive dynamics of a damaged ship and floodwater. Then a hybrid method that couples the present NS solver and another in-house seakeeping solver is proposed to reduce the computational cost.

1.2 Thesis Outline

The remainder of the thesis is structured as follows:

Chapter 2: The principal aim and specific objectives of present research are stated.

Chapter 3: A report of literature review is presented.

Chapter 4: The elements of approach adopted in this research are outlined.

Chapter 5: An NS solver for the coupled simulation of flow and body motion is introduced. The governing equations of two-phase flow motion and rigid body motion are given first. Then the numerical method to solve the governing equations is detailed, involving discretisation formats, interpolation schemes, dynamic mesh strategy and solution procedure.

Chapter 6: A hybrid method that couples an NS solver and a seakeeping solver is introduced to solve the problem of a damaged ship flooding in waves, beginning with a description of mathematical model for the interactive dynamics between ship, wave and floodwater, followed by the numerical solution of this dynamic system with the proposed method.

Chapter 7: The developed NS solver is tested by solving three groups of non-linear free surface flow problems, including dam break, tank sloshing and compartment flooding. The time and grid dependence studies as well as the validation against other published results are performed.

Chapter 8: The developed NS solver is used to simulate two flooding scenarios of a damaged barge in the calm water. The barge is fixed and freely movable in the two scenarios, respectively. The results of benchmarking study are given.

Chapter 9: The proposed hybrid method is applied to the flooding of a damaged Ro-Ro ferry. The roll decay of the ferry and free motion of the ferry in regular beam seas are simulated, respectively. The comparisons between computed results and experimental data are given. Moreover, the coupled dynamics of ship, sea wave, water sloshing and flooding are analyzed.

Chapter 10: The thesis is summarized. The main contributions of present work and suggestions for future work are given.

Chapter 11: The main conclusions derived from the thesis are drawn.

Chapter 2

Aim of Research

The main aim of this research work is to develop a numerical tool with sufficient accuracy and efficiency to study flooding and damaged ship dynamics. The specific objectives are listed as follows:

1) Development of an NS solver with a free-surface-capturing scheme to accurately calculate the floodwater dynamics.

2) Extension of the two-phase flow NS solver to include the motion of a rigid body with six degrees of freedom (6-DOF), in order to effectively predict the interactive dynamics between floodwater and a damaged ship.

3) Integration of the present NS solver and an in-house seakeeping solver to improve computational efficiency for solving damaged ship flooding in waves.

4) Verification and validation of the newly developed solvers.

5) Application of the developed solver to study the interactive influences between ship behaviour, sea wave, damaged opening, compartment's internal layout and floodwater motion.

Chapter 3

Literature Review

In this chapter, a critical review of the previous related studies in the subject of damaged ship flooding is presented, aiming to identify the capabilities and limitations of the previous mathematical models in dealing with the subject.

3.1 Studies Based on Conventional Method

Numerical studies on the dynamic behaviour of a damaged ship upon flooding have been conducted since the 1980s by different research groups, aiming to analyze the cause of some major accidents, to comprehend the behaviour of damaged ship in different sea states, to determine the survivability boundary of new designs or to investigate the effect of parameters on the damage survivability.

Spouge (1986) investigated the capsizing of the *European Gateway* by numerical simulation. In his simulation program, the sea surface was assumed to be calm. The flow rates through the opening were calculated by the relative head of water and were integrated to give the water volume in each compartment, where the inflowing water was assumed to settle to an equilibrium surface. The ship was considered to be in static equilibrium at each time step. Its equilibrium heel angle for the current time step was interpolated according to the heeling and righting moments which were calculated for each assumed heel angle. The phenomenon of transient asymmetric flooding (first introduced by Spouge) was accounted for by using a semi-empirical

offset of the gravitational centre of floodwater. Dand (1989) used the same simulation program to study the loss of the *Herald of Free Enterprise*. Sen and Konstantinidis (1987) used a similar numerical model to study the survival potential of a damaged Ro-Ro cargo vessel.

Vredeveldt and Journée (1991) combined a hydraulic flow model with the dynamic roll motion of the ship to study damaged ship's behaviour in calm water due to sudden water ingress. In their studies, the Bernoulli's equation with a pressure loss coefficient was used to calculate the flow rates through the damaged opening. The motion of water inside the compartments was ignored. The ship's roll motion was determined by solving the simplified dynamic roll motion equation in which the roll damping was evaluated by the Ikeda's semi-empirical method, whereas the heave and trim motions were considered to be quasi-stationary. A similar approach was later used in Xia et al. (1999) to study the cross-flooding and the resulting dynamic roll motion of a Ro-Ro ship. In both cases, the air compression was taken into account.

Santos et al. (2002) applied a 6-DOF mathematical model to the transient asymmetric flooding of the *European Gateway* in calm water. The ship motions were computed using a set of six nonlinear coupled equations of motion with time dependent coefficients. The ship-motion-induced forces (added mass and damping coefficients) were determined by the potential flow theory. The viscous effects were taken into consideration using the Tasai-Takaki method. The modified Bernoulli's equation was used to compute the flow rates. The floodwater inside the compartment was assumed to settle down instantaneously with a horizontal surface.

For the flooding case in waves, Turan and Vassalos (1993) presented a numerical method which coupled the motions of ship and floodwater to assess the survivability of a damaged ferry. The realistic wind and wave conditions were considered. A

coupled system for ship motions of sway, heave and roll together with instantaneous trim was proposed. The external-wave-induced forces (Froude-Krylov and diffraction forces) and ship-motion-induced forces were calculated based on linear potential flow theory. The ship roll damping due to viscous effect was treated through Ikeda's method. The effect of accumulating water was included by taking into account the instantaneous amount of water on deck, roll angle and trim. However, the flooding rates were predefined instead of using time dependent solutions. An improved version with application of modified Bernoulli's equation for the flow rates was soon presented in Vassalos and Turan (1994).

Based on the similar model for floodwater motion, de Kat and Paulling (2001) proposed to use a coupled system for 6-DOF motions instead of using the above 3-DOF ones (sway, heave and roll) to calculate extreme motions of a damaged ship in waves. With the coupled system for 6-DOF motions of ship, Chan et al. (2002) investigated the dynamic motion responses of a damaged Ro-Ro ship to various wave conditions; Palazzi and de Kat (2004) simulated flooding of a damaged frigate with air flow effect; van't Veer et al. (2004) studied the time to flood of a large passenger ship; Lee et al. (2007a) compared the effect of damaged compartment's location and sea state on the ship motions; Santos and Guedes Soares (2009) assessed the factors of sea state, hull form, compartment internal layout and discharge coefficient affecting the survivability of a damaged Ro-Ro passenger ship.

In the seakeeping computation based on linear theory, the hydrodynamic forces and coefficients are normally obtained over the mean wetted surface of the hull. In the case of progressive flooding, this linear approximation is only justified within limited time duration because the underwater geometry of the hull can change significantly. Letizia (1996) and Jasionowski (2001) used a database approach to consider the nonlinear effect due to the change of hull's underwater geometry in the flooding simulation. In this approach, a set of hydrodynamic forces and coefficients were

pre-calculated with the linear method and stored in the database. Their transient values were interpolated from the stored values. This approach is usually referred to as the geometry nonlinear approach.

Although hydrostatic and hydrodynamic loads acting on the external hull surface can be effectively predicted with the aforementioned approaches, addressing floodwater motion (flooding through the opening and internal sloshing) is critical and still challenging in the numerical simulations. Usually the flooding model is based on the well-established hydraulic model, where the volumes of inflowing water are integrated explicitly from the flow velocities determined by a modified Bernoulli's equation. Ruponen (2007) proposed a pressure-correction technique to calculate the volume of inflowing water implicitly. In this approach, each compartment was represented by a single computational cell. The cell pressure was corrected iteratively by solving the continuity and linearized Bernoulli's equations. However, the free surface inside the compartment was assumed to be horizontal, and thus the progress of floodwater was still considered on the basis of hydrostatic pressure. This approach can work well for quasi-stationary flooding simulation but they are not valid for drastic flooding cases.

To improve the model assuming a horizontal water surface inside the compartment, the internal water was considered to be a lump mass moving freely over a specific path surface by Spanos and Papanikolaou (2001). However, the water surface was yet assumed to remain flat. Similar concept was also adopted by Jasionowski (2001) and Manderbacka and Matusiak (2011). These simple assumptions of internal water surface (either horizontal or a freely movable plane) provide adequate results for practical use as long as the sloshing effect is not dominant. Thus, they are frequently adopted in many relevant studies. However, as reported in the ITTC benchmarking study (ITTC, 2002), numerical tools based on the above assumptions failed to predict the ship behaviour reliably in damaged condition.

A more sophisticated model for calculating the internal water dynamics uses a shallow water equation. Chang and Blume (1998) and Chang (1999) employed this model to study survivability of damaged Ro-Ro passenger vessels in seaway with floodwater on car deck. Valanto (2006) also employed the shallow water equation to study the free surface effect on car deck of a Ro-Pax vessel. Santos and Guedes Soares (2008) used the same model to analyze the internal liquid load on the lower compartments of a damaged Ro-Ro ferry in regular beam sea. But the water ingress/egress was not included and the compartment internal layout was not fully modelled in this studied case. Although the shallow water equation can account for the nonlinear sloshing effect, it is only valid in the case where the depth of internal water is much smaller compared to the width of compartment.

To adapt the method to different flooding scenarios, Kong (2009) adopted different models to calculate internal water dynamics. When the damaged opening is small compared to the compartment dimension, the shallow water equation or the multimodal method are used according to the depths of internal water. Otherwise, a so-called hull reshaped method is used, in which all the floodable compartments are combined into a whole one and the internal water is treated as a part of the external sea wave. However, the computed results showed that nonlinear sloshing effects in resonance conditions were still matter when using the proposed hull reshaped method.

In summary, the models for floodwater motion adopted in the conventional method have some limitations. First, a simple hydraulic model drives the water ingress/egress through the opening, and thus, the transient dynamics of the flow are ignored. Second, almost all the approaches assume the water surface in the compartment to be either horizontal or a freely movable plane. When the ship undergoes large-amplitude motion, these approaches lack the ability to model the violent flows with a non-linear free surface. Even the method employing the shallow water equation has its

restriction on the depth of internal water. Third, all mentioned models cannot fully account for the influence of the damaged opening geometry or the compartment's internal layout on the motion of floodwater. Therefore, more effective and accurate models for floodwater motion are necessary.

3.2 Studies Based on CFD Method

A fundamental method of simulating the complex flooding phenomenon is based on solving the NS equations with a free-surface-capturing scheme. The most popular surface-capturing methods include the marker and cell (MAC) method (Harlow and Welch, 1965), the level set (LS) method (Osher and Sethian, 1988) and the volume of fluid (VOF) method (Hirt and Nichols, 1981). The MAC method can account for substantial topology changes in interface. But this method is computationally very expensive due to the requirement of tracing a large number of particles, especially in three-dimensional simulations. The LS method is conceptually simple and relatively easy to implement yielding accurate results when the flow is smooth and evolves with a simple interface. However, the LS method has the principal disadvantage that it suffers from loss of mass in cases where the interface experiences severe stretching or tearing. In the VOF method, a scalar indicator function known as volume fraction is used to represent the interface. An advantage of representing the interface as a volume fraction is the fact that we can write accurate algorithms for advecting the volume fraction so that mass is conserved, while still maintaining a reasonably sharp representation of the interface. Many studies (Nielsen, 2003; Fekken, 2004; Xing-Kaeding, 2006) have confirmed that the VOF method is capable of capturing sharp interfaces, even with large-scale deforming.

Over the past few years, efforts have been made to apply the VOF method to the damaged ship flooding problem. For the case of fixed compartment, Cho et al. (2005) used the VOF method to study the effects of damaged opening geometry,

compartment's internal layout and air compression on the motion of floodwater. Nabavi et al. (2006) and Wood et al. (2010) employed the VOF method to investigate effects of geometric parameters on the discharge rate of an opening.

If a ship is moveable during the flooding process, the equations of rigid body motion have to be solved together with the NS equations, and accordingly, the mesh needs to be updated following the transient ship motion. There have been several dynamic mesh techniques developed in the past to deal with mesh updates, such as spring analogy based smoothing technique (Blom, 2000), remeshing technique (Anderson et at., 2005), sliding mesh technique (Steijl and Barakos, 2008) and overset grid technique (Tang et al., 2003), etc.

Strasser (2010) applied the VOF method to simulate transient and progressive flooding of a freely floating barge in calm water. The barge motion was tackled by utilising the remshing and spring-based smoothing techniques. Turbulent flow and air compressibility were included in the simulation. Fairly good agreement between the numerical and experimental results was obtained. However, it took nearly 2 months to complete a 400-s computation performed on an HPC with 16 processors. Gao et al. (2010) employed the VOF method with sliding mesh technique to analyse the hydrodynamics of a damaged ship section under forced roll motion in calm water. A Similar method was used by Gao and Vassalos (2011) to study roll decay of the same ship section in damaged condition. No confident experimental data was available to validate the numerical results in these two cases.

As an alternative to the mesh based method, like the VOF method, the smoothed particle hydrodynamics (SPH) method (Monaghan, 1992) is becoming an attracted tool for free surface flow calculations. This easy-to-code, mesh-less method can easily handle complex free surface motion, even coupling with large-amplitude motion of the body. González et al. (2003) used the SPH method to predict the

dynamic behaviour of a damaged Ro-Ro ship with a flooded vehicle deck. Skaar et al. (2006) employed the SPH method to model progressive flooding of a damaged ship section forced to oscillate in roll and heave motions. Shen and Vassalos (2009) applied the SPH method to the water sloshing and flooding problems. Le Touzé et al. (2010) simulated ship flooding scenarios using the SPH method. Their studies showcase the ability of the SPH method to model the flooding process with subsequent internal sloshing; however, the required number of particles is large, and modelling the boundaries of the computational domain remains problematic.

Numerical simulation of damaged ship flooding in waves solely based on the CFD method is time-consuming. On the other hand, the potential flow method is practical and efficient to solve general seakeeping problems of ship. To ensure high fidelity during flooding simulations while reducing the computational cost, it is rational to conceive the idea of coupling the CFD and potential flow methods, i.e., the floodwater dynamics is calculated using the CFD method, whereas the ship hydrodynamics induced by sea wave is predicted with the potential flow method. Based on this idea, Kim (2002) investigated the effect of anti-rolling tank equipped on a container ship; Cho et al. (2006) simulated roll decay of a tanker with internal water whose dynamics was obtained using a two-dimensional CFD solver; Kim et al. (2007) studied the sway motion of a box-shaped barge with rectangular tank and the roll motion of a container ship with anti-rolling tank; All of the test ships in the above three studies are in an intact condition.

For the case of a damaged ship, Woodburn et al. (2002) developed a coupled model to assess the survivability of a damaged ship in waves. The computed results were satisfactory in comparison with experimental data. Their work is the only reference that can be found in the area of CFD application to damaged ship flooding in waves. Gao et al. (2004) applied a similar idea to simulate flooding of a damaged ship section in forced heave motion in calm water. The internal water dynamics were

analyzed, but no comparison with experimental results was presented. Although the coupling idea is promising, there is still a dearth of literature reporting its application to investigate the complex interactions between damaged ship, sea wave and floodwater. Much space in this subject can be explored, such as coupling strategy, selection of computational domain, implementation of boundary condition and mesh arrangement, etc.

3.3 Closure

This chapter elucidates the major steps of research development in the area of damaged ship flooding. Various numerical tools developed over the past quarter century have been reviewed. In summary, the force acting on the ship is divided into component of external water acting on the hull surface and component of floodwater acting on the compartments. In the conventional method, the ship-wave interactive dynamics are calculated using the potential flow method. Viscous effects that have significant influence on the roll motion of the ship are treated through different semi-empirical means. The modified empirical Bernoulli's equation is normally used to evaluate the flow rate through the opening. In the earlier studies, the water surface inside the compartment is assumed to be horizontal. Later on, the concept of moving lump mass, shallow water equation, multimodal method and hull reshaped method are introduced to improve the model of internal water motion. To model the floodwater motion more physically, the CFD method is applied to calculate the dynamics of flooding and internal sloshing. The VOF and SPH methods are utilized to deal with complex free surface motion. Different dynamic mesh techniques are adopted to account for the ship motion. In addition, the idea of coupling the potential flow and CFD methods is proposed to retain high numerical fidelity while reducing the computational cost. In the next chapter, the approach adopted in the present research work will be discussed.

Chapter 4

Approach Adopted

The present research work is defined by a set of objectives stated in Chapter 2. Before starting to undertake the work, a clear plan of action and well defined phases of work are required. In this chapter, an overview of the general approach to achieve the specific objectives is given, aiming to clarify and justify the methodology adopted during each phase of this study, and also to provide a roadmap for the following chapters of this thesis.

4.1 Development of NS Solver

There are three interactive sub-problems for damaged ship flooding, i.e., the flooding problem, the sloshing problem and the ship motion problem. In the flooding and sloshing simulation, the most appropriate way to include the full dynamics of floodwater is to model its motion directly. The CFD method based on solving the NS equations with a free-surface-capturing scheme is capable of performing such a simulation. Therefore, development of an NS solver with the VOF model is primary for the research work. As validation and verification are indispensable in the process of solver development, three test cases including dam break, tank sloshing and compartment flooding are performed, aiming to assess the performance of the developed solver in addressing complex free surface motion. The present numerical results are compared with experimental data, analytical solutions or other published numerical results.

The next step is to implement the dynamic mesh techniques in the two-phase flow NS solver, aiming to include the 6-DOF motion of a rigid body in the numerical simulation. After this extension, the NS solver, which is now combines the VOF method with the dynamic mesh techniques, should have the ability to calculate the interactive dynamics of flooding, sloshing and ship motion. To test this ability, two cases of a damaged barge flooding in calm water are simulated. The results obtained are validated against the experimental data.

4.2 Development of Hybrid Method

Although the newly developed NS solver can ensure high numerical fidelity, its application to the area of ship-wave interaction is not practical due to the expensive cost of computation. As a result, simulation of damaged ship flooding in waves solely based on the NS solver is prohibited. On the other hand, the potential flow method is practical and efficient to predict the intact ship motion and sea wave load. However, it is not capable of solving the seakeeping problem of a ship in damaged condition. To combine the advantages of the two methods mentioned above, the following idea is conceived.

A neighbour region of the damaged opening that includes the floodable compartments is derived from the entire flow region. The NS solver is used to model the flow motion in this neighbour region. Its computation cost becomes affordable because of the reduction of computational domain; while most of the flow characteristic during flooding and sloshing is retained. The interactive dynamics between ship and external sea wave are calculated using a seakeeping solver based on the potential flow method. The two solvers are coupled by exchanging information of boundary conditions during the computation. Therefore, the entire dynamic problem involving flooding, sloshing, ship motion and sea wave can be effectively solved.

Within the above idea of solver coupling, a hybrid method that couples the newly developed NS solver and another in-house seakeeping solver is developed. The proposed method is tested by simulating the roll decay of a damaged Ro-Ro ferry and free motion of the ferry in regular beam seas. Our computed results are compared with the results obtained by the model test and conventional methods. Because a clear understanding of the dynamics between damaged ship, sea wave and floodwater is still limited, investigation on these interactive dynamics is carried out based on the hybrid method to reveal the flooding mechanism.

4.3 Closure

This chapter has clearly demonstrated the blueprint of the present research work. Generally, the development of a numerical tool with sufficient accuracy and efficiency for simulation of damaged ship flooding is subdivided into several phases of work, i.e., development of an NS solver, development of a hybrid method and validation of the developed solvers. Additionally, the dynamics involving in the flooding process are analyzed using the newly developed solvers. The remainder of this thesis is mainly concerned on the specific methodology employed in each phase. In the next chapter, the methodology for the NS solver will be first described in detail.

Chapter 5

NS Solver for Coupled Motion of Two-Phase Flow and Floating Body

5.1 Mathematical Model

5.1.1 Governing Equations of Fluid Motion

The present method considers incompressible flow involving two different fluids (water and air). A one-fluid formulation for a two-phase flow is used. According to this model, the integral forms of the NS and the continuity equations described in the global coordinate system (GS), which is a space-fixed Cartesian coordinate system, are as follows:

$$\frac{\partial}{\partial t}\int_V \rho \boldsymbol{u}\mathrm{d}V + \int_S \rho \boldsymbol{u}\left(\boldsymbol{u}-\boldsymbol{u}_S\right)\cdot\boldsymbol{n}\mathrm{d}S = \int_S \mu\nabla\boldsymbol{u}\cdot\boldsymbol{n}\mathrm{d}S - \int_S P\boldsymbol{I}\cdot\boldsymbol{n}\mathrm{d}S + \int_V \rho\boldsymbol{g}\mathrm{d}V \tag{5.1}$$

$$\frac{\partial}{\partial t}\int_V \mathrm{d}V + \int_S \left(\boldsymbol{u}-\boldsymbol{u}_S\right)\cdot\boldsymbol{n}\mathrm{d}S = 0 \tag{5.2}$$

where V denotes the control volume (CV) bounded by a closed surface S; $\boldsymbol{n}$ is the unit vector outwards normal to S; $\boldsymbol{I}$ is the unit tensor; $\boldsymbol{u}$ is the fluid velocity vector; $\boldsymbol{u}_S$ is the velocity vector of the CV face; P is the pressure; $\boldsymbol{g}=(0, 0, g)$ and g is the gravitational acceleration; $\rho=\alpha\rho_1+(1-\alpha)\rho_2$ is the effective density; ρ_1 and ρ_2 are the densities of water and air, respectively; $\mu=\alpha\mu_1+(1-\alpha)\mu_2$ is the effective viscosity; μ_1 and μ_2 are the viscosities of water and air, respectively; and α is the fluid volume

fraction, which is set to 1 in the water region, 0 in the air region and between 0 and 1 for the interface.

The scalar transport equation for the volume fraction written in its integral form is as follows:

$$\frac{\partial}{\partial t}\int_V \alpha \mathrm{d}V + \int_S \alpha\left(\boldsymbol{u}-\boldsymbol{u}_S\right)\cdot\boldsymbol{n}\mathrm{d}S = 0 \tag{5.3}$$

When the CVs change their shapes or positions with time, the so-called space conservation law (SCL) (Demirdžić and Perić, 1988), which is expressed by the following relation between the rate of change of CV volume and its boundary velocity, must be satisfied.

$$\frac{\partial}{\partial t}\int_V \mathrm{d}V - \int_S \boldsymbol{u}_S\cdot\boldsymbol{n}\mathrm{d}S = 0 \tag{5.4}$$

To completely specify the mathematical model, it is necessary to define the initial conditions as well as the boundary conditions of the flow domain. For transient calculations, the initial velocity and density fields are specified according to specific test cases. The initial pressure field is irrelevant to the subsequent evolution of the flow field in incompressible flow calculations, so any guess of this field would suffice in theory. However, it is advantageous to initialise the pressure field to a distribution consistent with the velocity and density field in order to reduce the computational effort. The boundary conditions of the flow domain depend on the specific test cases and are defined in Chapters 7, 8 and 9, respectively.

At the time of the present study, the turbulence models were not implemented in our developed code. All of the simulations of the present test cases are based on the laminar flow model. On the other hand, the flow in the studied cases is dominated by inertial and pressure forces rather than by turbulence effect. Modelling the global motion of the flow plays a more important role in the simulations. Additionally, the

studies reported in the literatures (Lee et al., 2007b; Liu and Lin, 2008; Strasser, 2010) show that turbulence effect on the flows of our interest is small. Thus omitting turbulence modelling in the present study is reasonable.

5.1.2 Governing Equations of Rigid Body Motion

The motion of a rigid body is determined by solving the following linear and angular momentum equations described in the GS:

$$m\dot{\boldsymbol{U}}_G = \boldsymbol{F} \tag{5.5}$$

$$\boldsymbol{J}_G \cdot \dot{\boldsymbol{\Omega}} + \boldsymbol{\Omega} \times \boldsymbol{J}_G \cdot \boldsymbol{\Omega} = \boldsymbol{M}_G \tag{5.6}$$

where m denotes the mass of the body; G denotes the centre of m; $\boldsymbol{U}_G$ is the velocity vector of G; $\boldsymbol{F}$ is the resultant vector of external forces acting on the body; $\boldsymbol{J}_G$ is the tensor of inertia moments of the body with respect to G; $\boldsymbol{\Omega}$ is the angular velocity vector of the body; and $\boldsymbol{M}_G$ is the resultant vector of external moments acting on the body with respect to G.

The moment of inertia ($\boldsymbol{J}_G$), resultant external force ($\boldsymbol{F}$) and moment ($\boldsymbol{M}_G$) are evaluated by the following expressions:

$$\boldsymbol{J}_G = \boldsymbol{T}_T \cdot \boldsymbol{J}'_G \cdot \boldsymbol{T}_T^{-1} \tag{5.7}$$

$$\boldsymbol{T}_T = \begin{bmatrix} \cos\beta\cos\theta & \cos\beta\sin\theta\sin\gamma - \sin\beta\cos\gamma & \cos\beta\sin\theta\cos\gamma + \sin\beta\sin\gamma \\ \sin\beta\cos\theta & \sin\beta\sin\theta\sin\gamma + \cos\beta\cos\gamma & \sin\beta\sin\theta\cos\gamma - \cos\beta\sin\gamma \\ -\sin\theta & \cos\theta\sin\gamma & \cos\theta\cos\gamma \end{bmatrix} \tag{5.8}$$

$$\boldsymbol{F} = \int_{S_B} \left\{ \mu \left[\nabla \boldsymbol{u} + \left(\nabla \boldsymbol{u} \right)^{\mathrm{T}} \right] - P\boldsymbol{I} \right\} \cdot \boldsymbol{n} dS + m\boldsymbol{g} \tag{5.9}$$

$$\boldsymbol{M}_G = \int_{S_B} (\boldsymbol{r} - \boldsymbol{r}_G) \times \left\{ \mu \left[\nabla \boldsymbol{u} + (\nabla \boldsymbol{u})^{\mathrm{T}} \right] - P\boldsymbol{I} \right\} \cdot \boldsymbol{n} dS \tag{5.10}$$

where $\boldsymbol{J}'_G$ is the tensor of inertia moments of the body with respect to G described in the body-fixed coordinate system (BS), which is a Cartesian coordinate system with origin at G, rotating along with the body; note that $\boldsymbol{J}'_G$ is usually known at the beginning of the calculation for a certain rigid body and remains constant with respect to the BS during the calculation. $\boldsymbol{T}_T$ is the transformation matrix from the BS to the GS, the derivation of which is given in Appendix A.2; β, θ and γ are the Euler angles, the definitions of which are described in Appendix A.1; S_B denotes the body surface; $\boldsymbol{r}$ denotes the position vector of a point on S_B; and $\boldsymbol{r}_G$ is the position vector of G.

5.2 Numerical Method

5.2.1 Calculation of Fluid Field

To numerically solve the fluid field, governing equations (5.1) to (5.3) are discretised by the finite volume (FV) method on a collocated grid, where all the flow properties are defined at the centre of the CV. The details of temporal and spatial discretisation techniques in the FV method have been fully described by Versteeg and Malalasekera (1995); thus, the final discretised forms of Eqs. (5.1) to (5.3) are given as follows without further proof:

$$\begin{aligned} &\left(\rho_q^{t_{n+1}} \boldsymbol{u}_q^{t_{n+1}} V_q^{t_{n+1}} - \rho_q^{t_n} \boldsymbol{u}_q^{t_n} V_q^{t_n} \right) \frac{1}{\delta t} + \sum_{i=1}^{k} \rho_{f_i}^{t_{n+1}} E_{f_i}^{t_{n+1}} \boldsymbol{u}_{f_i}^{t_{n+1}} \\ &\quad = \sum_{i=1}^{k} \mu_{f_i}^{t_{n+1}} \boldsymbol{A}_{f_i}^{t_{n+1}} \cdot (\nabla \boldsymbol{u})_{f_i}^{t_{n+1}} - \sum_{i=1}^{k} P_{f_i}^{t_{n+1}} \boldsymbol{A}_{f_i}^{t_{n+1}} + \rho_q^{t_{n+1}} \boldsymbol{g} V_q^{t_{n+1}} \end{aligned} \tag{5.11}$$

$$\sum_{i=1}^{k} \boldsymbol{u}_{f_i}^{t_{n+1}} \cdot \boldsymbol{A}_{f_i}^{t_{n+1}} = 0 \tag{5.12}$$

$$\left(\alpha_q^{t_{n+1}} V_q^{t_{n+1}} - \alpha_q^{t_n} V_q^{t_n}\right)\frac{1}{\delta t} + \frac{1}{2}\sum_{i=1}^{k}\left(\alpha_{f_i}^{t_{n+1}} + \alpha_{f_i}^{t_n}\right) E_{f_i}^{t_{n+1}} = 0 \tag{5.13}$$

where subscripts q and f denote values at the centre of the CV and at the centre of the CV face, respectively; superscripts t_n and t_{n+1} denote values at time level n and $n+1$, respectively; δt is the time step; and k is the number of faces of a CV. E_f is the volumetric flux at the CV face, and applying SCL (see Eq. (5.4)), $E_f = \boldsymbol{u}_f \cdot \boldsymbol{A}_f - \delta V_i / \delta t$; δV_i is the change of CV volume due to the motion of the CV face i. $\boldsymbol{A}_f$ is the area vector of the CV face.

Note that the Crank-Nicolson (CN) scheme is used for the temporal discretisation of the volume fraction (see Eq. (5.13)) to avoid introducing numerical diffusion (Ubbink, 1997). In order to be consistent with it, the CN scheme should also be utilized for the temporal discretisation of other flow properties. However, the CN scheme is more expensive in terms of computer storage because it needs both the old and the new time level's values of the flow properties. For a small enough time step, the variations of other flow properties such as E and $\boldsymbol{u}$ are negligible in comparison with the larger variation of α. Therefore, the Euler implicit scheme is applied to the temporal discretisation of the NS equations instead and only the most recent value of E is used in Eq. (5.13).

Eqs. (5.11) to (5.13) use the values of flow properties at the centre of the CV as well as at the centres of the CV faces. For the spatial discretisation based on a collocated grid system, the CV centre values are used to interpolate the values on the CV faces. The face velocity ($\boldsymbol{u}_f$) in the second term (convective term) on the left-hand side of Eq. (5.11) is calculated using a hybrid differencing scheme (Spalding, 1972), whereas the momentum interpolation method (Rhie and Chow, 1983) is used to calculate $\boldsymbol{u}_f$ in Eq. (5.12) and in the volumetric flux (E) to suppress non-physical oscillations in the pressure field. The velocity gradient in the first term (diffusive

term) on the right-hand side of Eq. (5.11) is calculated using the method described in Date (2005). A piecewise linear interpolation (Panahi et al., 2006) is used to calculate the face pressure (P_f) to eliminate the interpolation error caused by the large density ratio of two-phase flow. To retain the physical interface profile, the compressive interface capturing scheme for arbitrary meshes (CICSAM) proposed by Ubbink (1997) is used to calculate the face volume fraction (α_f). Appendix B briefly describes the aforementioned interpolation schemes. In order to calculate the pressure field and couple it to the velocity field, the continuity equation, i.e., Eq. (5.12), is transformed into a pressure-correction equation following the semi-implicit method for pressure-linked equations (SIMPLE) proposed by Patankar and Spalding (1972).

Now all the face values in Eqs. (5.11) to (5.13) can be approximated in terms of the values at CV centres and it is possible to reformulate the above equations in terms of these values. In order to limit the implicit parts of the discretised equations to a CV and its nearest neighbours, a deferred-correction approach (Xue et al., 2002) is used. In this approach, a simplified approximation, which utilizes only the values in the nearest neighbouring CVs, is employed to calculate the values on the CV faces; the difference between the simplified approximation and the full approximation mentioned previously is computed explicitly from the values obtained in the previous iteration and added to the source term on the right-hand side of the equation. The algebraic equation obtained finally for each variable in each CV has the following general form:

$$a_q \chi_q^{t_{n+1}} + \sum_{nb=1}^{NK} a_{nb} \chi_{nb}^{t_{n+1}} = b_q \tag{5.14}$$

where χ denotes a general variable; a_q and a_{nb} are the diagonal and off-diagonal coefficients of the discretised equation, respectively; b is the source term; superscript

t_{n+1} denote value at time level $n+1$; subscripts q and nb denote values at the centres of CV q and its nearest neighbours, respectively; NK is the number of the nearest neighbours of CV q. Eq. (5.14) is a large sparse linear system which can be solved efficiently using iterative methods. In this study, we employ the generalized minimal residual (GMRES) method (Saad and Schultz, 1986) with the preconditioner of incomplete LU factorization with threshold (ILUT) (Saad, 1994) to solve this linear system.

Although both the Euler implicit and CN schemes are unconditionally stable regardless of the time step, it is necessary to use a small time step in the simulation to reduce numerical diffusion, which may smear the sharp interface profile. Unless stated otherwise the time step used in the present test cases is automatically adjusted to keep the cell Courant number within a given limit:

$$Co_q = \sum_{i=1}^{k} \max\left\{\frac{-E_{f_i}\delta t}{V_q}, 0\right\} \le Co_{\lim} \tag{5.15}$$

where Co_q is the cell Courant number of CV q and $Co_{\lim}$ is the given limit of the cell Courant number, the value of which will be discussed in Chapters 7 and 8. The definitions of the other symbols are identical to those in Eq. (5.11).

5.2.2 Calculation of Body Motion

Once the flow properties are solved by the above numerical method, the resultant force and moment acting on the body can be evaluated from Eqs. (5.9) and (5.10). The velocity of G is then obtained by integrating Eq. (5.5) over time, and the final discretised expression reads as follows:

$$\boldsymbol{U}_G^{t_{n+1}} = \boldsymbol{U}_G^{t_n} + \boldsymbol{F}^* \frac{\delta t}{m} \tag{5.16}$$

$$\boldsymbol{F}^{*} = \frac{\boldsymbol{F}^{t_{n-1}} + \boldsymbol{F}^{t_n}}{2} \tag{5.17}$$

The new position of G can be computed from the following expression:

$$\boldsymbol{r}_G^{t_{n+1}} = \boldsymbol{r}_G^{t_n} + \boldsymbol{U}_G^{*}\delta t \tag{5.18}$$

$$\boldsymbol{U}_G^{*} = \frac{\boldsymbol{U}_G^{t_n} + \boldsymbol{U}_G^{t_{n+1}}}{2} \tag{5.19}$$

Integrating Eq. (5.6) in a similar manner gives the expression of the angular velocity of the body:

$$\boldsymbol{\Omega}^{t_{n+1}} = \left(\boldsymbol{J}_G^{*}\right)^{-1} \cdot \left(\boldsymbol{M}_G^{*} - \boldsymbol{\Omega}^{*} \times \boldsymbol{J}_G^{*} \cdot \boldsymbol{\Omega}^{*}\right) \tag{5.20}$$

$$\boldsymbol{J}_G^{*} = \frac{\boldsymbol{J}_G^{t_{n-1}} + \boldsymbol{J}_G^{t_n}}{2} \tag{5.21}$$

$$\boldsymbol{M}_G^{*} = \frac{\boldsymbol{M}_G^{t_{n-1}} + \boldsymbol{M}_G^{t_n}}{2} \tag{5.22}$$

$$\boldsymbol{\Omega}^{*} = \frac{\boldsymbol{\Omega}^{t_{n-1}} + \boldsymbol{\Omega}^{t_n}}{2} \tag{5.23}$$

Instead of directly integrating the angular velocity to obtain the rotation angles of the body, a more general method is adopted in the present study. Let vectors $\boldsymbol{i}$, $\boldsymbol{j}$ and $\boldsymbol{k}$ attached to the BS represent the body orientation, which has the following relations with the angular velocity (see Appendix A.3):

$$\dot{\boldsymbol{i}} = \boldsymbol{\Omega} \times \boldsymbol{i} \tag{5.24}$$

$$\dot{\boldsymbol{j}} = \boldsymbol{\Omega} \times \boldsymbol{j} \tag{5.25}$$

$$\dot{\boldsymbol{k}} = \boldsymbol{\Omega} \times \boldsymbol{k} \tag{5.26}$$

Vector $\boldsymbol{i}$ is obtained from the following discretised form:

$$\boldsymbol{i}^{t_{n+1}} = \boldsymbol{\Omega}^* \times \boldsymbol{i}^* \tag{5.27}$$

$$\boldsymbol{\Omega}^* = \frac{\boldsymbol{\Omega}^{t_n} + \boldsymbol{\Omega}^{t_{n+1}}}{2} \tag{5.28}$$

$$\boldsymbol{i}^* = \frac{\boldsymbol{i}^{t_{n-1}} + \boldsymbol{i}^{t_n}}{2} \tag{5.29}$$

Vectors $\boldsymbol{j}$ and $\boldsymbol{k}$ are treated in a same manner like $\boldsymbol{i}$. Subsequently, the body rotation angles are calculated as follows (see Appendix A.4):

$$\gamma^{t_{n+1}} = \arccos\left(\frac{\boldsymbol{j}'}{|\boldsymbol{j}'|} \cdot \frac{\boldsymbol{j}^{t_{n+1}}}{|\boldsymbol{j}^{t_{n+1}}|} \right) \tag{5.30}$$

$$\theta^{t_{n+1}} = \arccos\left(\frac{\boldsymbol{i}'}{|\boldsymbol{i}'|} \cdot \frac{\boldsymbol{i}^{t_{n+1}}}{|\boldsymbol{i}^{t_{n+1}}|} \right) \tag{5.31}$$

$$\beta^{t_{n+1}} = \arccos\left(\frac{\boldsymbol{I}}{|\boldsymbol{I}|} \cdot \frac{\boldsymbol{i}'}{|\boldsymbol{i}'|} \right) \tag{5.32}$$

$$\boldsymbol{i}' = \boldsymbol{i}^{t_{n+1}} - \left(\boldsymbol{i}^{t_{n+1}} \cdot \boldsymbol{K} \right) \boldsymbol{K} \tag{5.33}$$

$$\boldsymbol{j}' = \boldsymbol{K} \times \boldsymbol{i}' \tag{5.34}$$

where angles γ, θ and β are the roll, pitch and yaw angles of the body, respectively,

and they are also the Euler angles appearing in Eq. (5.8); vectors ***I*** and ***K*** represent the orientations of *x*- and *z*-axes of GS, respectively.

5.2.3 Dynamic Mesh Strategy

Because the body surface is a part of the fluid domain boundary, when the body moves during the calculation, it is necessary to update the mesh dynamically according to the geometry change of the fluid domain. In this study, a combined dynamic mesh strategy is used to handle the mesh update. The computational domain is divided into three regions, as shown in Figure 5.1.

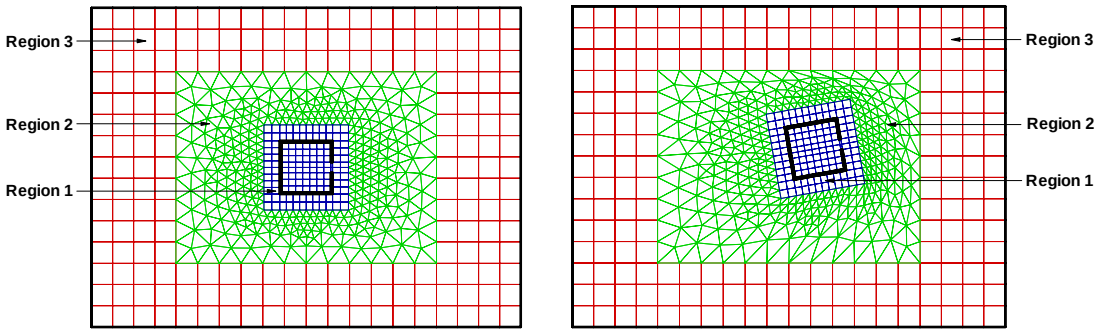

Figure 5.1: Dynamic mesh strategy (Left: initial stage, right: later stage).

Region 1 undergoes the same translational and rotational motion of the body so that the mesh in this region is moved without geometrical and topological change. This action ensures optimum mesh quality in the most important fluid domain is maintained throughout the calculation. Region 3 is kept static, and its mesh is fixed during the simulation, which makes it easier to implement specific boundary conditions (e.g., inlet or outlet boundary conditions) along the outer boundaries. In the buffer region (region 2), the mesh automatically deforms following the change in the geometry of the region boundary while keeping its topology constant. The spring-based smoothing method is employed to address this mesh deformation, where the displacements of mesh vertexes satisfy the following equilibrium equation:

$$\sum_{j=1}^{n_i} s_{ij}\delta \boldsymbol{x}_i = \sum_{j=1}^{n_i} s_{ij}\delta \boldsymbol{x}_j \tag{5.35}$$

where $\delta \boldsymbol{x}_i$ and $\delta \boldsymbol{x}_j$ are the displacements of vertexes i and j, respectively; n_i is the number of neighbours of vertex i; s_{ij} is the stiffness of the spring between vertexes i and j, and it is determined based on the ortho-semi-torsional (OST) spring analogy concept proposed by Markou et al. (2007). Once positions of boundary vertexes of region 2 are updated, their corresponding displacements will provide the Dirichlet boundary conditions for Eq. (5.35). Subsequently, displacements of interior vertexes are obtained by solving Eq. (5.35) iteratively:

$$\delta \boldsymbol{x}_i^{k+1} = \frac{\sum_{j=1}^{n_i} s_{ij}\delta \boldsymbol{x}_j^k}{\sum_{j=1}^{n_i} s_{ij}} \tag{5.36}$$

After the above iteration converges, the interior vertexes are displaced by adding the converged displacement:

$$\boldsymbol{x}_i^{t_{n+1}} = \boldsymbol{x}_i^{t_n} + \delta \boldsymbol{x}_i^{k,\text{converged}} \tag{5.37}$$

5.2.4 Solution Procedure

The overall procedure for the coupled computation of flow and body motion is as follows:

(a) Initialise all variables.

(b) Calculate the Courant number and adjust the time step if necessary (applicable to variable time step).

(c) Solve the NS equations for the intermediate velocity components.

(d) Solve the continuity equation for the pressure correction and correct the volumetric flux, velocity components and pressure.

(e) Solve the volume fraction transport equation for the volume fraction, and use the computed values to update the fluid density and viscosity.

(f) Return to step (c) and repeat until convergence is achieved for all flow variables.

(g) Calculate the resultant force and moment acting on the body.

(h) Solve the rigid body motion equations for the new position and orientation of the body.

(i) Adapt the mesh to the new position and orientation of the body.

(j) Return to step (b) and advance to the next time level until the end of the specified time duration.

5.3 Closure

In this chapter, a mathematical model for the calculation of three-dimensional, time-dependent, incompressible, viscous, turbulence free, two-phase flow with body motion in 6-DOF has been introduced. To numerically solve the governing equations, a newly developed NS solver based on FV discretisation was presented. The well-known SIMPLE algorithm was employed for pressure-velocity coupling. A VOF family algorithm, CICSAM, was used to capture the free surface. A combined dynamic mesh strategy was proposed to include the motion of a body into the fluid field calculation. The NS solver is ready for solely solving the general interactive dynamic problems of fluid and body. To improve the computational efficiency, the

NS solver will be coupled a seakeeping solver to simulate flooding of a damaged ship in waves, which is the subject of the next chapter.

Chapter 6

Hybrid Method for Damaged Ship Flooding in Waves

6.1 Mathematical Model

6.1.1 Reference Coordinate System

Let us consider a damaged ship advancing at constant mean forward speed (U_0) through sea wave in infinite depth water. Its motion is not only influenced by the excitation of sea wave but also by the liquid loads due to water flooding and sloshing. In the GS, the motion of a ship is described as: the ship advances at forward speed U_0 while undergoing an oscillatory motion.

A reference coordinate system (RS) is introduced to describe the position and orientation of the ship more conveniently. The RS is a non-rotating, non-accelerating, Cartesian coordinate system, which is moving together with the ship at forward speed U_0 and is constantly fixed with respect to the mean position of the ship. Its origin is located on the undisturbed free surface. X-axis points the direction of forward motion of the ship and z-axis points vertically upwards. In the RS, the motion of a ship reduces to a pure oscillation without mean forward speed, the effect of which is alternatively considered by adding an incoming uniform flow with velocity U_0 in the direction of the negative x-axis in the flow field. All equations given in this chapter are expressed with respect to the RS.

6.1.2 External Forces Acting on a Ship

The ship is considered as a rigid body. Within the framework of linear potential flow theory, the components of external forces and moments acting on a ship can be generalized as follows:

$$F_j = F_{\mathrm{FK},j} + F_{\mathrm{D},j} + F_{\mathrm{R},j} + F_{\mathrm{B},j} + F_{\mathrm{W},j} + F_{\mathrm{G},j}, \qquad j = 1,2,\ldots,6 \tag{6.1}$$

where j denotes the components of the external forces or moments (moment understood for j=4, 5, 6 and with respect to the mass centre of the ship); F_{FK} and F_{D} are, respectively, the Froude-Krylov and diffraction forces, which are collectively known as wave excitation force; F_{R} is the radiation force induced by the ship motion; F_{B} is the buoyancy force; F_{W} is liquid load due to the motion of floodwater inside the compartments; F_{G} is the gravitational force, $\boldsymbol{F}_{\mathrm{G}}$=(0, 0, mg, 0, 0, 0); and m is the ship mass. Note that the ship resistance is assumed to be balanced by the propeller thrust in the present study, and hence these two forces are not included in Eq. (6.1).

6.1.3 Wave Excitation Force

The wave excitation force, i.e., the resultant of Froude-Krylov and diffraction forces, is expressed in terms of the incident wave potential (Φ_{I}) and diffraction potential (Φ_{D}) (Salvesen et al., 1970):

$$F_{\mathrm{FK+D},j}(t) = -\rho \int_{S_H} \left(\frac{\partial}{\partial t} - U_0 \frac{\partial}{\partial x} \right) \left(\Phi_{\mathrm{I}} + \Phi_{\mathrm{D}} \right) n_j \, dS, \qquad j = 1,2,\ldots,6 \tag{6.2}$$

where ρ is the fluid density; n_j is the generalized normal, defined as (n_1, n_2, n_3)=$\boldsymbol{n}$ and (n_4, n_5, n_6)=($\boldsymbol{r}$−$\boldsymbol{r}_{\mathrm{G}}$)×$\boldsymbol{n}$; $\boldsymbol{n}$, $\boldsymbol{r}$ and $\boldsymbol{r}_G$ have been defined in Sections 5.1.1 and 5.1.2; and S_H denotes the instantaneous wetted surface of the hull for Φ_{I}, whereas it denotes the mean wetted surface for Φ_{D}. Note that the free surface around a ship oscillating at

sea wave is composed of incident, diffraction and radiation waves. Among these three components, the incident wave is dominant in high seas. Thus, only the incident wave elevation is taken into account for the evaluation of wetted hull surface in the present study.

For a regular harmonic incident wave propagating in infinite depth water, its corresponding potential has the following expression (Mei et al., 2005):

$$\Phi_{\mathrm{I}}\left(x,y,z;t\right)=\mathrm{Re}\left[\phi_{\mathrm{I}}\left(x,y,z\right)e^{i\omega t}\right] \tag{6.3}$$

$$\phi_{\mathrm{I}}\left(x,y,z\right)=\frac{ig\xi_{\mathrm{I}}}{\omega_0}e^{K_0\left[z-i\left(x\cos\varphi-y\sin\varphi\right)\right]} \tag{6.4}$$

where ϕ_{I} is the complex amplitude of incident wave potential or is referred to as spatial potential; ξ_{I} is the incident wave amplitude; $K_0=\omega_0^2/g$ is the incident wave number; ω_0 is the circular frequency of the incident wave; φ is the heading angle, which is the angle between the propagating direction of incident wave and the positive x-axis (φ=0 for the following wave); $\omega=\omega_0-K_0U_0\cos\varphi$ is the encounter frequency; and symbol Re is understood that real part of the subsequent expression is to be taken.

In accordance with the expression of incident wave potential (Eq. (6.3)), the diffraction potential can be also expressed in a harmonic form:

$$\Phi_{\mathrm{D}}\left(x,y,z;t\right)=\mathrm{Re}\left[\phi_{\mathrm{D}}\left(x,y,z\right)e^{i\omega t}\right] \tag{6.5}$$

where the spatial potential ϕ_{D} satisfies the equations below:

$$\Delta\phi_{\mathrm{D}}\left(x,y,z\right)=0,\ \text{in the fluid domain} \tag{6.6}$$

$$\left[\left(i\omega - U_0\frac{\partial}{\partial x}\right)^2 + g\frac{\partial}{\partial z}\right]\phi_{\mathrm{D}} = 0, \text{ on the undisturbed free surface } (z=0) \qquad (6.7)$$

$$\frac{\partial \phi_{\mathrm{D}}}{\partial n} = -\frac{\partial \phi_{\mathrm{I}}}{\partial n}, \text{ on the hull at mean position} \qquad (6.8)$$

Moreover, ϕ_{D} at infinity must satisfy an appropriate boundary condition to ensure that the disturbance waves generated can propagate away from the ship.

For a damaged ship, the seawater can freely flow across the damaged opening. Consequently, the non-penetration condition (Eq. (6.8)) is, in theory, only valid on the intact part of the hull surface, whereas the actual velocity of flow is distributed at the damaged opening. On the other hand, although the damaged opening could influence the hydrodynamics outside the ship, the resulting effect on the ship behaviour is limited if the opening is not too large. To simplify the mathematical model, in the present study the ship is considered as an intact body when solving the diffraction and radiation problems, in which the non-penetration condition is imposed on the hull surface without any modification.

St. Denis and Pierson (1953) pointed out that irregular waves can be described by superposing a large number of essentially independent regular waves with random phases provided that the linear assumption is valid. Thus, the above theory for harmonic waves can be easily applied to the case of irregular waves. The force of irregular wave excitation is given as:

$$F_{\mathrm{FK+D},j}(t) = \sum_{k=1}^{N}\left[-\rho\int_{S_H}\left(\frac{\partial}{\partial t} - U_0\frac{\partial}{\partial x}\right)\left(\Phi_{\mathrm{I},k} + \Phi_{\mathrm{D},k}\right)n_j dS\right], \quad j = 1,2,\ldots,6 \qquad (6.9)$$

where N is the total number of component waves; and variable with subscript k is corresponding to the k-th component.

The incident wave potential for component k is expressed as:

$$\Phi_{\mathrm{I},k}\left(x,y,z;t\right)=\mathrm{Re}\left[\phi_{\mathrm{I},k}\left(x,y,z\right)e^{i\left(\omega_k t+\sigma_k\right)}\right] \tag{6.10}$$

$$\phi_{\mathrm{I},k}\left(x,y,z\right)=\frac{ig\xi_{\mathrm{I},k}}{\omega_{0,k}}e^{K_{0,k}\left[z-i\left(x\cos\varphi-y\sin\varphi\right)\right]} \tag{6.11}$$

where σ_k denotes the phase angle of the component wave, which is distributed randomly in the range of $[0, 2\pi]$; wave amplitude $\xi_{\mathrm{I},k}$ of each component is determined from a given wave energy spectrum. The diffraction potential $\Phi_{\mathrm{D},k}$ is expressed in a similar form of Eq. (6.10). To determine the spatial potential $\phi_{\mathrm{D},k}$, Eqs. (6.6) to (6.8) are rewritten in the corresponding forms for each component.

6.1.4 Radiation Force

Based on the work of Cummins (1962) and Ogilvie (1964) (see Appendix C), the radiation force is calculated using the added mass and damping coefficients in frequency domain and transformed into the time domain:

$$F_{\mathrm{R},j}\left(t\right)=-\sum_{k=1}^{6}\left[A_{jk}\left(\infty\right)\dot{U}_{G,k}\left(t\right)+\int_{-\infty}^{t}K_{jk}\left(t-\tau\right)U_{G,k}\left(\tau\right)d\tau\right],\quad j=1,2,\ldots,6 \tag{6.12}$$

$$K_{jk}\left(t\right)=\frac{2}{\pi}\int_{0}^{\infty}B_{jk}\left(\omega\right)\cos\left(\omega t\right)d\omega \tag{6.13}$$

where A and B are the frequency-dependent added mass and damping coefficient, respectively; $A(\infty)$ represents the infinite frequency limit of the added mass; k=1, 2, 3, 4, 5 and 6 refer to surge, sway, heave, roll, pitch and yaw motions of the ship, respectively; A_{jk} and B_{jk} (for $j \neq k$) are, respectively, the added mass and damping coefficient for a ship's oscillatory motion in the k-th mode coupled into the j-th mode of motion (e.g., A_{24} is the added mass for roll motion coupled into sway motion). $U_{G,k}$,

for k=1, 2, 3, is the k-th mode oscillatory velocity of the ship's mass centre G; for k=4, 5, 6, it is the oscillatory angular velocity of the ship with respect to G.

The ship is assumed to oscillate harmonically. The frequency-dependent added mass and damping coefficient are expressed in term of the spatial potential for the oscillatory motion (Salvesen et al., 1970):

$$A_{jk}(\omega) = -\frac{\rho}{\omega^2}\mathrm{Re}\left[\int_{S_H}\left(i\omega - U_0\frac{\partial}{\partial x}\right)\phi_{\mathrm{R},k}\, n_j\, dS\right], \quad j,k = 1,2,\ldots,6 \tag{6.14}$$

$$B_{jk}(\omega) = \frac{\rho}{\omega}\mathrm{Im}\left[\int_{S_H}\left(i\omega - U_0\frac{\partial}{\partial x}\right)\phi_{\mathrm{R},k}\, n_j\, dS\right], \quad j,k = 1,2,\ldots,6 \tag{6.15}$$

where $\phi_{\mathrm{R},k}$ is the spatial potential for a ship's oscillatory motion in the k-th mode; S_H denotes the mean wetted surface of the hull; and symbol Im is understood that imaginary part of the subsequent expression is to be taken.

The governing equation and boundary conditions for the definite solution of ϕ_{R} are stated as follows:

$$\Delta\phi_{\mathrm{R},j}(x,y,z) = 0, \text{ in the fluid domain} \tag{6.16}$$

$$\left[\left(i\omega - U_0\frac{\partial}{\partial x}\right)^2 + g\frac{\partial}{\partial z}\right]\phi_{\mathrm{R},j} = 0, \text{ on the undisturbed free surface } (z=0) \tag{6.17}$$

$$\frac{\partial\phi_{\mathrm{R},j}}{\partial n} = i\omega n_j + U_0 m_j, \text{ on the hull at mean position} \tag{6.18}$$

where m_j=0 for j=1, 2, 3, 4, whereas $m_5=n_3$ and $m_6=n_2$. Additionally, an appropriate boundary condition should be imposed at infinity to ensure that the radiation waves can propagate away from the ship.

Eqs. (6.14) to (6.18) indicate that A_{jk} and B_{jk} only depend on the ship geometry and encounter frequency while being independent on the past history of the ship motion. Consequently, $A_{jk}(\infty)$ and K_{kj} only need to be calculated once for a given ship, and then the radiation force can be evaluated for any arbitrary motion using Eq. (6.12). Moreover, Eq. (6.12) is frequency-independent, thus it is valid to evaluate the radiation force associated with irregular motion of a ship.

6.1.5 Buoyancy Force

Buoyancy force is the hydrostatic component of sea loads acting on the external hull surface. It is evaluated by integrating the hydrostatic pressure over the instantaneous wetted surface of the ship:

$$F_{\mathrm{B},j}(t) = \int_{S_H} \rho g z n_j dS, \qquad j = 1, 2, \ldots, 6 \tag{6.19}$$

where $-\infty < z < \eta_{\mathrm{I}}$; η_{I} is the elevation of incident wave and is calculated with the following expressions.

For regular incident wave,

$$\eta_{\mathrm{I}}(x, y; t) = \xi_{\mathrm{I}} \cos\left[K_0 (x \cos\varphi - y \sin\varphi) - \omega t \right] \tag{6.20}$$

For irregular incident wave,

$$\eta_{\mathrm{I}}(x, y; t) = \sum_{k=1}^{N} \left\{ \xi_{1,k} \cos\left[K_{0,k} (x \cos\varphi - y \sin\varphi) - \omega_k t + \sigma_k \right] \right\} \tag{6.21}$$

6.1.6 Internal Liquid Load

Water flooding through the damaged opening and sloshing inside the compartments

is affected by the ship's behaviour as well as by the external sea wave. Thus, the computational domain for floodwater motion ought to include the floodable compartments and an external flow region around the damaged section of the ship, as shown in Figure 6.1.

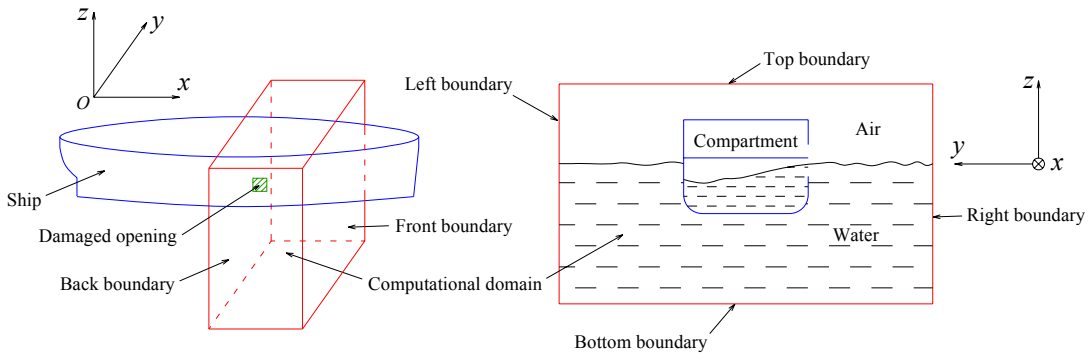

Figure 6.1: Sketch of the computational domain for floodwater motion.

The fluid motion in the above computational domain is governed by Eqs. (5.1) to (5.3). The boundary conditions of this domain depend on the heading angle. Take the case of beam seas ($\varphi=\pi/2$) for example. On the top boundary, the pressure is set to be the atmospheric pressure. The hydrostatic pressure corresponding to the initial water height is imposed on the bottom boundary. On the left boundary, the initial water height and the hydrostatic pressure are imposed. On the front and back boundaries, the initial water height and the velocity of incoming uniform flow ($-U_0$, 0, 0) are imposed. On the right boundary, the incident wave elevation (calculated with Eqs. (6.20) or (6.21)) and specific fluid velocity are imposed. The specific fluid velocity is composed of the velocities of incoming uniform flow and incident wave ($\nabla\Phi_\mathrm{I}$ for regular wave or $\sum_{k=1}^{N}\left(\nabla\Phi_{\mathrm{I},k}\right)$ for irregular wave). Once the flow properties in the compartments are obtained, the corresponding internal liquid load can be evaluated as follows:

$$\left(F_{\mathrm{W},1},F_{\mathrm{W},2},F_{\mathrm{W},3}\right)=\int_{S_C}\left\{\mu\left[\nabla\boldsymbol{u}+\left(\nabla\boldsymbol{u}\right)^{\mathrm{T}}\right]-P\boldsymbol{I}\right\}\cdot\boldsymbol{n}dS \tag{6.22}$$

$$\left(F_{\mathrm{W},4}, F_{\mathrm{W},5}, F_{\mathrm{W},6}\right) = \int_{S_C} \left(\boldsymbol{r} - \boldsymbol{r}_G\right) \times \left\{\mu\left[\nabla \boldsymbol{u} + \left(\nabla \boldsymbol{u}\right)^{\mathrm{T}}\right] - P\boldsymbol{I}\right\} \cdot \boldsymbol{n} dS \tag{6.23}$$

where S_C is the surface of floodable compartments; and the other symbols have been defined in Section 5.1.

6.1.7 Governing Equation of Ship Motion

The motion of a ship can be represented by the mass centre translation and the body rotation around its mass centre. The corresponding linear and angular velocities are determined by the momentum equations, the forms of which described in the RS are identical to Eqs. (5.5) and (5.6) described in the GS. Replacing the external forces on the right-hand sides of the momentum equations by Eq. (6.1) and moving the term of radiation force to the left-hand sides, a set of differential equations for the ship motion with 6-DOF read:

$$\begin{aligned} &\sum_{k=1}^{6}\left\{\left[\Lambda_{jk} + A_{jk}\left(\infty\right)\right]\dot{U}_{G,k}\left(t\right) + \int_{-\infty}^{t} K_{jk}\left(t-\tau\right)U_{G,k}\left(\tau\right)d\tau\right\} \\ &+\sum_{k=4}^{6}\sum_{l=4}^{6}\left[\lambda_{jkl}U_{G,k}\sum_{q=4}^{6}\left(\Lambda_{lq}U_{G,q}\right)\right] = F_{\mathrm{FK+D+B+W+G},j}, \quad j = 1,2,\ldots,6 \end{aligned} \tag{6.24}$$

The permutation symbol λ and generalized mass matrix Λ are respectively defined as:

$$\lambda_{jkl} = \begin{cases} 1, & \text{if } \left(j,k,l\right) \text{ is an even permutation of } \left(4,5,6\right); \\ -1, & \text{if } \left(j,k,l\right) \text{ is an odd permutation of } \left(4,5,6\right); \\ 0, & \text{if } j \le 3 \text{ or any index is repeated.} \end{cases} \tag{6.25}$$

$$\left[\Lambda_{jk}\right] = \begin{bmatrix} m & 0 & & & & \\ & m & & & 0 & \\ 0 & & m & & & \\ & & & J_{G,11} & J_{G,12} & J_{G,13} \\ & 0 & & J_{G,21} & J_{G,22} & J_{G,23} \\ & & & J_{G,31} & J_{G,32} & J_{G,33} \end{bmatrix} \tag{6.26}$$

where m is the ship mass; and $\boldsymbol{J}_G$ is the tensor of inertia moments of the ship with respect to the mass centre and has been defined in Section 5.1.2.

6.2 Numerical Method

The aforementioned interactive dynamics between the ship, sea wave and floodwater are calculated using a hybrid method. In this method, an in-house seakeeping solver, PROTEUS3 (Jasionowski, 2001), is used to calculate the buoyancy force, wave excitation force and hydrodynamic coefficients (added mass and damping coefficient). The calculations of diffraction and radiation hydrodynamics are based on the strip theory where the component of surge mode is not taken into account. Correspondingly, the three-dimensional boundary-value problems for diffraction (Eqs. (6.6) to (6.8)) and radiation (Eqs. (6.16) to (6.18)) reduce to the two-dimensional ones (see Appendixes D.1 and D.2), which are solved using the boundary element method. The boundary surface is subdivided into a number of straight lines with the Rankine source distribution of constant strength. The radiation condition is satisfied at a fictional surface set at a finite distance from the ship by the use of near and far field matching method. The finite distance is chosen to be equal to one wavelength from the ship but not less than one ship breadth. Because the mean wetted surface of the hull can change significantly during the flooding process, a database approach is used in PROTEUS3 to consider this influence on the hydrodynamic properties. In this approach, a set of hydrodynamic forces and coefficients are pre-calculated with the strip theory and stored in the database, and their transient values are interpolated from the stored values. The 6-DOF ship motion equation also reduces to the 5-DOF equation without surge motion (see Appendix D.3); the latter is solved in PROTEUS3 using the Runge-Kutta-Fehlberg method (Fehlberg, 1969). To account for the viscous effects outside the ship, in PROTEUS3, the well-known Ikeda's semi-empirical method (Himeno, 1981) is adopted to correct the roll damping. On the other hand, the fluid motion in the floodable compartments

and the neighborhood of the damaged ship section, as shown in Figure 6.1, is solved using the NS solver described in the previous chapter.

At each time step, the instantaneous ship motion is applied to the excitation of water motion in the compartments; the corresponding internal liquid loads obtained with the NS solver are added to the total external forces acting on the ship. Meanwhile, the hydrostatic and hydrodynamic forces/coefficients on the external hull surface are determined using the seakeeping solver. After all of the external forces are added together, the ship motion at next time step is determined by solving the 5-DOF motion equation (Eq. (D.26)). The solution procedure for the entire flooding problem is described in Figure 6.2.

6.3 Closure

In this chapter, a hybrid method, which couples an in-house seakeeping solver based on the potential flow method and a newly developed two-phase flow NS solver, has been presented to solve the flooding problem of a damaged ship in waves. The hydrostatic and hydrodynamic forces acting on the external hull surface were calculated using the seakeeping solver, whereas the internal liquid loads on the floodable compartments were obtained with the NS solver. Based on this hybrid model, the CFD simulation can focus on the complex phenomena of water flooding and sloshing, and hence most of the flow characteristic in the concerned fluid domain can be retained while greatly reducing the computational time.

Up to this point, all of the mathematical models and numerical methods adopted in our study have already been introduced. Verification and validation of the proposed methods for specific applications will be described in the following chapters.

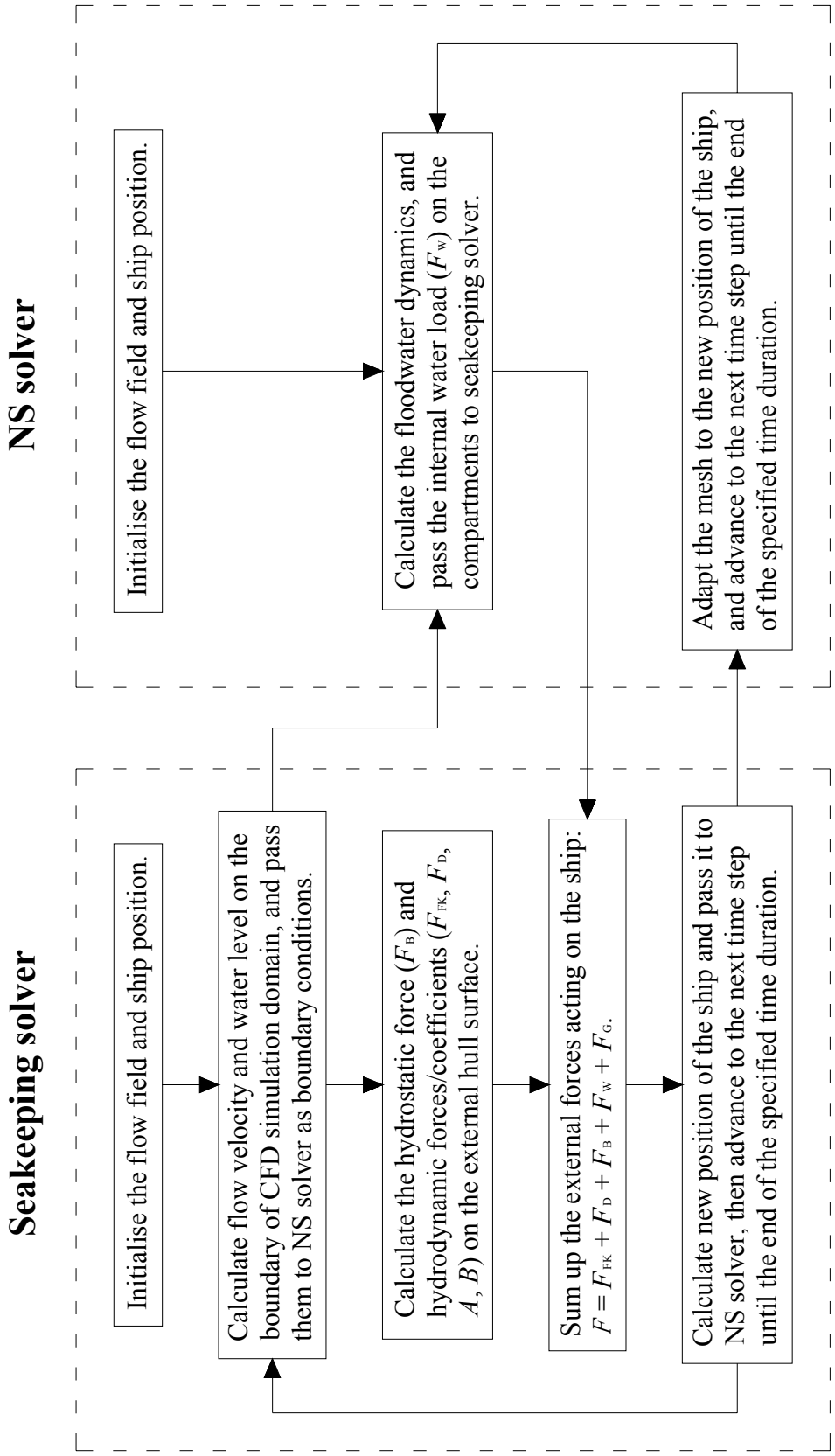

Figure 6.2: Outline of solution procedure for the hybrid method.

Chapter 7

Primary Test Cases of Free Surface Flow

To access its performance in solving two-phase flow problems, the developed NS solver is applied to three primary test cases including dam break, tank sloshing and compartment flooding. These three cases contain the elements which compose the damaged ship flooding, e.g., non-linear motion of free surface, water impact on structures, water motion under external excitation and obstacle influence on water motion. The results obtained are compared with experimental data, analytical solutions or other published numerical results. All computations are performed on a single-processor (Pentium 4, 3.0 Ghz) personal computer.

7.1 Dam Break Problem

First, the present NS solver is applied to the dam break problem, which is a popular and challenging test case to validate a numerical tool that addresses complex free surface motion exhibiting strong non-linear behaviour. In the following, the two- and three-dimensional dam break problems will be solved, respectively.

7.1.1 2-D Dam Break

A dam break flow experiment was performed in a tank measuring 3.22 m × 1 m × 1.8 m (Zhou et al., 1999), as shown in Figure 7.1. After the flap was lifted, the water with an initial water height (h_0) equal to 0.6 m flowed freely. The water heights and

pressure were measured using two water height probes (H1 and H2) and one pressure gauge (P1).

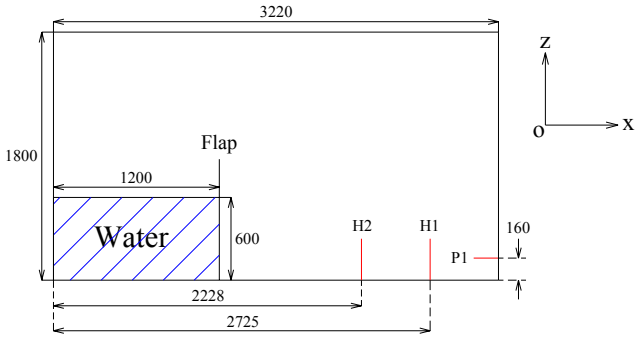

Figure 7.1: Sketch of the 2-D dam break experiment (units: mm).

The above dam break problem can be considered as a two-dimensional flow problem. The no-slip wall condition, which requires the fluid to stick to the wall, is imposed on the entire boundary. Referring to the verification approach presented by Stern et al. (2001), we first carry out the time and grid dependence study in the context of this dam break case. The variables selected for the study are the water height at H1 and the impact pressure at P1. The change (ε) between solutions at the coarser and finer levels of time step or grid size is defined by $\varepsilon=(\phi_{\text{finer}}-\phi_{\text{coarser}})/\phi_{\text{r}}$, where ϕ_{finer} and ϕ_{coarser} represent the solutions at the finer and coarser levels, respectively; ϕ_{r} represents the reference quantity of variables, which is equal to h_0 for the water height and $\rho g h_0$ (ρ the water density) for the impact pressure.

For the time dependence study, three time steps with refinement ratio of 2 as listed in Table 7.1 and a mesh with uniform element arrangement ($\delta x=\delta z=0.02$ m) in the x- and z-directions are used. It takes 1.4, 2.1 and 3.2 CPU hours to finish 2.5 s simulation with large, medium and small time step, respectively. The comparisons of computed results are shown in Figures 7.2 and 7.3, where the mean change ($\varepsilon_{\text{mean}}$) is defined by $\varepsilon_{\text{mean}}=\left(\sum_{i=1}^{n}\left|\varepsilon_i\right|\right)\Big/n$. It is apparent that the results computed with the three time steps are nearly identical until $t\sqrt{(g/h_0)}=6$, after which the water wave breaks

and the differences between the results become obvious. Table 7.2 summarizes the time dependence study results, e.g., convergence ratio (R_T), order of accuracy (p_T), correction factor (C_T), simulation numerical error (δ_T) and uncertainty (U_T). Note that δ_T and U_T are estimated depending on how close C_T is to 1. For C_T considered as sufficiently less than or greater than 1 and lacking confidence, U_T is estimated, but not δ_T. For C_T considered close to 1 and having confidence, both δ_T and U_T are estimated.

Table 7.1: Time steps used in the time dependence study for the 2-D dam break case.

Time step	Large	Medium	Small
δt (s)	0.002	0.001	0.0005

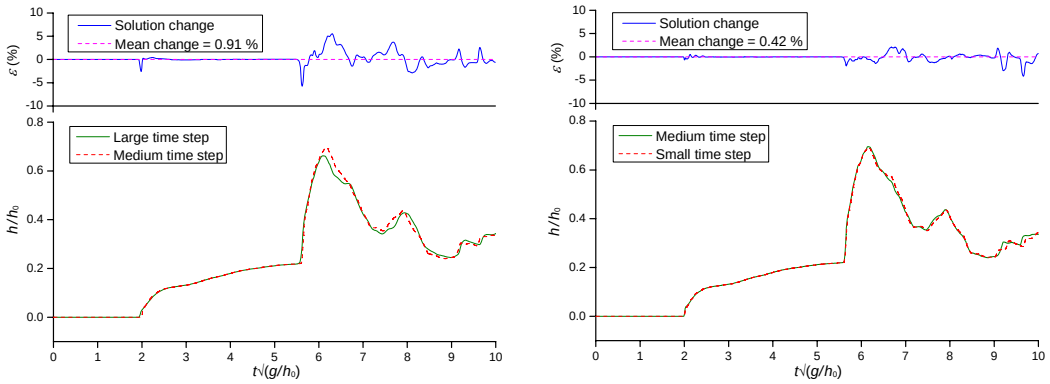

Figure 7.2: Comparison of vertical water height computed with different time steps at H1.

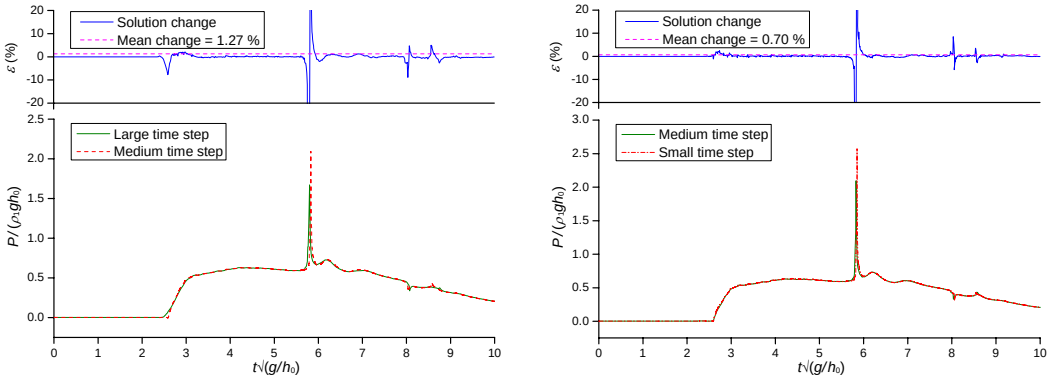

Figure 7.3: Comparison of impact pressure computed with different time steps at P1.

Table 7.2: Results of time dependence study for the 2-D dam break case.

Variable	R_T	p_T	C_T	For $\lvert 1-C_T \rvert \gg 0$	For $\lvert C_T \rvert \approx 1$	
				U_T	δ_T	U_T
Water height	0.46	1.12	1.18	0.48 %	0.42 %	0.06 %
Impact pressure	0.55	0.85	0.81	0.87 %	0.70 %	0.17 %

For the grid dependence study, a time step of 0.0005 s and three meshes with refinement ratio of √2 as listed in Table 7.3 are used. The element sizes (δx and δz) of mesh are uniform in the x- and z-directions. It takes 1.2, 3.2 and 6.7 CPU hours to finish 2.5 s simulation on coarse, medium and fine grids, respectively. The comparisons of numerical results are shown in Figures 7.4 and 7.5. It is apparent that the results as calculated using different grids are in good agreement at the initial stage. After $t\sqrt{(g/h_0)}>6$, the results obtained on coarser gird differ largely from those on finer grid. The results of grid dependence study are summarized in Table 7.4.

Table 7.3: Meshes employed in the gird dependence study for the 2-D dam break case.

Grid	$x \times z$	δx (m)	δz (m)	Total number of elements
Coarse	114 × 64	0.0282	0.0282	7,296
Medium	161 × 90	0.0200	0.0200	14,490
Fine	228 × 127	0.0141	0.0141	28,956

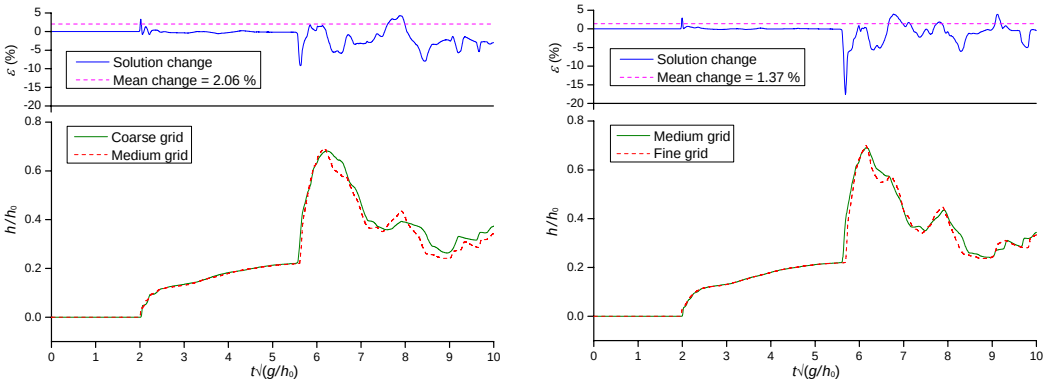

Figure 7.4: Comparison of vertical water height computed with different meshes at H1.

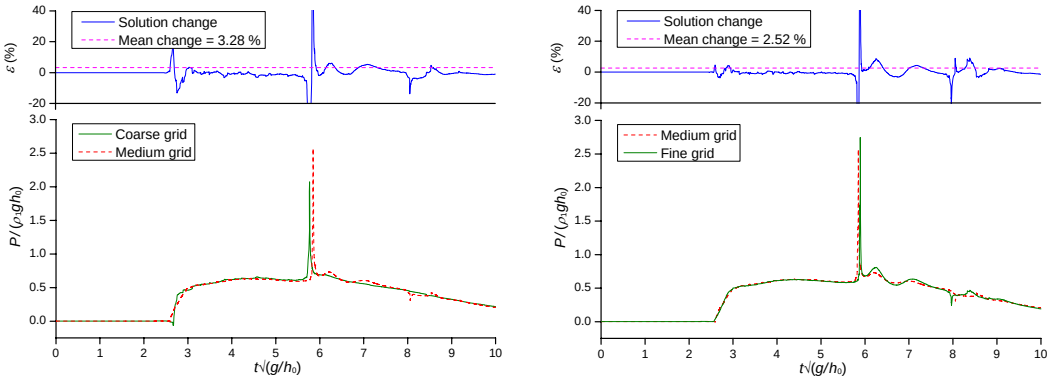

Figure 7.5: Comparison of impact pressure computed with different meshes at P1.

Table 7.4: Results of grid dependence study for the 2-D dam break case.

Variable	R_G	p_G	C_G	For $\lvert 1-C_G \rvert \gg 0$	For $\lvert C_G \rvert \approx 1$	
				U_G	δ_G	U_G
Water height	0.66	1.18	1.22	3.90 %	3.31 %	0.60 %
Impact pressure	0.77	0.76	0.73	8.35 %	6.08 %	2.27 %

In fact the time sensitivity of numerical results is associated with the cell Courant number that involves the performance of the CICSAM scheme (see Eqs. (B.26) and (B.27)). A convection test, which is commonly used for validation of interface capturing schemes, was conducted by Ubbink (1997) to investigate the influence of cell Courant number limit ($Co_{\lim}$) on the accuracy of the CICSAM scheme. It demonstrated that the selection of $Co_{\lim}$ around 0.25 can ensure acceptable numerical accuracy whilst making most efficient use of available computer resources. In the remainder of present chapter, all computations are carried out with variable time step to keep the cell Courant number within the limit of 0.25 (see Eq. (5.15)).

Now the computed results are compared with the experimental results and with other numerical results obtained by the SPH method (Colagrossi and Landrini, 2003). The fine grid listed in Table 7.3 is employed. It uses 4.2 CPU hours in this computation. The interface profile calculated using the present method and the SPH method are shown in Figure 7.6. At the initial stage, the flow is smooth and moves with a simple interface. The interface profiles obtained by the two methods are similar. After the

water wave overturns and breaks, the flow becomes violent and the interface profile differences between the two methods are obvious.

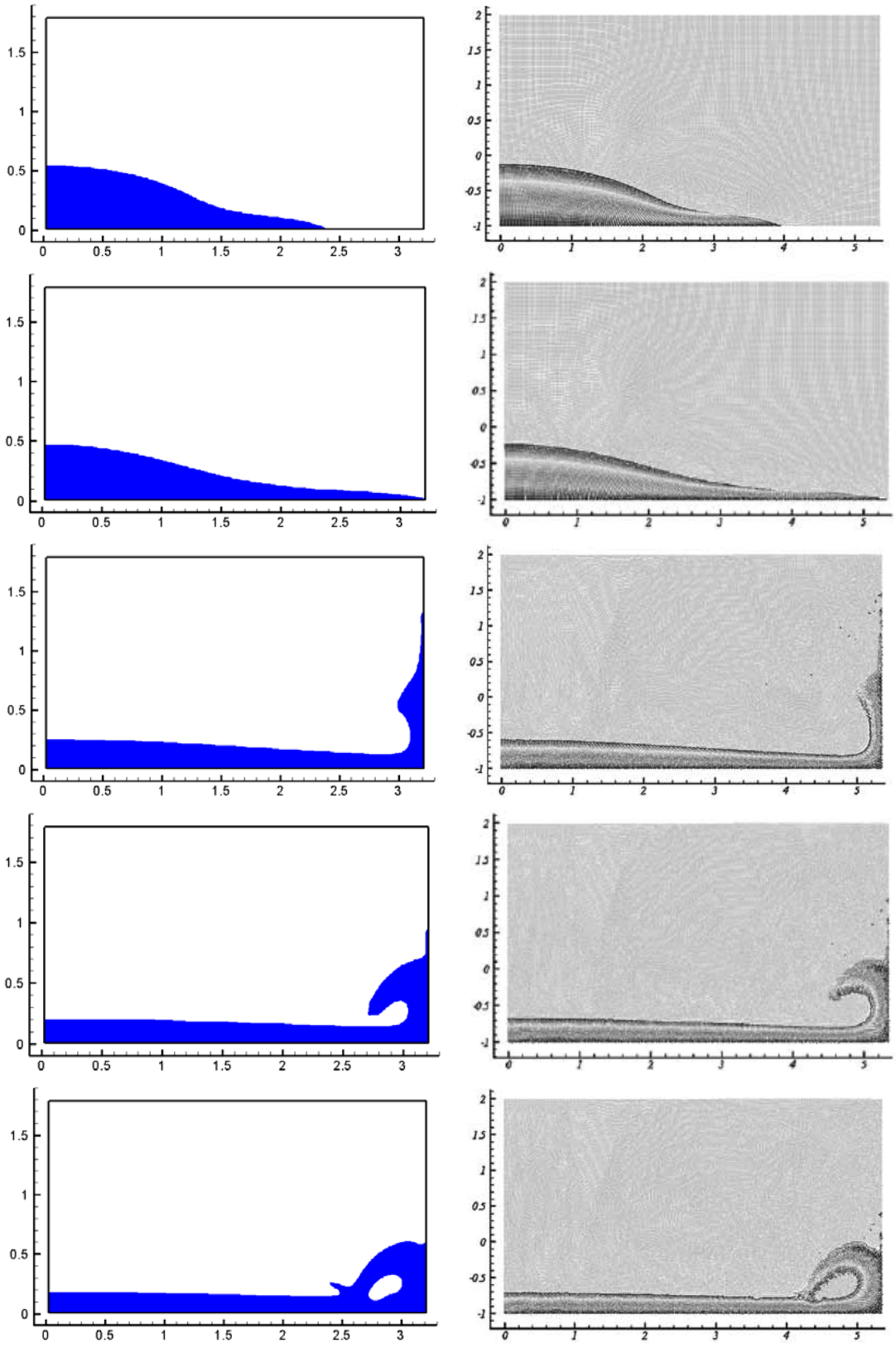

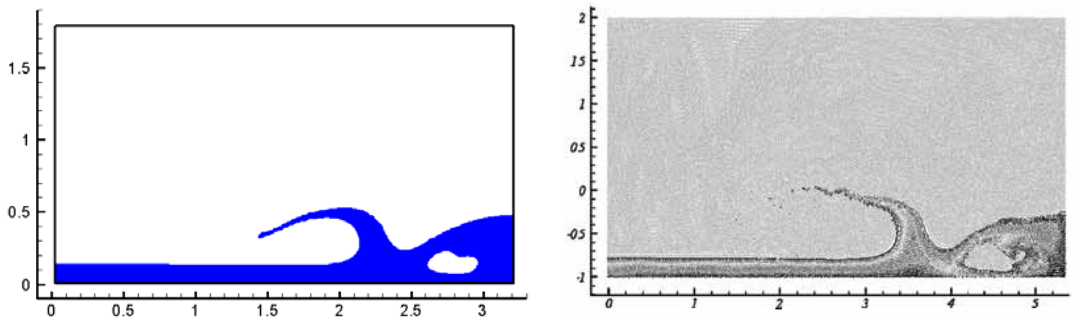

Figure 7.6: Snapshots of 2-D dam break process ($t\sqrt{(g/h_0)}$=1.66, 2.43, 4.81, 5.72, 6.17, 7.37) (Left: present computation, right: SPH computation).

Figures 7.7 and 7.8 compare the water heights. It is apparent that the present results initially agree well with the published results. However, the results obtained from the numerical simulations and model test disagree when $t\sqrt{(g/h_0)}>6$. Because of the experimental difficulties in measuring the water level of chaotic flow and the limited information about the experiment, further discussion of these inconsistencies is not appropriate. A comparison of the pressure histories is shown in Figure 7.9. It is clear that the present numerical results compare well with the experimental results. Compared to the SPH method, the first peak appearing around $t\sqrt{(g/h_0)}=6$, which is a result of the overturning water hitting the free surface, is better predicted by the present method. The frequency of pressure oscillations associated with entrapped air bubble pulsations is much higher in the SPH computation than that in the present computation and model test.

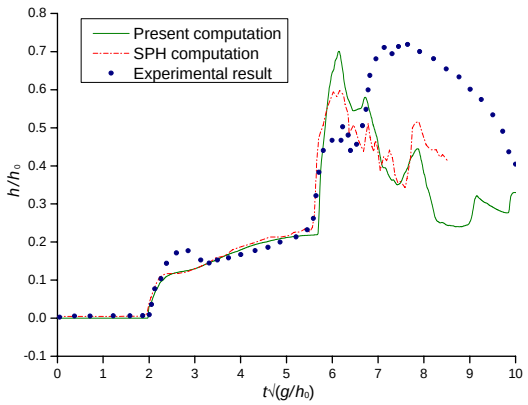

Figure 7.7: Comparison of the time history for vertical water height at H1.

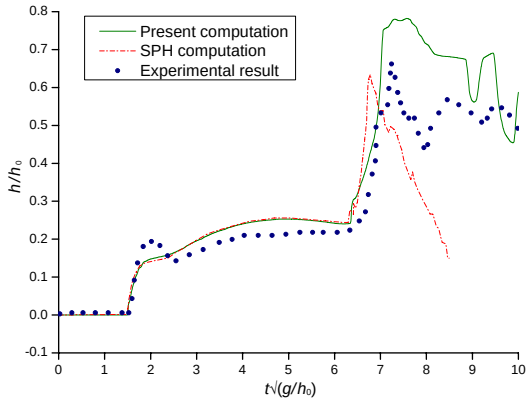

Figure 7.8: Comparison of the time history for vertical water height at H2.

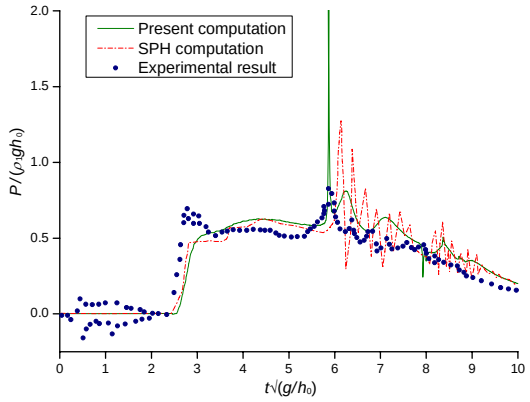

Figure 7.9: Comparison of the time history for impact pressure at P1.

7.1.2 3-D Dam Break

Another model test was performed to investigate the impact of dam break flow on a structure (Kleefsman et al., 2005). The setup of the test is illustrated in Figure 7.10. A tank with dimensions 3.22 m × 1 m × 1 m and with an open roof was used in the experiment. The right part of the tank was initially sealed with a door, behind which a column of water with 0.55 m height was placed. When the door was opened, the water flowed into the void and impacted the box that had been placed in the tank. Water height and pressure measurements were acquired during the experiment. Four water height probes (H1, H2, H3 and H4) were placed in the tank. The box was covered with eight pressure sensors: four on the front of the box and four on the top. The positions of the sensors are shown in Figure 7.11.

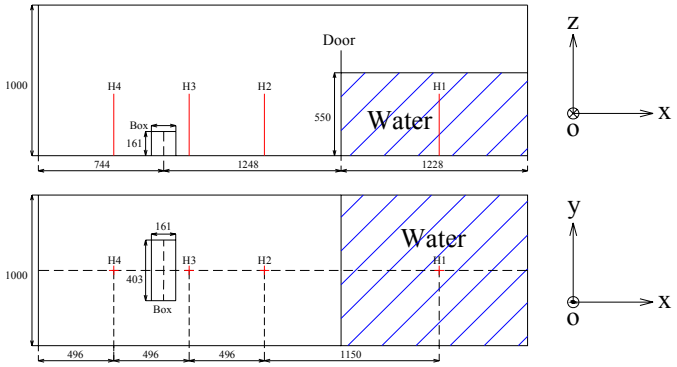

Figure 7.10: Sketch of the 3-D dam break experiment (units: mm).

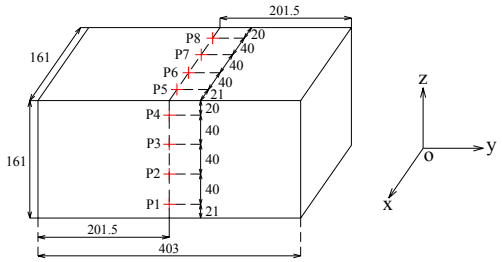

Figure 7.11: Locations of the pressure sensors placed on the box (units: mm).

In the present computation, a tank with dimensions 3.22 m × 1 m × 1.4 m is used, which is somewhat different from the one used in the model test. The pressure is set to be 101325 Pa on the top boundary of the tank. The no-slip wall condition is imposed on the other boundaries. A mesh with uniform element arrangement in the *x*-, *y*- and *z*-directions is employed. The element sizes (δx, δy and δz) are 0.02 m. The total number of elements in the numerical computation is 554,170. The numerical simulation runs up to 6 s. It uses 183 CPU hours in this computation.

The snapshots in Figure 7.12 demonstrate the dam break process. The smaller pictures inside the snapshots show the water in the right part of the tank. When the door is opened, the water flows into the left part of the tank smoothly. After the water impacts the box, the flow becomes violent and wave breaking is observed. The chaotic water reaches the back wall and overturns. Then, the water flows back with broken waves. The numerical simulation reproduces the process of complex free surface motion well in comparison with the model test.

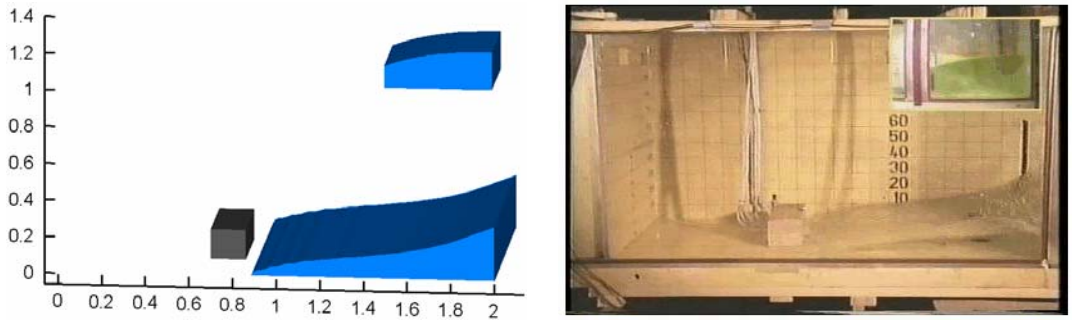
1.4
1.2
1
0.8
0.6
0.4
0.2
0
0 0.2 0.4 0.6 0.8 1 1.2 1.4 1.6 1.8 2
60
50
40
30
20
10

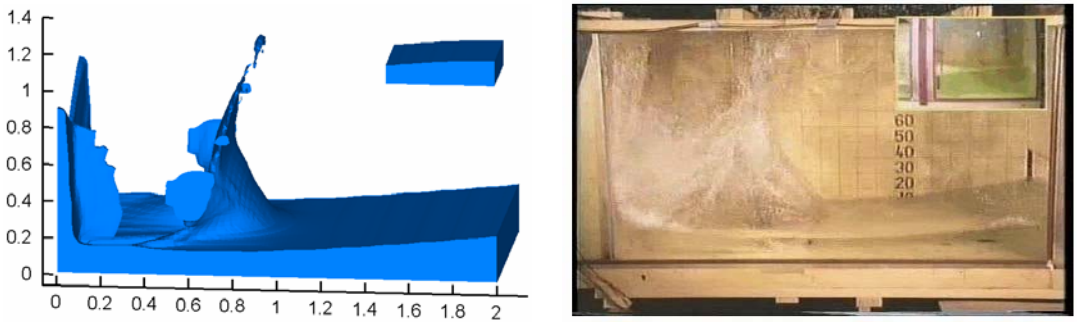
1.4
1.2
1
0.8
0.6
0.4
0.2
0
0 0.2 0.4 0.6 0.8 1 1.2 1.4 1.6 1.8 2
60
50
40
30
20

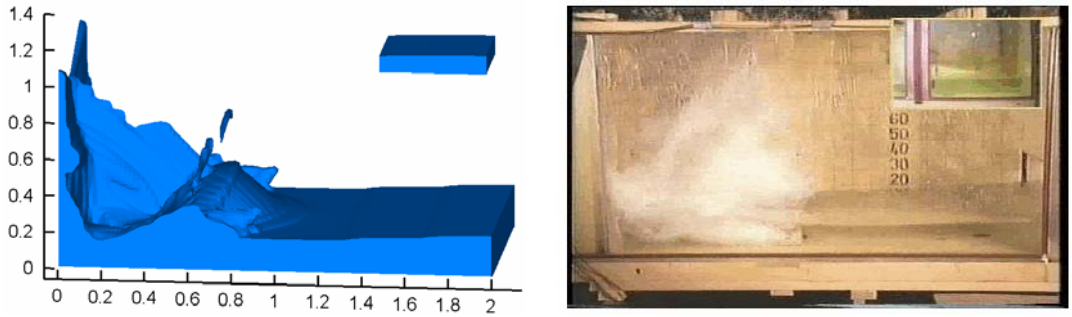
1.4
1.2
1
0.8
0.6
0.4
0.2
0
0 0.2 0.4 0.6 0.8 1 1.2 1.4 1.6 1.8 2
60
50
40
30
20

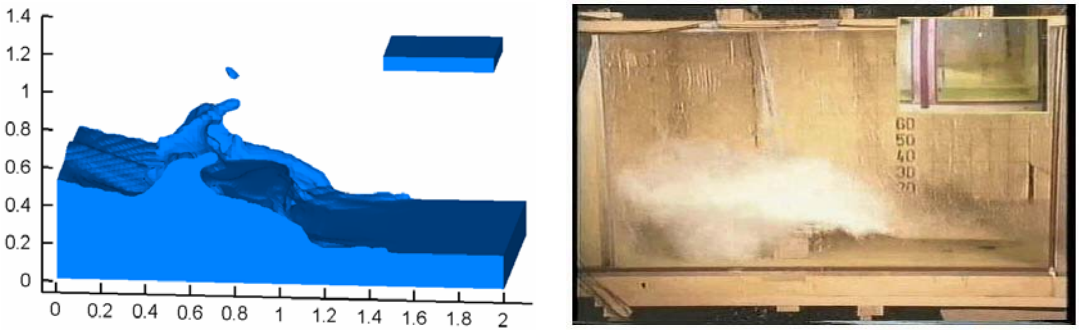
1.4
1.2
1
0.8
0.6
0.4
0.2
0
0 0.2 0.4 0.6 0.8 1 1.2 1.4 1.6 1.8 2
60
50
40
30

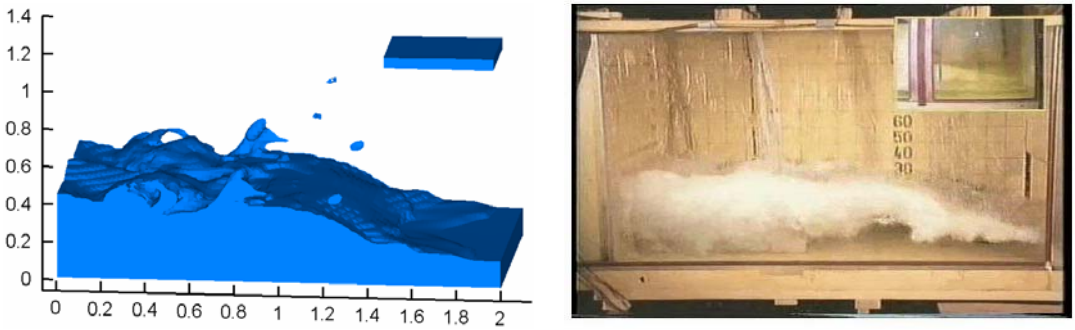
1.4
1.2
1
0.8
0.6
0.4
0.2
0
0 0.2 0.4 0.6 0.8 1 1.2 1.4 1.6 1.8 2
60
50
40
30

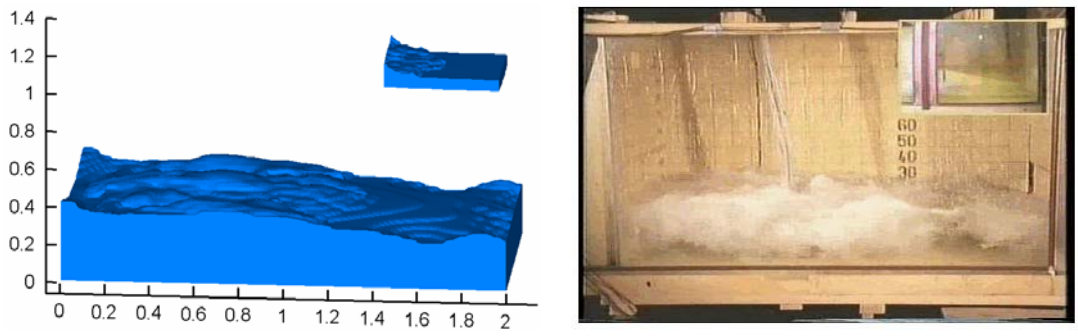

Figure 7.12: Snapshots of 3-D dam break process (t=0.4, 0.8, 1.2, 1.4, 2.0, 2.4 s) (Left: present computation, right: model test).

Water height comparisons are shown in Figures 7.13 through 7.16. The agreements between numerical and experimental results are comparatively good at the initial stage. After the water returns from the back wall, the differences of water heights obtained with computation and model test become larger, especially for the comparison at H4. The snapshots of model test in Figure 7.12 show that the water flows back mixing with large numbers of air bubbles. However, our numerical method can not capture this physical characteristic accurately because the mechanisms of bubble coalescence and breakup are not included in the present mathematical model. Therefore large discrepancies between numerical and experimental results are observed during this period. At the later stage, the change trends of computed and measured water height as a function of time are in good agreement, although phase lags between computation and experiment are observed. Generally, the global behaviour of dam break flow as predicted by the present method agrees with the experimental one. Figures 7.17 and 7.18 compare the pressure histories at the front of the box. Two significant peaks are observed in the figures. The first peak, at around 0.4 s, is a result of the initial impact. The magnitude of the peak at P1 is well predicted by the present method according to the experimental data, but it is under-predicted at P3. The second peak, at around 4.8 s, results from the water hitting the box again. Generally, good agreement between the numerical and experimental results is obtained. The pressure history comparisons for

the top of the box are shown in Figures 7.19 and 7.20. The numerical results are generally consistent with the experimental data except for the period of 1.5 s to 2.7 s, when the backflow with air bubbles impacts on the top of the box.

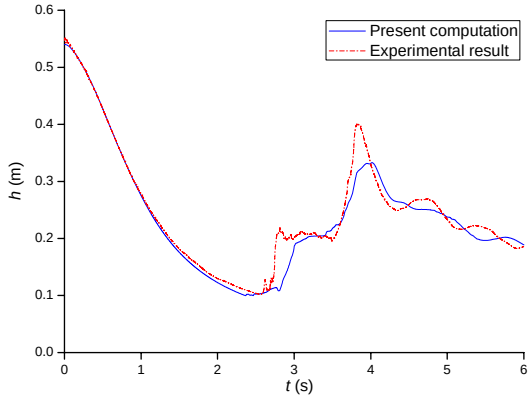

Figure 7.13: Comparison of the time history for vertical water height at H1.

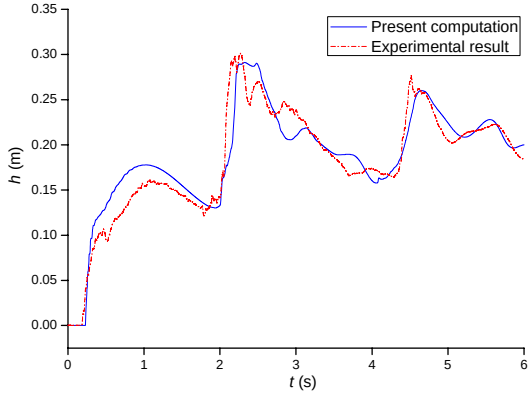

Figure 7.14: Comparison of the time history for vertical water height at H2.

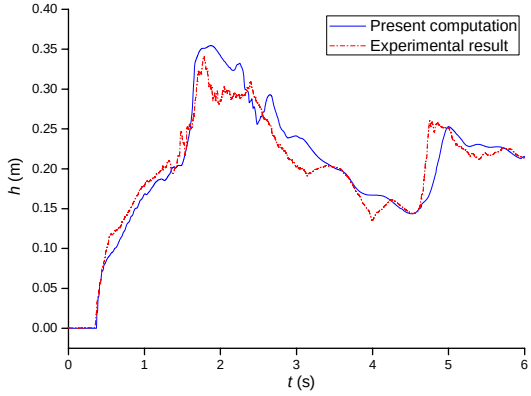

Figure 7.15: Comparison of the time history for vertical water height at H3.

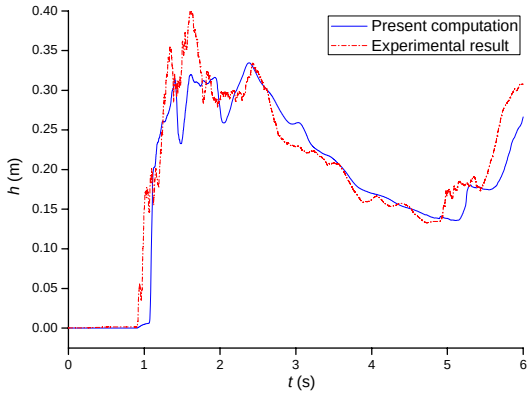

Figure 7.16: Comparison of the time history for vertical water height at H4.

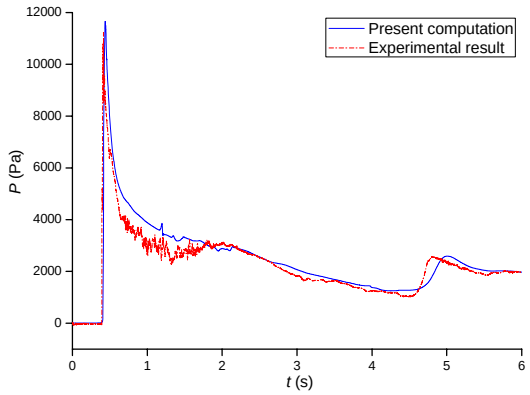

Figure 7.17: Comparison of the time history for impact pressure at P1.

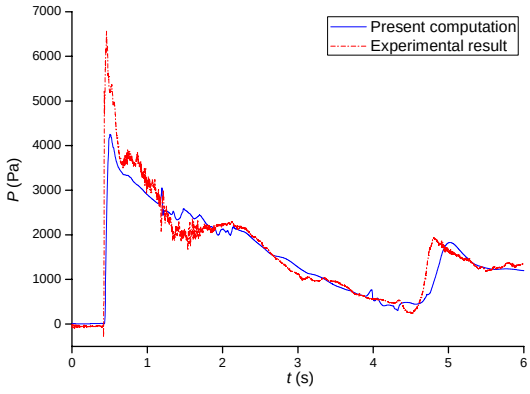

Figure 7.18: Comparison of the time history for impact pressure at P3.

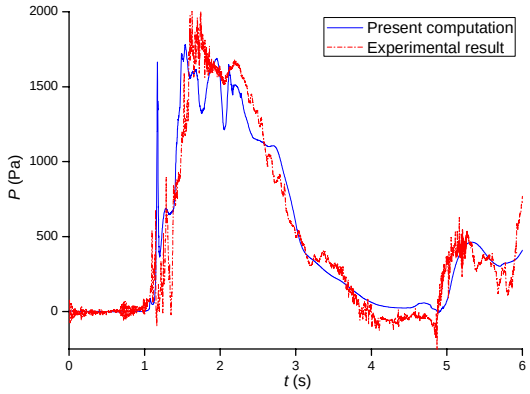

Figure 7.19: Comparison of the time history for impact pressure at P5.

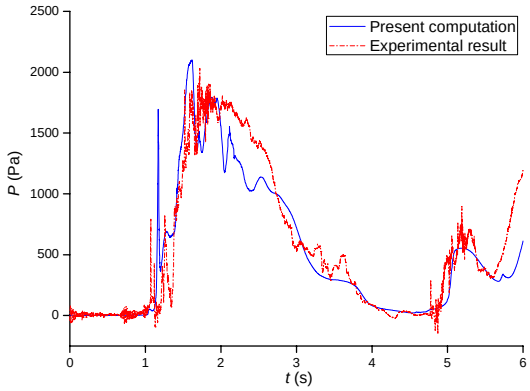

Figure 7.20: Comparison of the time history for impact pressure at P7.

7.2 Tank Sloshing Problem

The proposed method is then used to solve the tank sloshing problem. Experiments of liquid sloshing in a horizontally excited hexahedral tank have been reported by Liu and Lin (2008). The tank is 0.57 m long, 0.31 m wide and 0.3 m high. The still water depth is 0.15 m. The lowest natural frequency (ω_0) of liquid motion in the tank is 6.0578 s^{-1}. The tank is secured on a shaker whose movement follows the sinusoidal function: $x=-a\sin(\omega t)$. The shaking amplitude (a) is 0.005 m and the frequencies (ω) are $0.583\omega_0$ and $1.0\omega_0$, which correspond to the non-resonance and resonance cases, respectively. The tank is equipped with water height probes (H1, H2 and H3) to measure the elevation of the water surface. The experimental setup is shown in Figure 7.21.

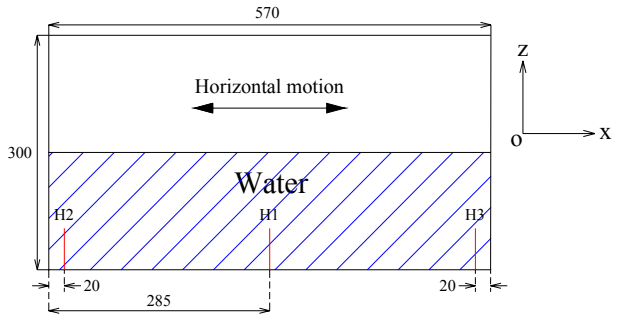

Figure 7.21: Sketch of the sloshing experiment (units: mm).

The above sloshing problem can be simplified to a two-dimensional problem. There are two methods to account for the effect of a moving tank in the numerical simulation. One is to simulate the actual movement of the tank, in which the mesh follows the tank motion. The other is to solve the problem on a non-inertial, body-fixed coordinate system (BS) that moves along with the tank, and hence the mesh can keep static during the computation. The latter method is adopted in the present study. In the BS, the NS equation is modified by adding an external acceleration on its right-hand side (see Appendix E). For the present sloshing case, the x-component of external acceleration ($-a\omega^2\sin(\omega t)$) is added. The no-slip wall condition is imposed on the entire boundary.

A grid resolution investigation is carried out. For the non-resonance case (ω=0.583ω_0), three meshes described in Table 7.5 are generated. The element size (δx) is uniform in the x-direction, whereas in the z-direction, the element size (δz) varies and more elements are distributed near the free surface. It takes 0.4, 0.9 and 2.3 CPU hours to finish 10.0 s simulation on coarse, medium and fine grids, respectively. For the resonance case (ω=1.0ω_0), the three meshes given in Table 7.6 are employed. The element sizes (δx and δz) are uniform in the x- and z-directions. It takes 0.6, 1.8 and 3.6 CPU hours to finish 7.0 s simulation on coarse, medium and fine grids, respectively. Comparisons of the numerical results from the three grids are shown in Figures 7.22 through 7.27. The results indicate that more elements are needed to better capture the behaviour of water moving with small-amplitude motion.

As can be seen in Figure 7.22 and in the initial stage of Figure 7.25, the numerical results obtained by the coarse grid differ from those obtained by the medium and fine grids, whereas the results obtained with the two higher resolution grids are in good agreement. In the case of large amplitude motion, the numerical results obtained by the three grid resolutions are nearly identical.

Table 7.5: Meshes employed in the gird dependence study for the non-resonance sloshing case.

Grid	$x \times z$	δx (m)	min δz (m)	Number of elements near the free surface in z-direction	Total number of elements
Coarse	57 × 50	0.010	0.0010	20	2,850
Medium	81 × 70	0.007	0.0007	30	5,670
Fine	114 × 90	0.005	0.0005	40	10,260

Table 7.6: Meshes employed in the gird dependence study for the resonance sloshing case.

Grid	$x \times z$	δx (m)	δz (m)	Total number of elements
Coarse	57 × 60	0.010	0.005	3,420
Medium	81 × 100	0.007	0.003	8,100
Fine	114 × 150	0.005	0.002	17,100

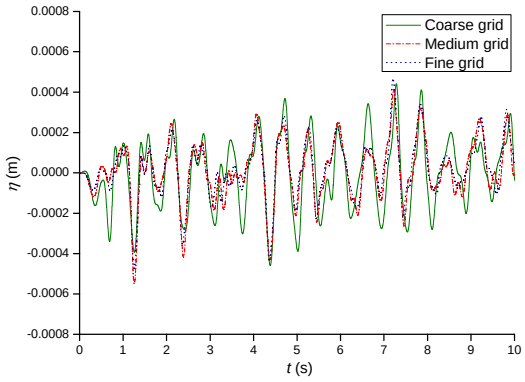

Figure 7.22: Comparison of numerical results for free surface elevation at H1 (ω=0.583ω_0).

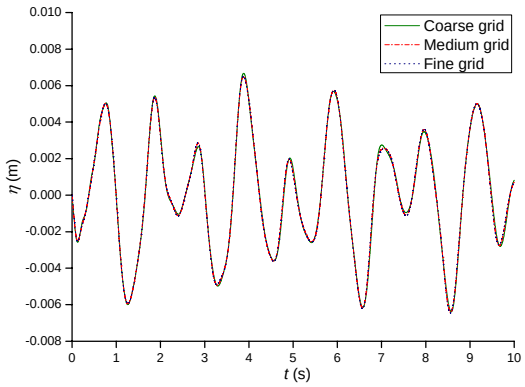

Figure 7.23: Comparison of numerical results for free surface elevation at H2 (ω=0.583ω_0).

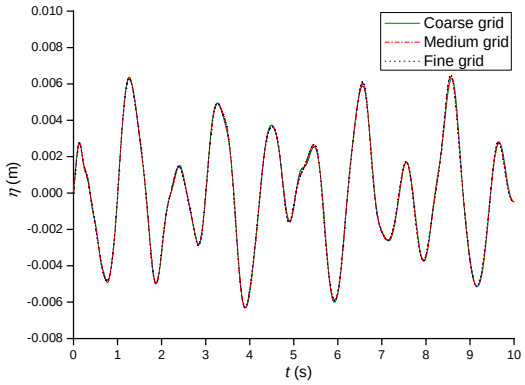

Figure 7.24: Comparison of numerical results for free surface elevation at H3 (ω=0.583ω_0).

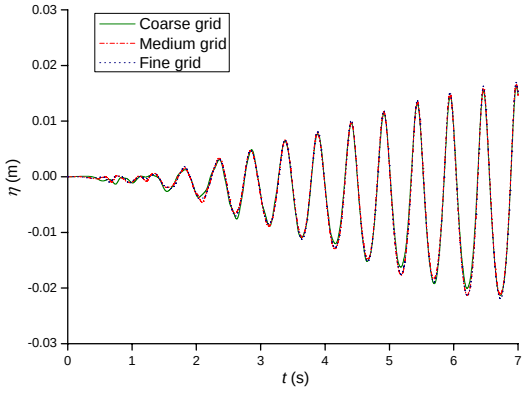

Figure 7.25: Comparison of numerical results for free surface elevation at H1 (ω=1.0ω_0).

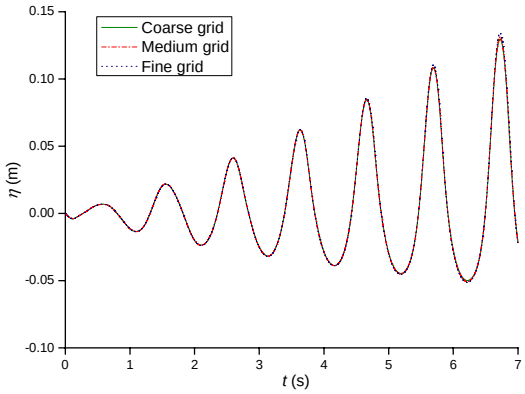

Figure 7.26: Comparison of numerical results for free surface elevation at H2 (ω=1.0ω_0).

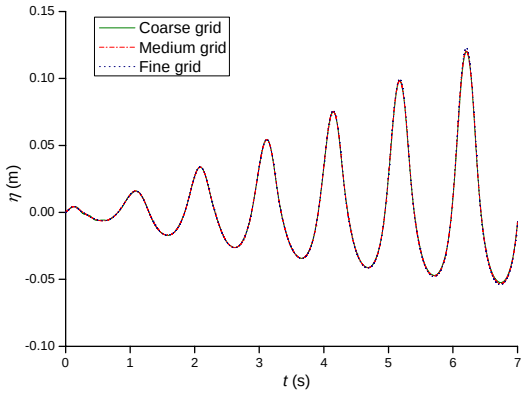

Figure 7.27: Comparison of numerical results for free surface elevation at H3 (ω=1.0ω_0).

Our numerical results can be validated with the experimental data and analytical solutions (Faltinsen, 1978). For the non-resonance case, the fine grid described in Table 7.5 is employed. The calculated free surface elevation is compared with other published results, as shown in Figures 7.28 through 7.30. It is apparent that the present results are in good agreement with the published results. For the resonance case, the fine grid described in Table 7.6 is employed. Figures 7.31 through 7.33 show the comparisons of free surface elevation. The linear analytical solution clearly fails to predict the behaviour of non-linear wave, i.e., the wave crest becomes sharper and the trough becomes flatter; however, this typical phenomenon is simulated well by the present method and we see a fairly good agreement between the numerical

results and experimental data.

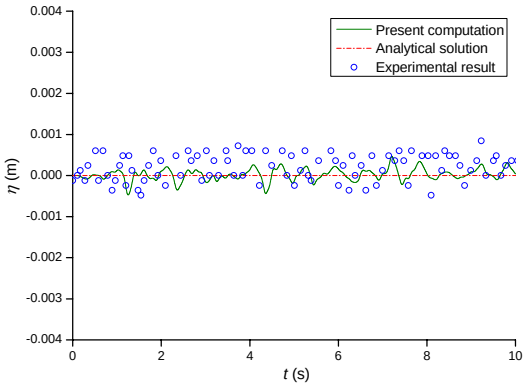

Figure 7.28: Comparison of the time history for free surface elevation at H1 (ω=0.583ω_0).

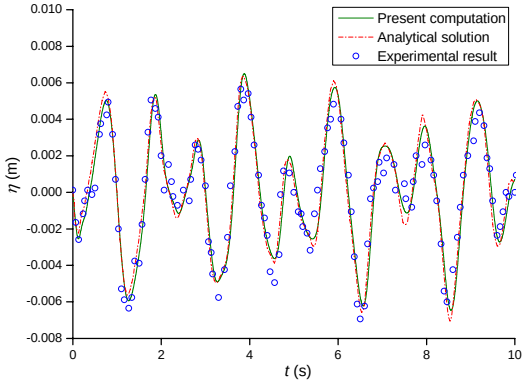

Figure 7.29: Comparison of the time history for free surface elevation at H2 (ω=0.583ω_0).

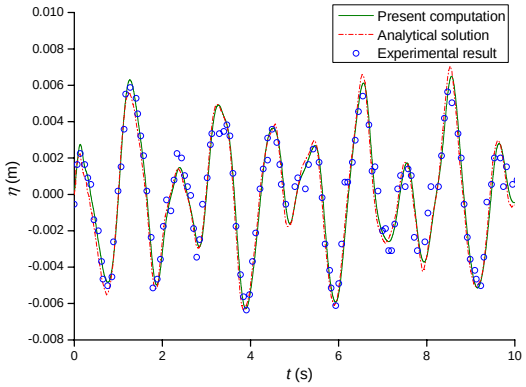

Figure 7.30: Comparison of the time history for free surface elevation at H3 (ω=0.583ω_0).

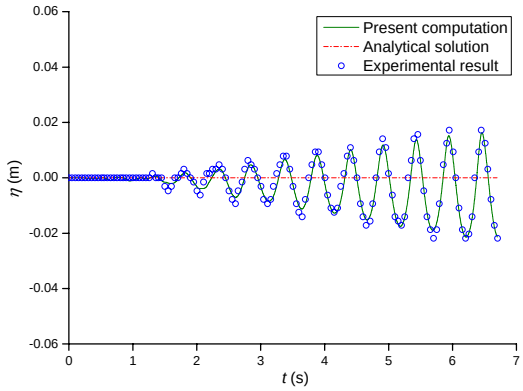

Figure 7.31: Comparison of the time history for free surface elevation at H1 (ω=1.0ω_0).

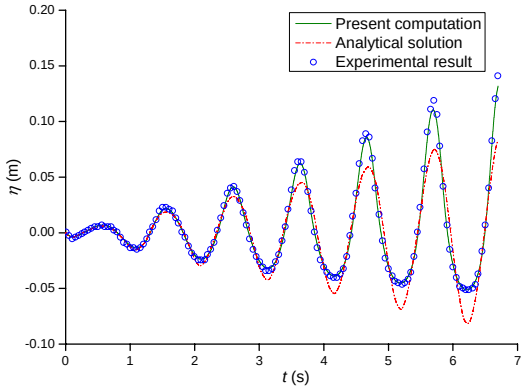

Figure 7.32: Comparison of the time history for free surface elevation at H2 (ω=1.0ω_0).

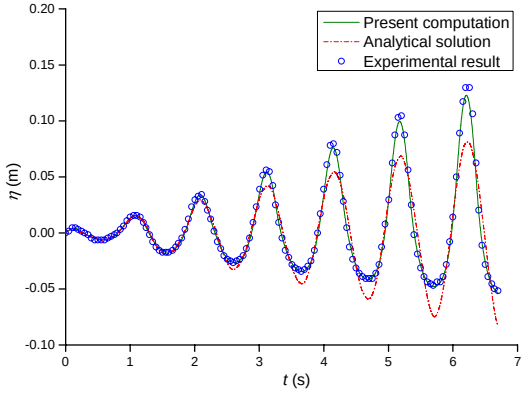

Figure 7.33: Comparison of the time history for free surface elevation at H3 (ω=1.0ω_0).

7.3 Compartment Flooding Problem

The final application of our solver presented in this chapter is analysis of floodwater dynamics in the damaged compartments. Cho et al. (2005) conducted a series of model tests, shown in Figure 7.34, to study water flooding into a damaged compartment of a Ro-Ro ferry. Two models of the damaged compartment were adopted in their study: the actual model and the simplified model, both of which are shown in Figure 7.35. The main parameters of the model are given in Table 7.7. The floating positions and attitudes of the models were fixed in the experiments.

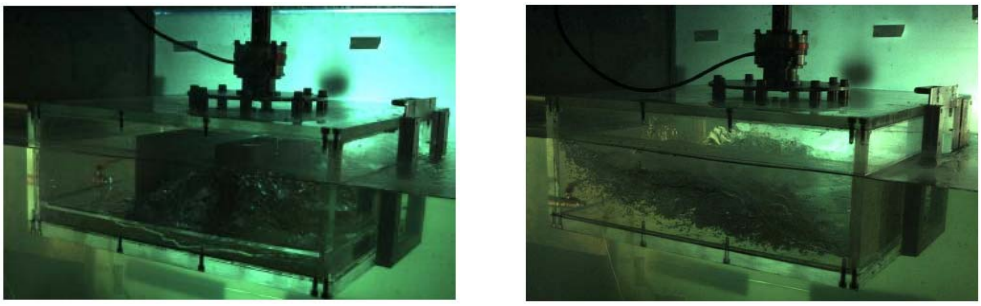

Figure 7.34: Model tests of water flooding into damaged compartments.

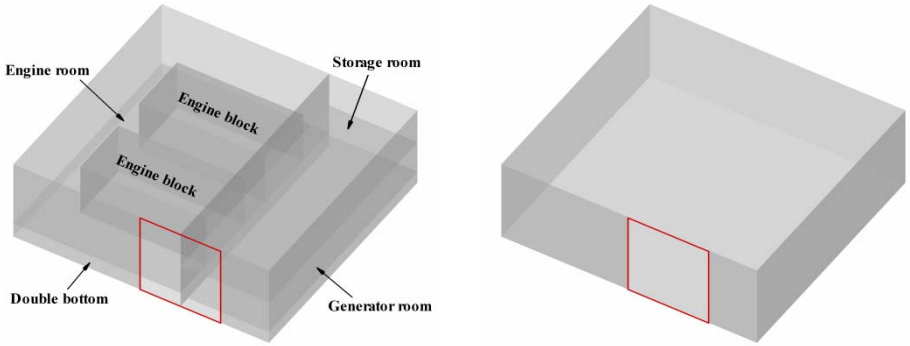

Figure 7.35: Models of damaged compartment (Left: actual model, right: simplified model).

Table 7.7: Main dimensions of the damaged compartment (unit: m).

Length (L)	Breadth (B)	Height (H)	Draft (D)	Engine block	Damaged length
0.55	0.515	0.186	0.132	0.271 × 0.132 × 0.118	0.17

Because the air compressibility has not been considered in our developed solver, for the actual model of the compartment, three ventilation holes are opened on the decks to ensure that the air in the double bottom and generator room can escape during the numerical simulation. The holes are 0.03 m × 0.03 m in size, and their positions are shown in Figure 7.36. In order to avoid significant boundaries effect on the flow around the compartment, the computational domain is extended to 3L on the left and right, 3B on the front and back, and 1H on the bottom, as show in Figure 7.37. The pressure is set to be 101325 Pa on the top boundary of the computational domain. On the left, right, front and back boundaries of the computational domain, the water level is set to be H+D and the hydrostatic pressure is imposed to make the water level outside the compartment maintain around the initial water height. The no-slip wall boundary condition is imposed on the compartment and on the bottom boundary of the computational domain. The meshes employed in the computation are given in Table 7.8. Inside the damaged compartment, the element size magnitudes in the x-, y- and z-directions are 0.01 m, whereas outside the compartment, the element sizes vary and become larger away from the compartment with expansion factor of approximately 1.2. Figure 7.38 shows the outline of mesh arrangement in the computational domain.

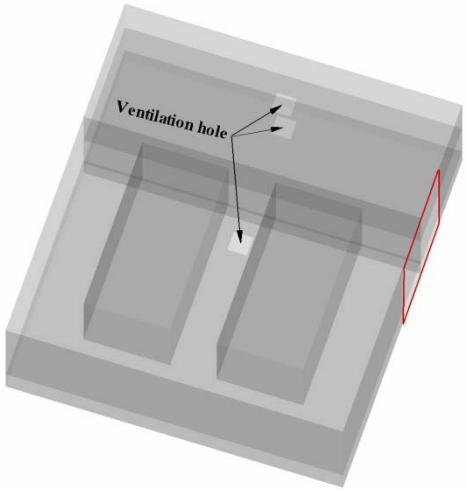

Figure 7.36: Ventilation holes on the decks of the actual model.

Table 7.8: Meshes employed for the compartment flooding cases.

Model	Number of elements in region 1	Number of elements in region 2	Total number of elements
Simplified model	51,408	175,728	227,136
Actual model	44,871	180,120	224,991

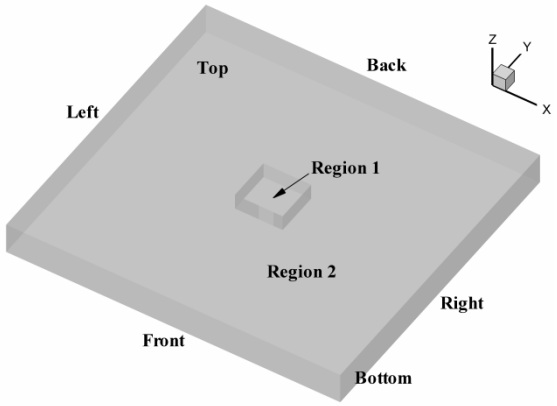

Figure 7.37: Computational domain of compartment flooding.

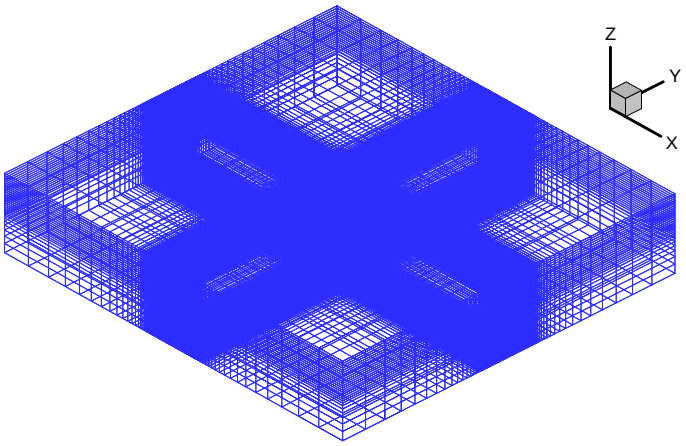

Figure 7.38: Sketch of the mesh arrangement in the computational domain.

The simulations of water flooding process run up to 10 s. It uses 33 CPU hours for the simplified model case and 59 CPU hours for the actual model case. The numerical prediction of floodwater motion in the simplified model is shown in Figure 7.39. The water floods into the damaged compartment promptly and reaches the opposite wall in 0.43 s. Then, an overturning wave is formed and the flow becomes violent. The flow returns to the inlet in 1.29 s. Figure 7.40 shows the

floodwater motion in the actual model. Initially, the floodwater motion in the storage room and generator room is similar to that in the simplified model, but in the engine room, a large amount of floodwater is blocked by the engine and accumulates around the inlet. After 0.645 s, the floodwater behaviour in the two models differs significantly. The *z*-direction force comparisons that reflect the flow magnitude through the opening are shown in Figure 7.41. We note that water ingress into the actual model is slower than that in the simplified model because of the block effect of the engines. For the case of simplified model, the compartment is almost filled after 4 s which is approximately 2 s earlier than the one happens in the actual model case. The change trends of the computed *z*-direction force are in good agreement with the experimental data, which indicates that the ingress of floodwater as calculated by the proposed method is consistent with experimental results.

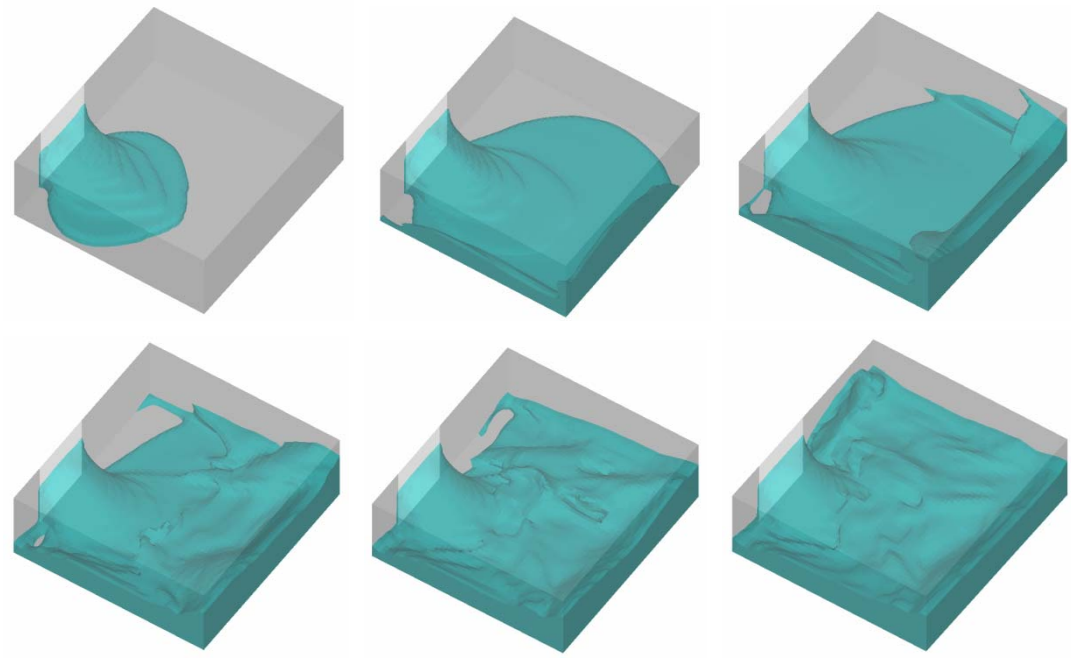

Figure 7.39: Snapshots of floodwater in the simplified model (t=0.215, 0.43, 0.645, 0.86, 1.075, 1.29 s).

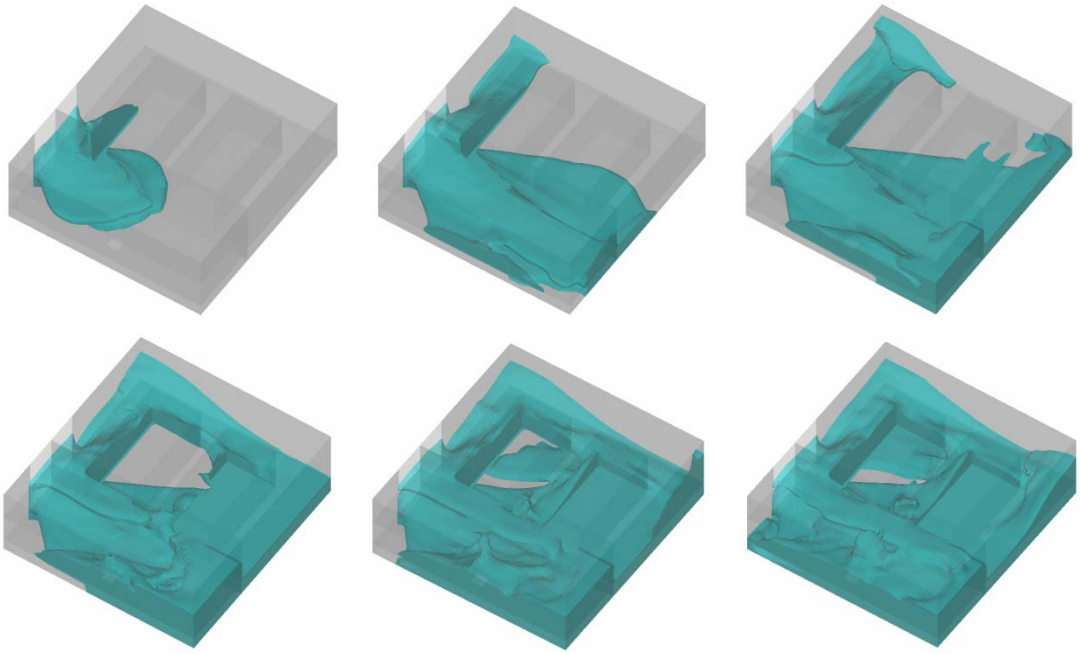

Figure 7.40: Snapshots of floodwater in the actual model (t=0.215, 0.43, 0.645, 0.86, 1.075, 1.29 s).

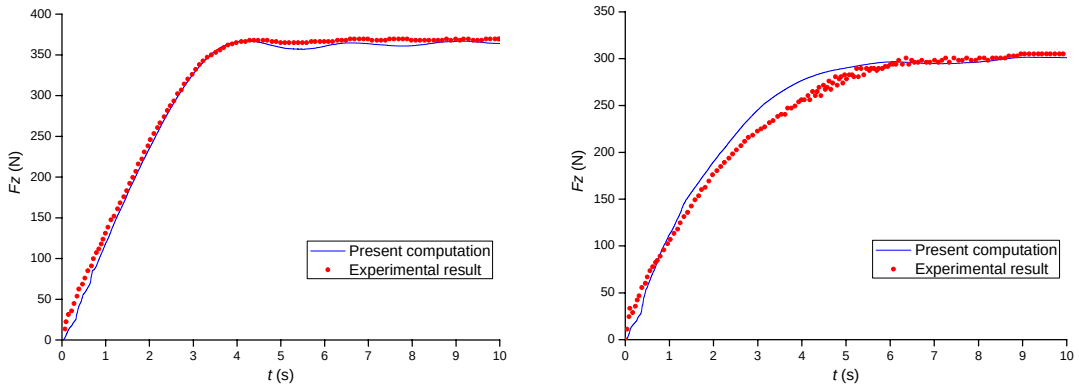

Figure 7.41: Comparison of the time history for z-direction force (Left: simplified model, right: actual model).

7.4 Closure

In this chapter, three various cases which are all related to the damaged ship flooding have been used to test the NS solver described in Chapter 5. The two-dimensional and three-dimensional dam break problems were solved first. The computed water height and pressure agreed reasonably well with the experimental data and published

numerical results. Then, the solver was applied to both the non-resonance and resonance liquid sloshing problems. In the non-resonance test, the numerical results were in good agreement with the analytical solutions and experimental data. In the resonance test, our numerical results performed better than the linear analytical solutions, which failed to predict the non-linear sloshing motion. Fairly good agreement between the numerical and experimental results was obtained. Finally, the solver was used to simulate water flooding into a damaged compartment of a Ro-Ro ferry. The accumulation of internal water predicted by our numerical method coincided with the experimental measurements. It was found that the engines obstructed the floodwater propagation inside the compartment significantly. These applications demonstrate that the developed solver is capable to predict complex free surface motion and analyze water impact forces on structures. Further application with our solver to study the interactive dynamic problem of a damaged ship and floodwater will be discussed in the following chapters.

Chapter 8

Damaged Ship Flooding in Calm Water

Having been successfully applied to strongly non-linear free surface flow problems (e.g., dam break, tank sloshing and compartment flooding), the two-phase flow NS solver is now used to study the interactive dynamics between a damaged ship and floodwater. The ship motion is considered by introducing the proposed dynamic mesh strategy. As benchmarking tests, two flooding scenarios of a damaged barge that is fixed or freely floats in calm water are simulated with our developed solver, respectively. The computed motions of internal water and the barge are compared with the experimental measurements. All computations are performed on a single-processor (Intel Core2, 3.0 GHz) personal computer.

8.1 Summary of Benchmarking Cases

Ruponen (2006) presented a series of model tests for the flooding phenomenon of a damaged box-shaped barge in calm water. The aim of these tests is to provide experimental data for the validation of numerical tools developed to tackle flooding problems. The main particulars of the barge model are provided in Table 8.1. The general arrangement of the barge and the internal layouts of its floodable compartments are shown in Figures 8.1 and 8.2, respectively. Table 8.2 lists the dimensions and working status of the damaged and internal openings. Compartment DB1 was constructed to be airtight. R21P and R21S were equipped with small pipes (ϕ 7 mm) for ventilation after the large openings (20 mm × 200 mm) on the

longitudinal bulkheads were submerged. The arrangement of ventilation pipe is shown in Figure 8.3. For the other compartments, the internal openings on the decks are large enough to provide sufficient level of ventilation. During the experiments, the compartments were equipped with water height sensors to measure the internal water levels. The locations of the sensors are shown in Figure 8.4. Six flooding cases were tested in the experiments. Case 03 has been numerically simulated by various participants of the ITTC benchmarking study (ITTC report, 2008), which shows that the codes based on simple hydraulic model can not reproduce the transient phenomenon of the flow. In the present study, cases 01 and 06 are selected as the validation tests of our proposed method.

Table 8.1: Main particulars of the barge model.

Length (L)	4.000 m
Breadth (B)	0.800 m
Draft (T)	0.500 m
Depth (D)	0.800 m
Centre of gravity above base (KG)	0.278 m
Displacement (Δ)	1447.39 kg
Moment of inertia along the x-axis (I_{xx})	176.0 kg·m^2
Moment of inertia along the y-axis (I_{yy})	2235.3 kg·m^2
Moment of inertia along the z-axis (I_{zz})	2209.4 kg·m^2

Table 8.2: Information of the damaged and internal openings.

Connecting	Dimension (mm)			Status	
	x	y	z	Case 01	Case 06
DB2 ↔ Outside	25	25	10	open	closed
DB1 ↔ DB2	10	ϕ20	ϕ20	open	closed
DB2 ↔ R21	60	40	10	open	closed
R21 ↔ R21P	20	10	200	open	open
R21 ↔ R21S	20	10	200	open	open
R21S ↔ Outside	60	10	40	closed	open
R21 ↔ R11	10	ϕ20	ϕ20	open	open
R21 ↔ R22	100	100	10	open	open
R11 ↔ R12	100	100	10	open	open
R12 ↔ R22	10	80	200	closed	closed

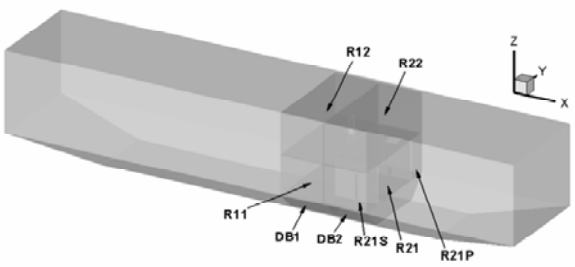

Figure 8.1: Sketch of the barge with eight floodable compartments.

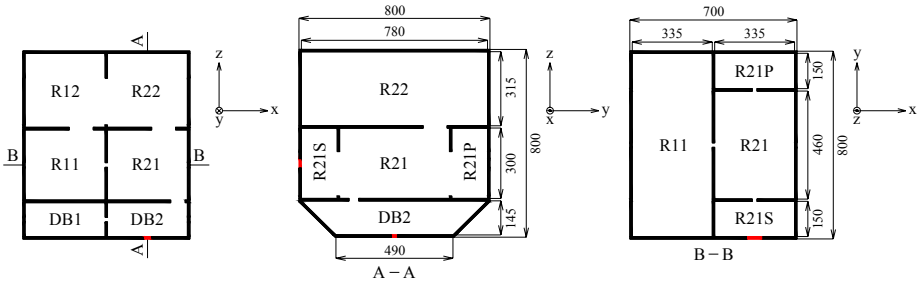

Figure 8.2: Internal layouts of the floodable compartments (units: mm).

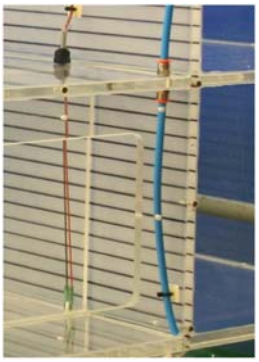

Figure 8.3: Ventilation pipe equipped in compartment R21S.

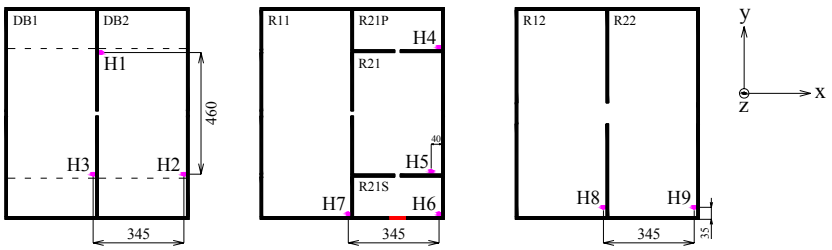

Figure 8.4: Locations of water height sensors placed in compartments (units: mm).

8.2 2-D Compartment Flooding Case

Before applying the developed NS solver to the aforementioned benchmarking cases, we first perform a time and grid dependence study in the context of the two-dimensional compartment flooding case, as shown in Figure 8.5. The adopted two-dimensional compartment is a simplified cross-section of the actual compartment of the barge described previously. Its floating position is fixed during the simulation. Once the simulation starts, the water will flood the compartment through the damaged opening until the internal water level equals the external one. On the left and right boundaries of the computational domain, the water level and pressure are set equal to the initial water height and hydrostatic pressure, respectively. The no-slip wall boundary condition is imposed on the other boundaries. The computational domain is divided into five blocks, as shown in Figure 8.6. Three meshes described in Table 8.3 are generated. In the possibly flooded area of Block 1 and 2, the uniform elements are arranged in both the *y*- and *z*-directions, the sizes of which are 0.014 m, 0.01 m and 0.007 m for the coarse, medium and fine grids, respectively. In Blocks 3, 4 and 5, the element size varies. In the *y*-direction, it becomes larger with an expansion factor of approximately 1.2 as the distance from the compartment increases. In the *z*-direction, more elements are distributed near the free surface and the damaged opening. Figure 8.7 shows the coarse grid arrangement.

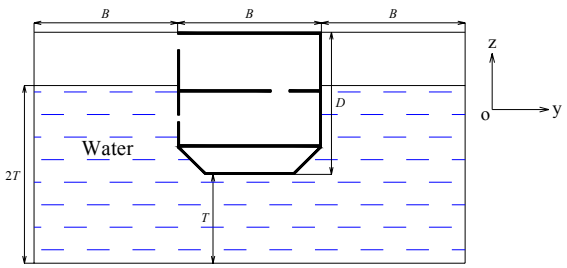

Figure 8.5: Sketch of the 2-D compartment flooding case.

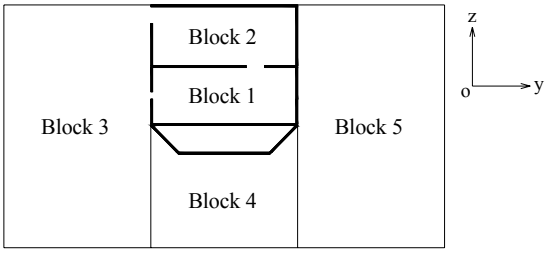

Figure 8.6: Block division of the computational domain for the 2-D compartment flooding case.

Table 8.3: Meshes employed in the 2-D compartment flooding case.

Grid	Number of elements arranged in the y- and z-directions					Total number of elements
	Block 1	Block 2	Block 3	Block 4	Block 5	
Coarse	55 × 21	55 × 14	16 × 45	24 × 8	10 × 41	3247
Medium	78 × 30	78 × 18	16 × 47	24 × 8	10 × 41	5098
Fine	111 × 42	111 × 22	16 × 50	24 × 8	10 × 41	8506

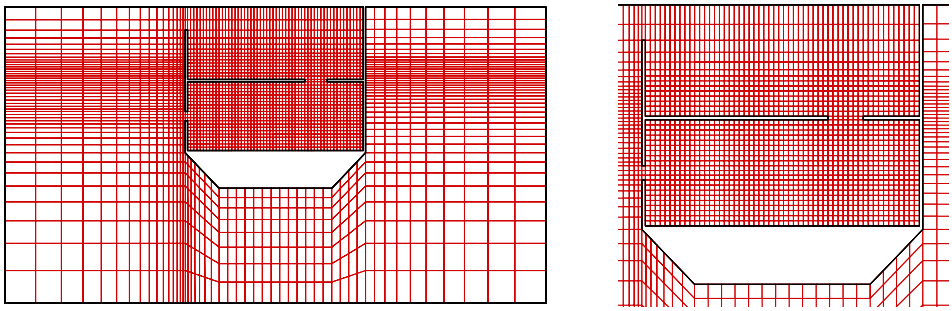

Figure 8.7: Sketch of the coarse grid arrangement for the 2-D compartment flooding case.

The time step used in the simulations is automatically adjusted according to Co_{lim} (see Eq. (5.15)). The value of Co_{lim} being around 0.25, as recommended by Ubbink (1997), may be too conservative for the current flooding cases. Thus the aim of the time dependence study is to investigate the influence of different Co_{lim} on the numerical solution for the flooding problem. Three different Co_{lim} values (0.75, 0.50, and 0.25) are investigated. The medium grid listed in Table 8.3 is employed. It takes 0.9, 1.2 and 2.1 CPU hours to complete a 10-s simulation with Co_{lim} equal to 0.75, 0.50 and 0.25, respectively. The comparisons of the computed interface profiles are shown in Figure 8.8. At the initial stage, the flooding flow evolves with a simple

interface, and the results computed with different Co_{lim} are nearly identical. After the floodwater reaches the opposite wall of the compartment and overturns, the flow becomes violent, and the differences between the results become obvious. However, the global motions of the floodwater predicted with the three Co_{lim} are still in good agreement. Figures 8.9 and 8.10 show the impact forces of the floodwater on the compartment. For the horizontal force, the results computed with Co_{lim}=0.75 differ largely from those computed with smaller Co_{lim}, whereas the results computed with Co_{lim}=0.50 are consistent with those computed with Co_{lim}=0.25. For the vertical force, the results computed with the three Co_{lim} values are in good agreement. The above comparisons demonstrate that Co_{lim} values equal to 0.50 can ensure acceptable numerical accuracy while consuming relatively fewer computational resources. In the remainder of present chapter, the limit of the cell Courant number will be 0.50 for all computations.

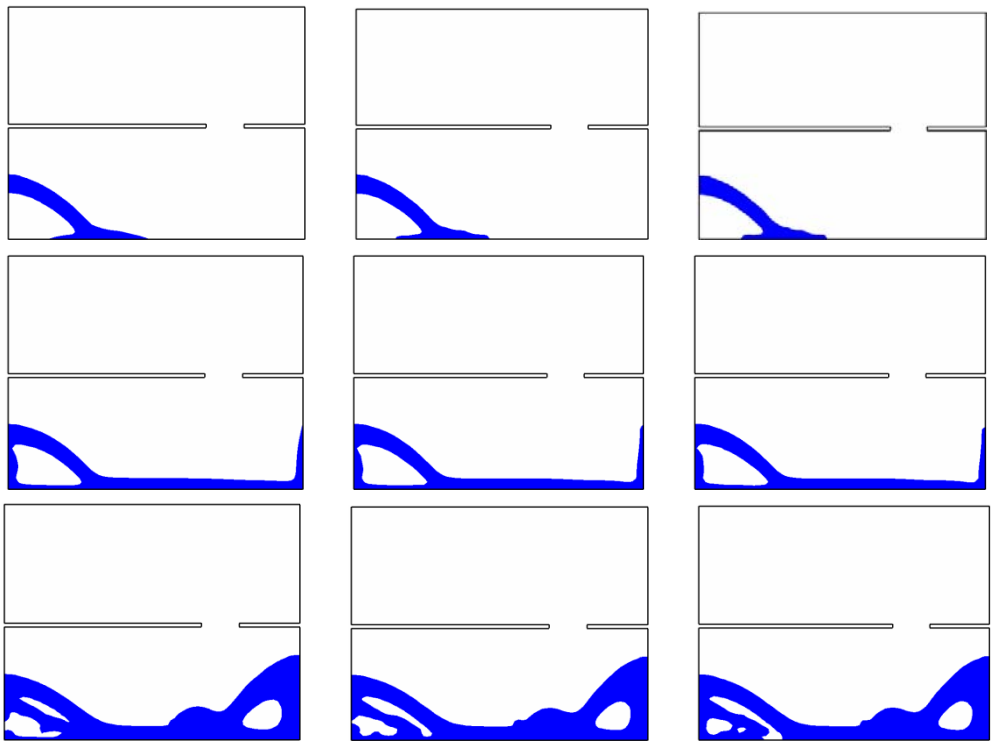

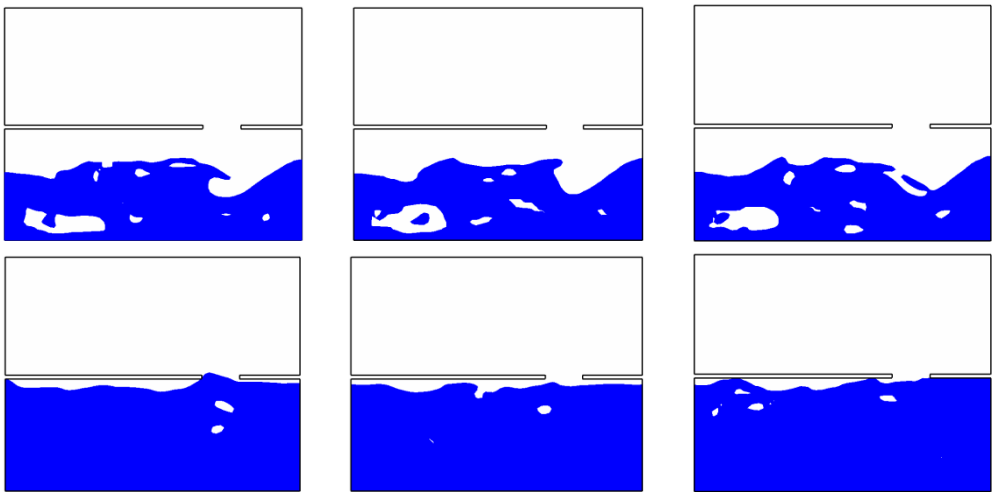

Figure 8.8: Snapshots of the 2-D flooding process (t=1, 2, 4 s) computed with different Co_{lim} values (Left: Co_{lim}=0.75, middle: Co_{lim}=0.50, right: Co_{lim}=0.25).

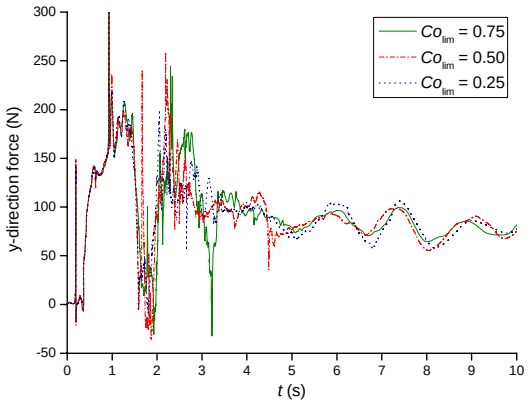

Figure 8.9: Comparison of the time history for the y-direction force computed with different Co_{lim} values.

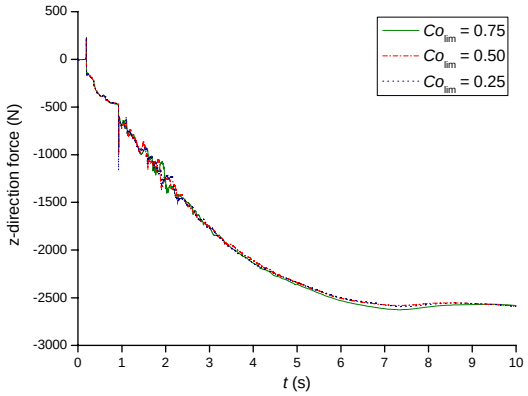

Figure 8.10: Comparison of the time history for the z-direction force computed with different Co_{lim} values.

The floodwater motion inside the compartment is a crucial part of flooding. The accuracy of its prediction largely depends on the number of grid elements used in the compartment region. Therefore, the aim of the grid dependence study is to investigate the grid resolution in Blocks 1 and 2, as shown in Figure 8.6. The three meshes listed in Table 8.3 are investigated. It takes 0.6, 1.2 and 2.2 CPU hours to complete a 10-s simulation on coarse, medium and fine grids, respectively. Figure 8.11 shows the comparisons of the computed interface profiles. The results computed with different grid resolutions are similar at the initial stage. The discrepancies between the results become large after the flow becomes chaotic. The interface profiles obtained on the coarse grid are seriously smeared due to excessive numerical diffusion. With an increase in the grid resolution of the compartment region, more details of the interface profile can be retained. Figures 8.12 and 8.13 show the impact forces of floodwater on the compartment. For the horizontal force, the results computed with the coarse grid deviate significantly from those computed with the finer grids, whereas the results obtained on the two finer grids coincide reasonably well. For the vertical force, good agreement among the numerical results is obtained. The above investigation indicates that the coarse grid introduces unacceptable level of numerical diffusion and cannot be employed for the rest of the test cases. Compared to the fine grid, the use of the medium grid can reduce the computational cost notably and still achieve tolerable numerical accuracy. Thus, the mesh generation for the subsequent 3-D flooding cases is based on the arrangement of a medium grid.

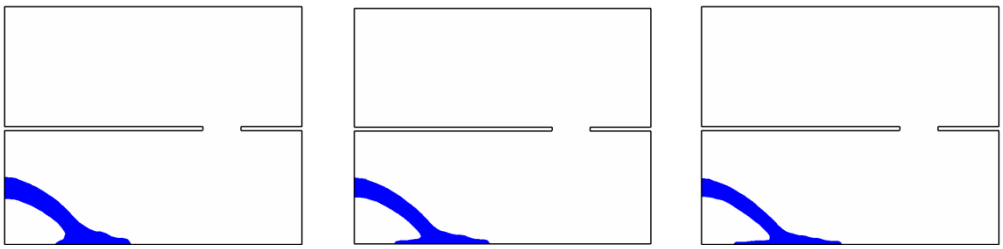

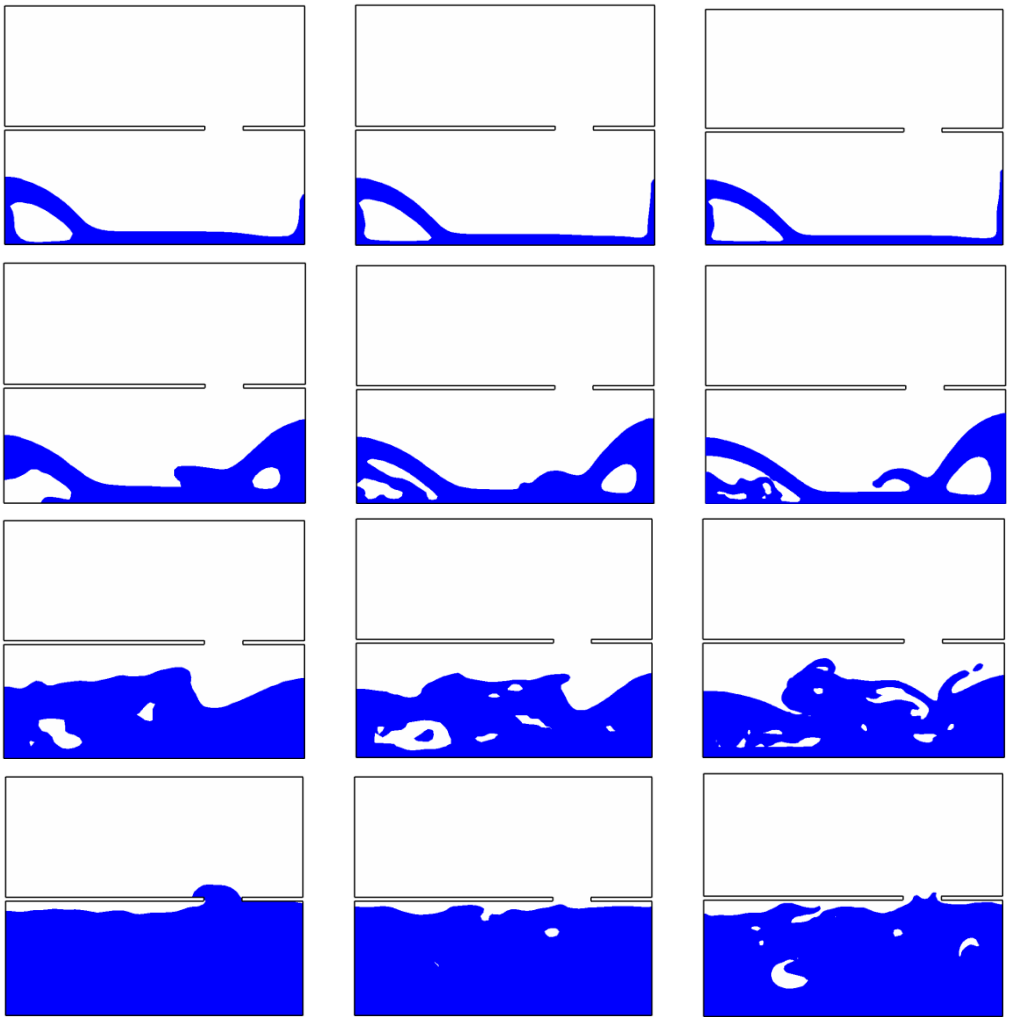

Figure 8.11: Snapshots of the 2-D flooding process (t=0.25, 0.5, 1, 2, 4 s) computed with different meshes (Left: coarse grid, middle: medium grid, right: fine grid).

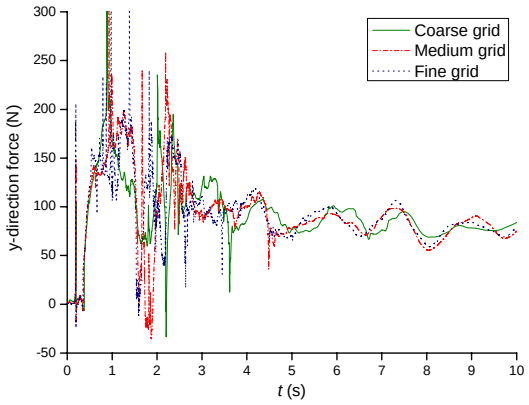

Figure 8.12: Comparison of the time history for y-direction force computed with different meshes.

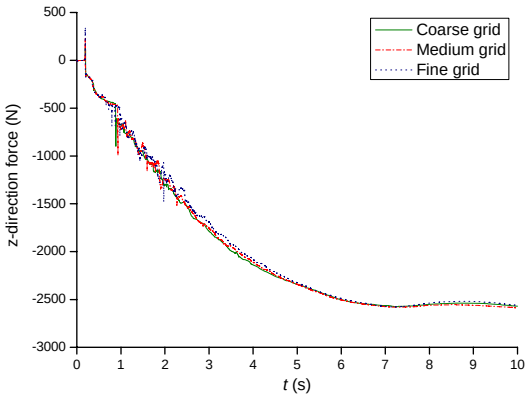

Figure 8.13: Comparison of the time history for *z*-direction force computed with different meshes.

8.3 Fixed Barge Flooding Case

The present NS solver could then be applied to simulate the flooding of a damaged barge illustrated in Section 8.1. Test case 01 reported by Ruponen (2006) is used as a benchmarking study. A damaged, rectangular opening (25 mm × 25 mm) located at the bottom of compartment DB2 is tested. The floating position of the barge is fixed during the test. The model test shows that the airtight compartment DB1 is flooded very slow and finally filled half due to the blockage effect of the internal air. However, at the time of the present study, the air compressibility was not considered in our method. Thus, the small internal opening (ϕ 20 mm) that connects DB1 to DB2 is closed, and DB1 is not flooded in the numerical simulation. The experimental results in Figure 8.14 show that the rise of water level in DB1 is nearly 7 times slower than that in DB2. This comparison indicates that the close of internal opening connecting DB1 to DB2 has insignificant effect on the entire flooding process. On the other hand, two ventilation holes (20 mm × 10 mm) are opened on the tops of the longitudinal bulkheads, as shown in Figure 8.15, to ensure that the air in R21P and R21S can escape during the computation.

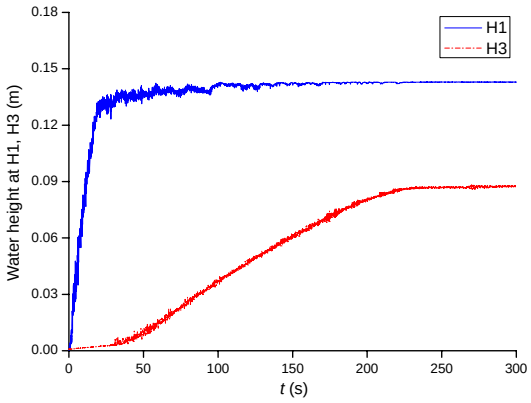

Figure 8.14: Comparison of the time history of the water height in DB1 and DB2 for the fixed barge flooding case.

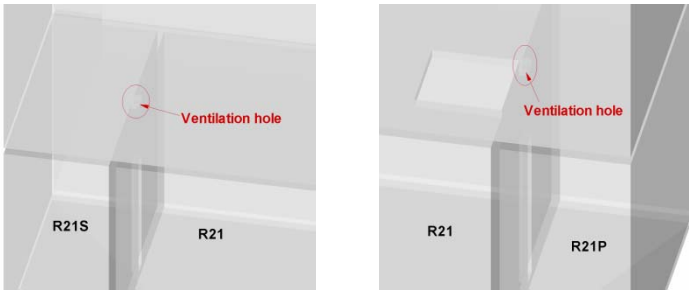

Figure 8.15: Ventilation holes on the longitudinal bulkheads.

Figure 8.16 shows the numerical tank used for the simulation; the tank is 2*L* in length, *L*+*B* in breadth and *T*+*D* in height (1*T* under the barge bottom). On the left, right, front and back boundaries of the tank, the water level is set to the initial water height, and the hydrostatic pressure is imposed on these boundaries. On the top boundaries of compartments R12 and R22 and the tank, the pressure is set to be the atmospheric pressure. The no-slip wall boundary condition is imposed on the other boundaries. The mesh generation for this test case refers to the previous grid dependence study. In the possibly flooded areas of the compartments, the element size magnitudes in the *x*-, *y*- and *z*-directions are 0.01 m, as shown in Figure 8.17. In the *x*- and *y*-directions outside the compartments, the element sizes vary and become larger away from the damaged opening with an expansion factor of approximately 1.2. In the *z*-direction, the element size is 0.01 m in the free surface area and expands away from it. Figure 8.18 shows the outline of mesh arrangement in the computational

domain. The total number of elements is 406,140, and its distribution in the computational domain is given in Table 8.4.

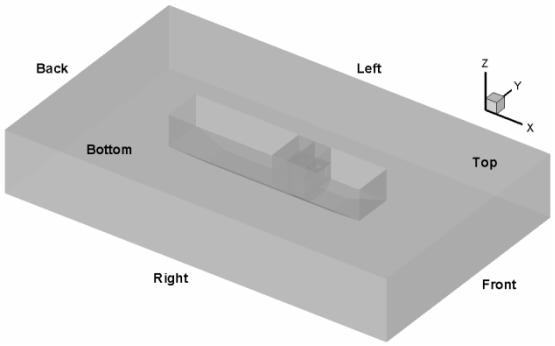

Figure 8.16: Sketch of the computational domain for the fixed barge flooding case.

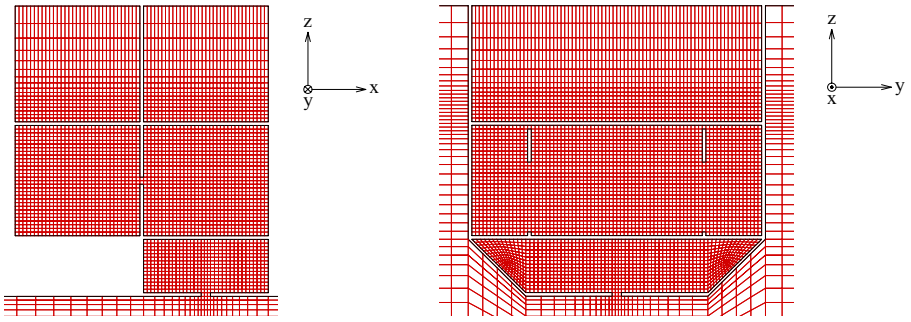

Figure 8.17: Sketch of the mesh arranged in the floodable compartments for the fixed barge flooding case.

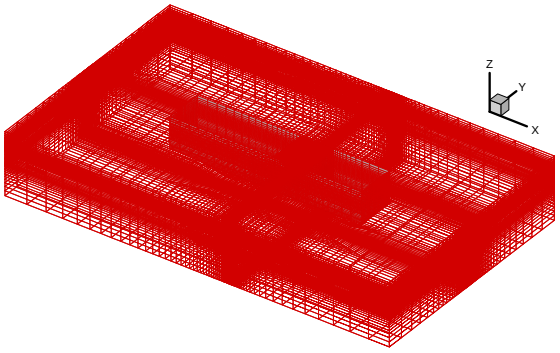

Figure 8.18: Sketch of the mesh arrangement in the computational domain for the fixed barge flooding case.

Table 8.4: Number of elements distributed in the computational domain for the fixed barge flooding case.

Inside the compartment							Outside the compartment
R11	R12	DB2	R21	R21P	R21S	R22	
77,420	43,758	36,607	47,200	15,300	15,300	45,084	125,471

The numerical simulation runs for up to 500 s and uses 467 CPU hours in this computation. Figure 8.19 shows the computed floodwater motion inside the compartments. At the initial stage of flooding, the external water floods into DB2 through the damaged opening like a water jet and splashes to the top of the compartment. After DB2 is filled, the floodwater flows to the other compartments smoothly through the internal openings, and the water levels rise gradually. The entire flooding process appears to occur almost symmetrically about the barge's longitudinal central plane.

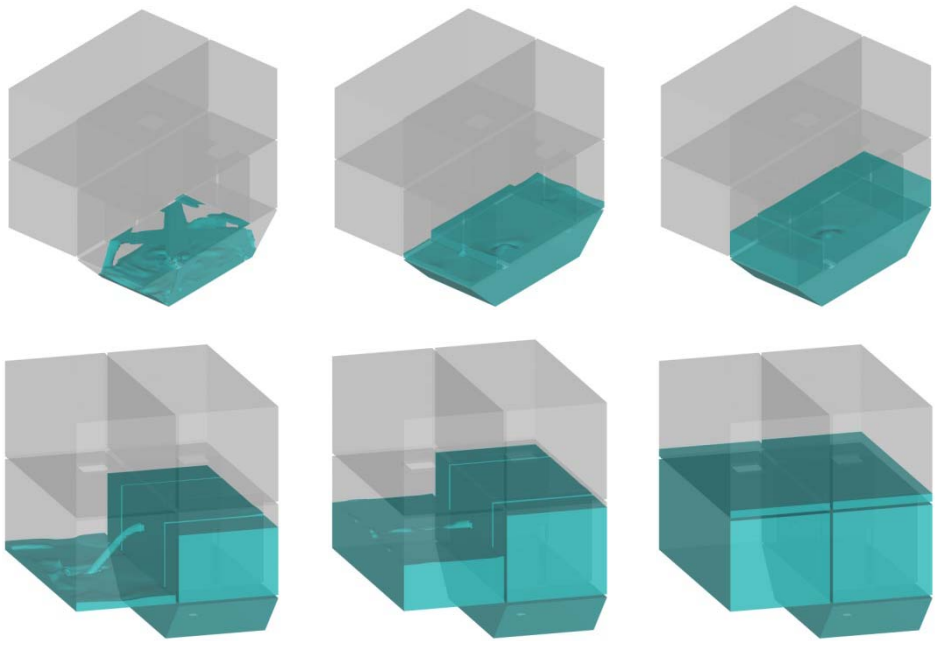

Figure 8.19: Snapshots of the internal water motion during the fixed barge flooding process (t=5, 25, 50, 100, 200, 400 s).

The comparisons of water heights obtained by the numerical and experimental methods are shown in Figures 8.20 through 8.27. In DB2, the computed results

compare well with the experimental data during the first 15 s, after which the water level predicted by the present method rises more slowly than that measured by the experiment. In R21, R21P and R21S, the computed water heights are under-predicted; however, the change trends of the results with respect to the time obtained by the two methods are in good agreement. When the free surface suffers from large-scale deformation, such as the complex free surface motion occurring in DB2, the CICSAM scheme introduces moderate numerical diffusion that leads to the floodwater spreading more rapidly in the calculation. Therefore, R21, R21P and R21S are flooded earlier, whereas DB2 is filled later in the numerical simulation. Although the filled time of R21, R21P and R21S in the computation disagrees with that in the experiment, these three compartments are filled synchronously in the computation and experiment, respectively, as shown in Figure 8.24. This observation indicates that air compression in R21P and R21S does not occur because the air can sufficiently escape through the ventilation pipes (in the model test) or holes (in the numerical simulation) during the current slow flooding. In R11, the computed water height agrees well with the experimental one. Since the internal opening connecting R21 and R11 is small, the water ingress into R11 is slow and the motion of internal water is smooth. The comparisons in R12 and R22 show that the floodwater reaches the water height sensors earlier in the numerical simulation, which is also attributed to numerical diffusion. As the water levels rise at the later stage, the discrepancies between the numerical and experimental results become small. In all of the comparisons, the errors in the water heights between the calculation and the experiment are approximately 0.01 m, which is equal to the size of the mesh elements. Thus, the numerical results obtained on the current grid resolution are satisfactory for this test case.

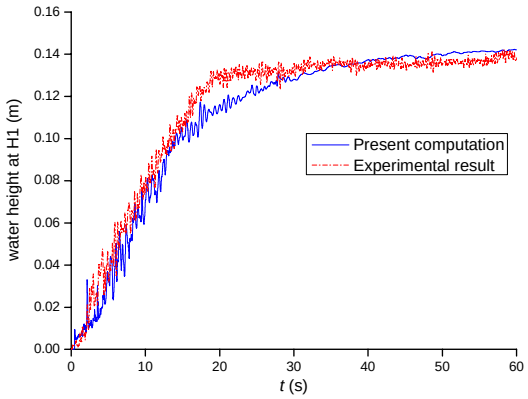

Figure 8.20: Comparison of the time history of the water height in DB2 for the fixed barge flooding case.

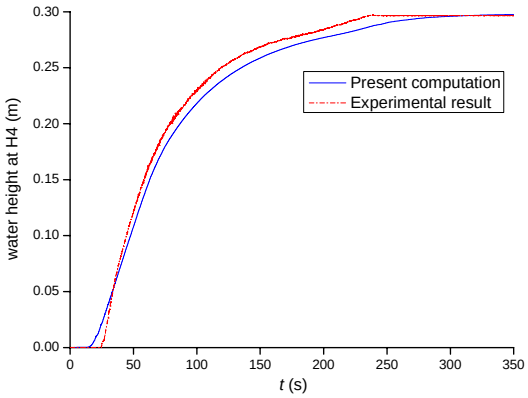

Figure 8.21: Comparison of the time history of the water height in R21P for the fixed barge flooding case.

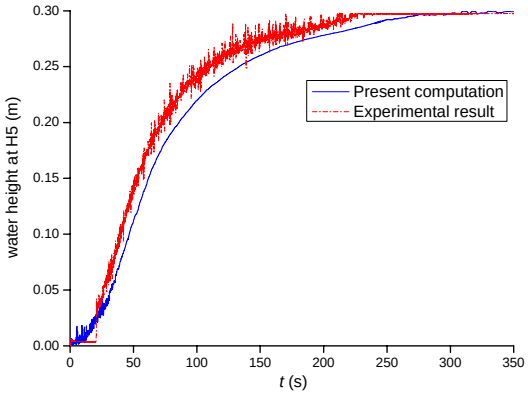

Figure 8.22: Comparison of the time history of the water height in R21 for the fixed barge flooding case.

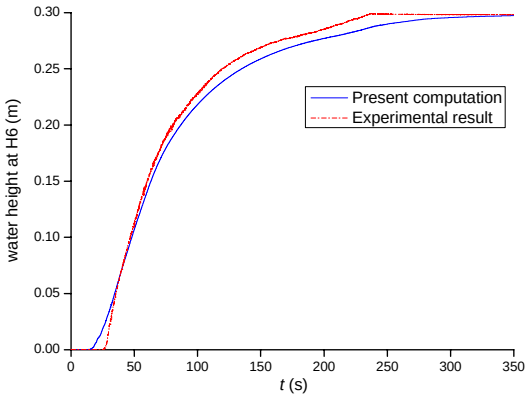

Figure 8.23: Comparison of the time history of the water height in R21S for the fixed barge flooding case.

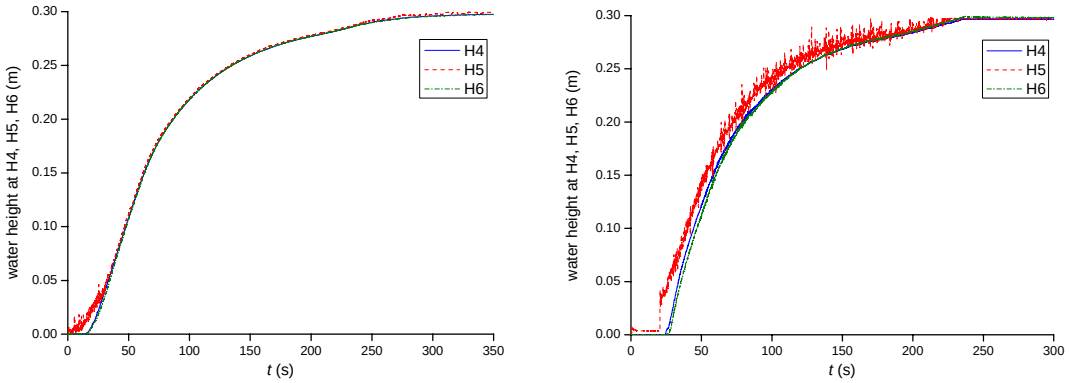

Figure 8.24: Comparison of the time history of water heights in R21P, R21 and R21S for the fixed barge flooding case (Left: present computation, right: model test).

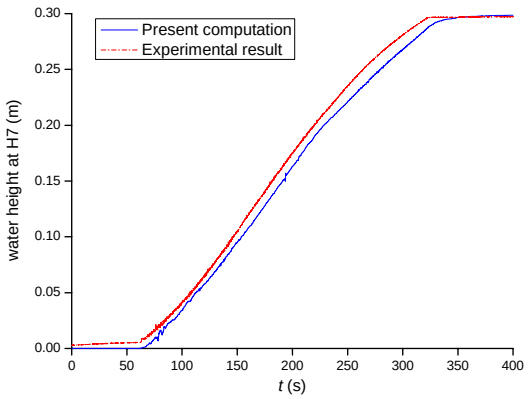

Figure 8.25: Comparison of the time history of the water height in R11 for the fixed barge flooding case.

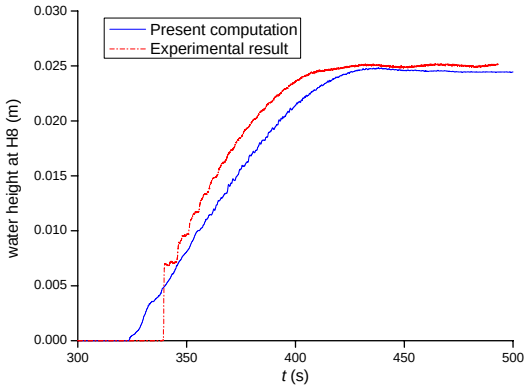

Figure 8.26: Comparison of the time history of the water height in R12 for the fixed barge flooding case.

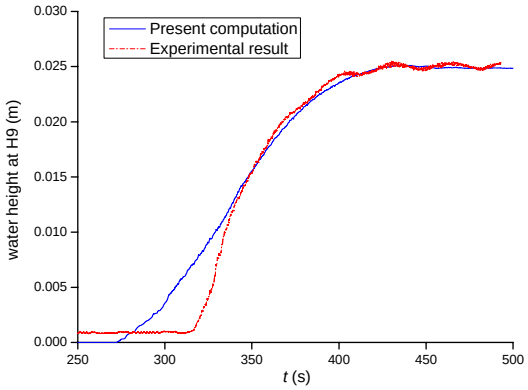

Figure 8.27: Comparison of the time history of the water height in R22 for the fixed barge flooding case.

8.4 Floating Barge Flooding Case

The last numerical simulation shown in this chapter focuses on the flooding of a moving ship. Test case 06 reported by Ruponen (2006) is used to validate the present method. A damaged, rectangular opening (60 mm × 40 mm) located on the side of compartment R21S is tested. The barge floats freely in calm water during the experiment. In the numerical simulation, only the heave, pitch and roll motions of the barge are considered, whereas the other motions (surge, sway and yaw) are not included because they are relatively slow and have little effect on the flooding process in calm water.

To avoid the effect of boundary reflection on the flow around the hull, a numerical tank larger than the one adopted in the previous fixed barge case is used in this simulation. Its dimensions are 3L in length, 2L+B in breadth and 3T+D in height (2T under the barge bottom). The definitions of boundary condition are similar to those in the fixed barge case. According to the dynamic mesh strategy depicted in Section 5.2.3, the computational domain is divided into three regions, as shown in Figure 8.28. Region 1 includes six floodable compartments (R11, R12, R21, R21P, R21S and R22) and the adjacent area of the hull. The mesh in this region moves in the same motion of the barge. In region 2, the mesh is updated by the OST spring analogy method. The mesh in region 3 is kept static during the simulation. The mesh arrangements in the compartment areas are similar to those in the fixed barge case. On the hull surface, the size of the elements distributed near the free surface and the damaged opening is 0.01 m, as shown in Figure 8.29. In regions 2 and 3, the element sizes vary and become larger away from the hull with an expansion factor of approximately 1.2. The total number of elements employed in the computational domain is 755,155, the distribution of which is summarised in Table 8.5.

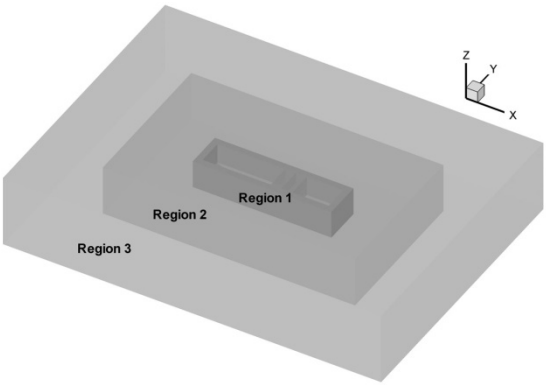

Figure 8.28: Sketch of the computational domain for the floating barge flooding case.

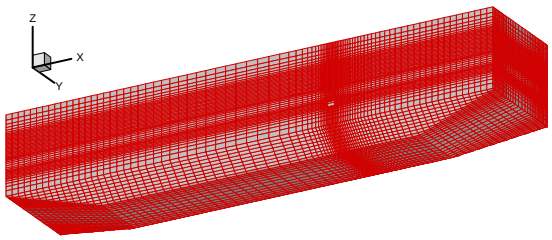

Figure 8.29: Mesh arrangement on the hull surface for the floating barge flooding case.

Table 8.5: Number of elements distributed in the computational domain for the floating barge flooding case.

Region 1							Region 2	Region 3
R11	R12	R21	R21P	R21S	R22	Adjacent area		
77,320	56,628	47,104	15,324	15,300	58,392	85,905	258,855	140,327

The numerical simulation runs for up to 400 s and uses 1157 CPU hours in this computation. Figure 8.30 compares the internal water motion obtained by the present method and the model test during the initial flooding stage. Generally, the computed floodwater behaviours are consistent with the experimental results. In the first several seconds, the flooding process appears to be clearly asymmetrical about the longitudinal central plane. The external water floods into the compartments drastically through the damaged opening and accumulates promptly. As the damaged opening is collinear with the internal opening connecting R21S to R21, the external water sprays straight into R21. It should be noted that the distance of water spraying in the experiment is farther than that in the numerical simulation. This observation indicates that in the experiment more water directly enters into R21 and less stays in R21S; whereas in the numerical simulation opposite case is deduced. Consequently, the computed water levels in R21, R21P and R21S disagree with the experimental measurements during the first several seconds, as shown in Figure 8.34. Due to the large internal openings, the floodwater flows across R21, R21P and R21S without significant blockage and spreads throughout the compartments rapidly. The water levels in these three compartments rise to be close soon. After the large internal

openings on the longitudinal bulkheads are submerged, in the model test the water level in R21 is a bit higher than those in R21P and R21S; whereas in the numerical simulation the water levels in these three compartments still keep equivalent. Such disagreement between computation and experiment will be discussed later. After 20 s, the flooding process seems to be nearly symmetrical.

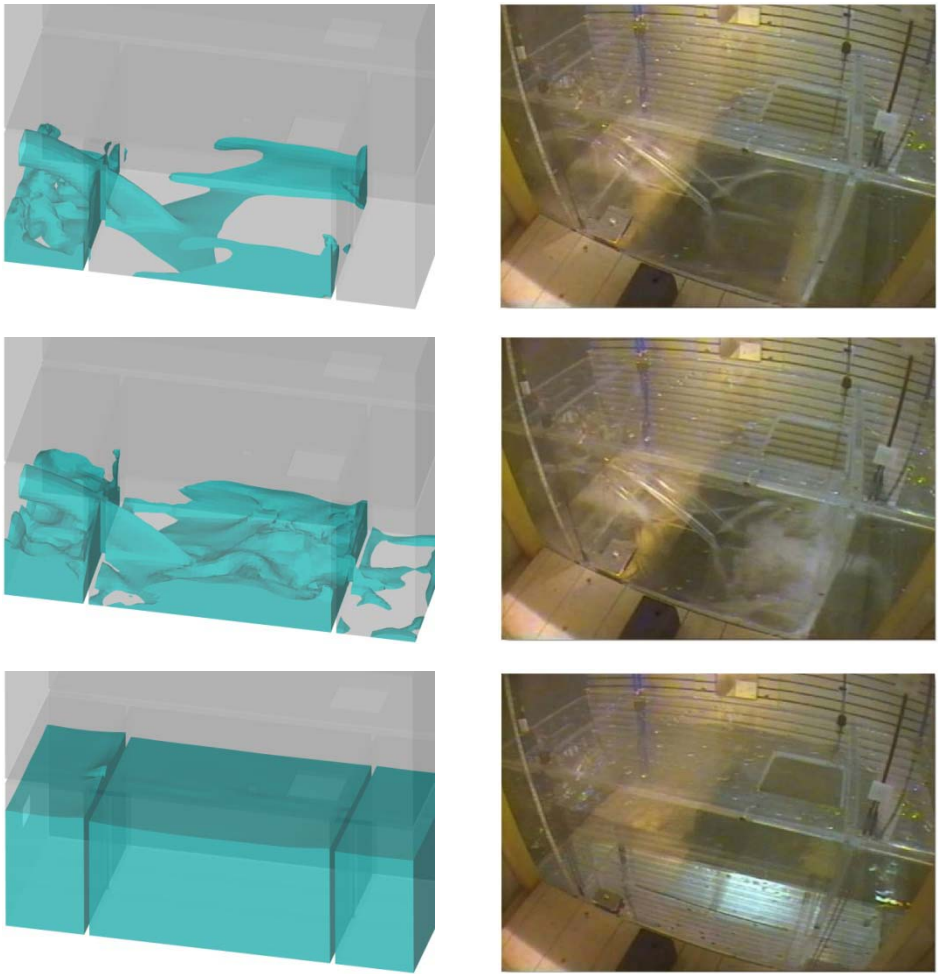

Figure 8.30: Snapshots of the internal water motion during the floating barge flooding process (t=0.7, 2.25, 20 s) (Left: present computation, right: model test).

Comparisons of water height obtained by the numerical and experimental methods are shown in Figures 8.31 through 8.37. The rapid rise of water level in R21, R21P and R21S demonstrates that the flooding is drastic at the initial stage. Before the large internal openings on the longitudinal bulkheads are submerged (t<15 s), there

is no significant difference between the water levels in these three compartments in the experiment, but in the computation the water level in R21S rises much faster than those in R21 and R21P. The reason for such discrepancy between computation and experiment has been stated previously. After the large internal openings on the longitudinal bulkheads are submerged (t>15 s), difference between numerical simulation and experiment in terms of ventilation effect on the flooding process is observed in Figure 8.34. In the experiment, the ventilation pipes (ϕ 7 mm) equipped in R21P and R21S are too small to sufficiently vent the air for such drastic flooding. The decreased level of ventilation leads to the fact that R21P and R21S are filled approximately 8 s later than the fill of R21. In the numerical simulation, the holes (20 mm × 10 mm) opened on the longitudinal bulkheads (see Figure 8.15) are still capable to sufficiently vent the air inside R21P and R21S, and hence these three compartments are filled synchronously at around 28 s. The above comparisons indicate that in the case of insufficient level of ventilation the entrapped air has blockage effect on water ingress. To account for this effect, the present numerical method needs to be extended to include the model of air compression in future. As the opening connecting R21 to R11 is small, the flooding progression in R11 is smooth. The water level in R11 rises slowly and is well predicted by the present method in comparison with the experimental results. After the water levels rise to the top of the lower compartments, the floodwater flows into the upper compartments through the openings on the decks. Good agreement between the computed and measured water heights in R22 is shown. The water level rises rapidly in the first 50 s and slows down as the difference between the internal and external water levels gradually decreases. Compared to the experiment, R12 is flooded earlier in the numerical simulation. The disagreement between the numerical and experimental results becomes small during the final flooding stage. The flooding process comes to an end after 350 s, when the water level inside the compartments is equal to that outside the barge.

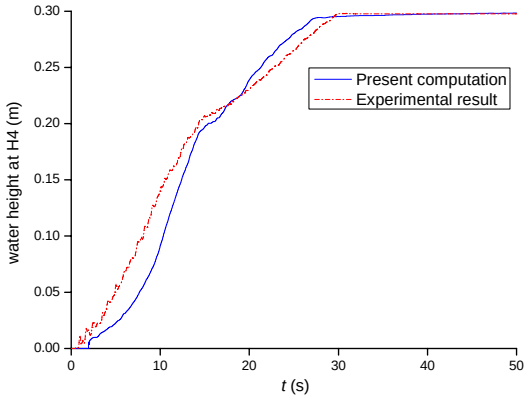

Figure 8.31: Comparison of the time history of the water height in R21P for the floating barge flooding case.

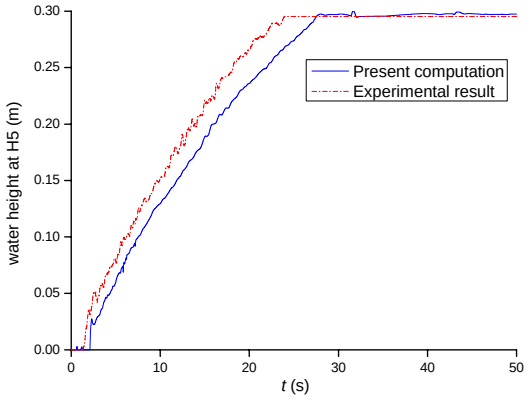

Figure 8.32: Comparison of the time history of the water height in R21 for the floating barge flooding case.

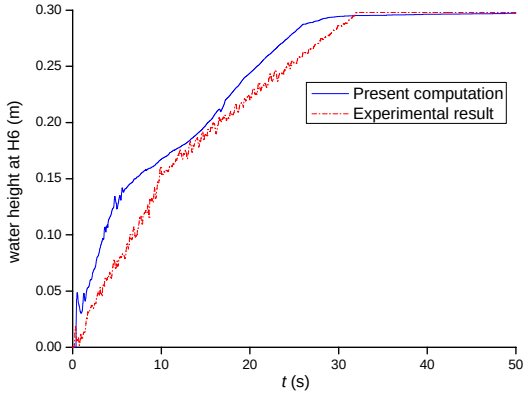

Figure 8.33: Comparison of the time history of the water height in R21S for the floating barge flooding case.

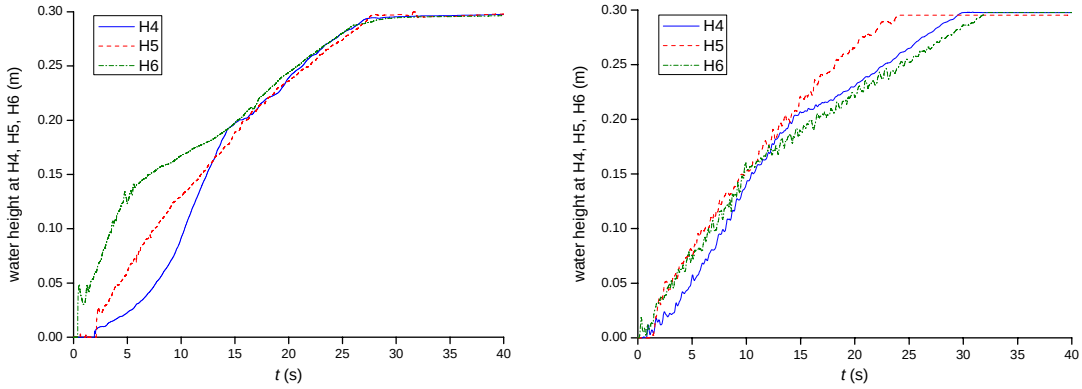

Figure 8.34: Comparison of the time history of water heights in R21P, R21 and R21S for the floating barge flooding case (Left: present computation, right: model test).

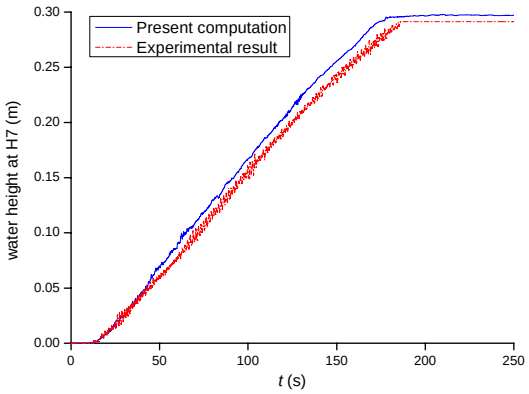

Figure 8.35: Comparison of the time history of the water height in R11 for the floating barge flooding case.

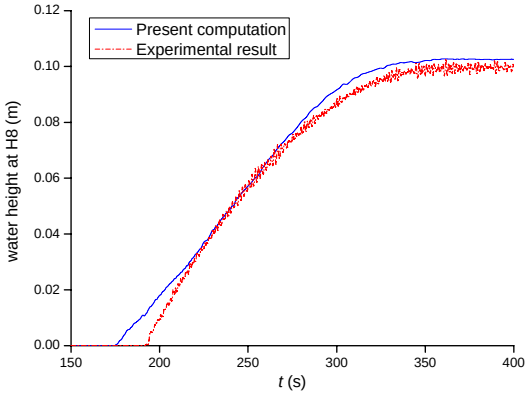

Figure 8.36: Comparison of the time history of the water height in R12 for the floating barge flooding case.

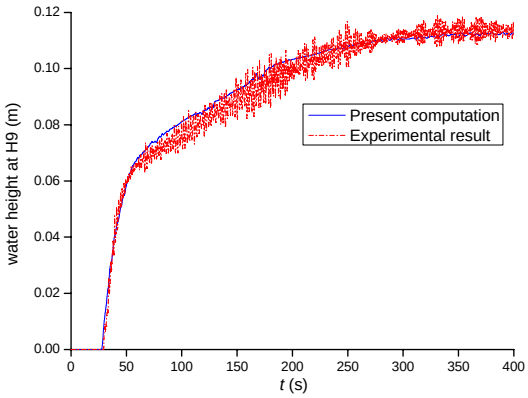

Figure 8.37: Comparison of the time history of the water height in R22 for the floating barge flooding case.

Comparisons of the computed and measured motions of the barge are shown in Figures 8.38 through 8.40. The barge sinks rapidly during the initial stage because of the drastic water ingress. As R21, R21P and R21S are filled, the ingress of water starts to abate, and the sinking of the barge tends to be slower. The computed heave motion is in good agreement with its experimental counterpart. Similar behaviour for the pitch motion is observed, and fairly good agreement between the numerical and experimental results is obtained. Although the flooding process is clearly asymmetrical about the longitudinal central plane in the first several seconds, the barge only heels with a small angle due to its high initial stability. At the later stage, the flooding process tends to be symmetrical, and the heel angle approaches zero.

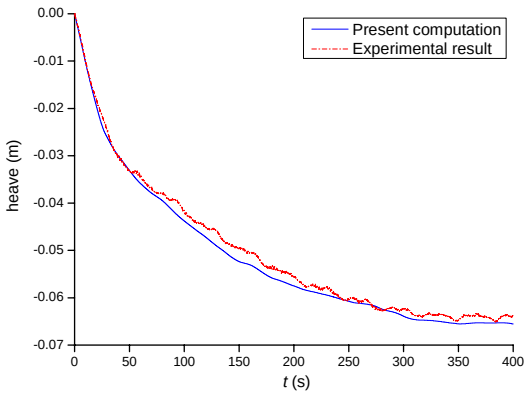

Figure 8.38: Comparison of the time history of the heave motion for the floating barge flooding case.

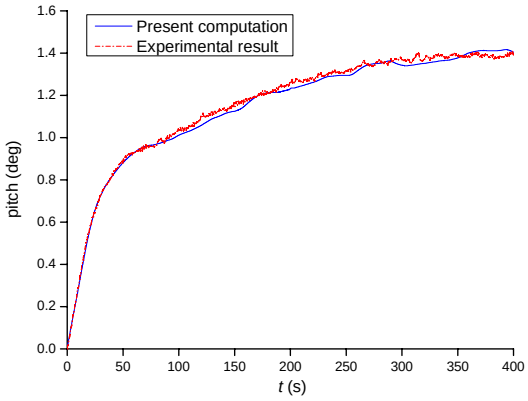

Figure 8.39: Comparison of the time history of the pitch motion for the floating barge flooding case.

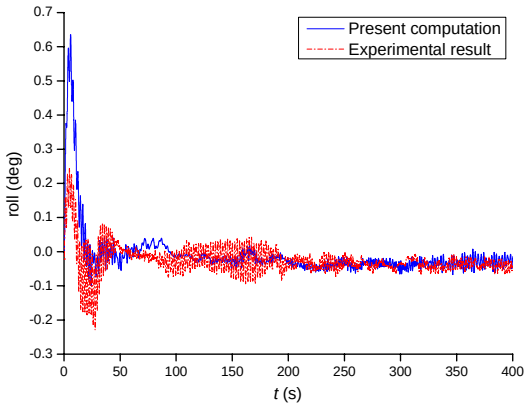

Figure 8.40: Comparison of the time history of the roll motion for the floating barge flooding case.

8.5 Closure

The present NS solver combining the VOF model and dynamic mesh techniques has been applied to simulate the flooding of a damaged ship. The performed benchmarking study demonstrates that the present method is effective in predicting the coupled dynamics of a damaged ship and floodwater. For the case of fixed barge flooding, the flooding process was drastic during the initial stage. The floodwater inside the compartments exhibited strongly non-linear and transient behaviour such as ejecting, overturning and breaking. During later stage, the flooding progressed slowly and steadily. The internal water showed quasi-static behaviour. For the case of

floating barge flooding, the flooding process was also drastic during the initial stage, and the barge was forced to sink and pitch rapidly. However, the notable transient dynamics of internal water had a limited effect on the roll motion of the barge due to its high initial stability. Furthermore, air compressibility had considerable effect on the flooding process due to insufficient level of ventilation. In the intermediate and final stages, the flooding flow moved smoothly with a flat interface, and the barge became quasi-static.

Although the ability of developed NS solver to tackle the intricate flooding problem has been confirmed, the expensive computational time prohibits its practical applications. The hybrid method that couples the present NS solver and a seakeeping solver can overcome this hurdle. Its application to damaged ship flooding in waves will be presented in the next chapter.

Chapter 9

Damaged Ship Flooding in Waves

The hybrid method introduced in Chapter 6 is now applied to solve the flooding problem of a damaged ship in waves. A Ro-Ro ferry is selected as the test ship. Numerical simulations of roll decay of the ship in intact and damaged conditions are first conducted. Then the behaviour of the intact and damaged ship in beam seas is investigated. The validation of numerical results and analysis of the coupled dynamics of ship, wave and floodwater are given. Moreover, a numerical test is carried out to investigate the influence of water ingress/egress on the behaviours of damaged ship and internal water. All computations are performed on a dual-core (Intel Core2, 3.0 GHz) personal computer.

9.1 Description of Test Ship

A Ro-Ro ferry, coded as PRR1 in the literatures (ITTC report, 2002; Papanikolaou and Spanos, 2004; ITTC report, 2005), is adopted herein as the test ship in our study. Its behaviours in intact and damaged conditions have been experimentally tested in the Denny Tank of Strathclyde University (Jasionowski, 2001). Table 9.1 gives the main particulars of the ship. Its body plan is shown in Figure 9.1. The damaged opening is located on the port side of the midship. Figure 9.2 illustrates the general arrangement of the ship, in which the parts in shadow denote the floodable compartments including the double bottoms, storage rooms and car deck. It is shown that the compartment's internal layout is asymmetric.

Table 9.1: Main particulars of PRR1.

Length between perpendiculars (L_{pp})	170.00 m
Breadth (B)	27.80 m
Draft (T)	6.25 m
Depth to car deck (D_{cd})	9.00 m
Damaged length (L_{dam})	8.10 m
Centre of gravity above base (KG)	12.892 m
Displacement (Δ)	17301.7 t
Moment of inertia along the x-axis (I_{xx})	1441.9 kt·m^2
Moment of inertia along the y-axis (I_{yy})	30946.3 kt·m^2
Moment of inertia along the z-axis (I_{zz})	30946.3 kt·m^2

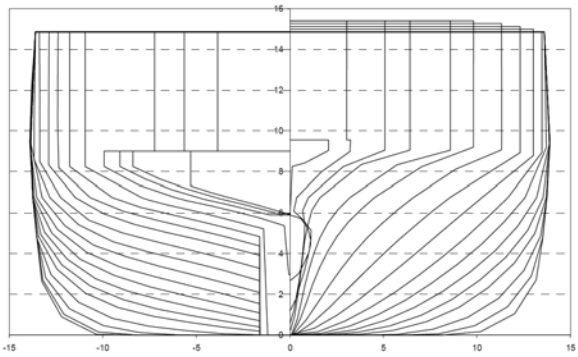

Figure 9.1: Body plan of PRR1 (from Papanikolaou and Spanos (2004)).

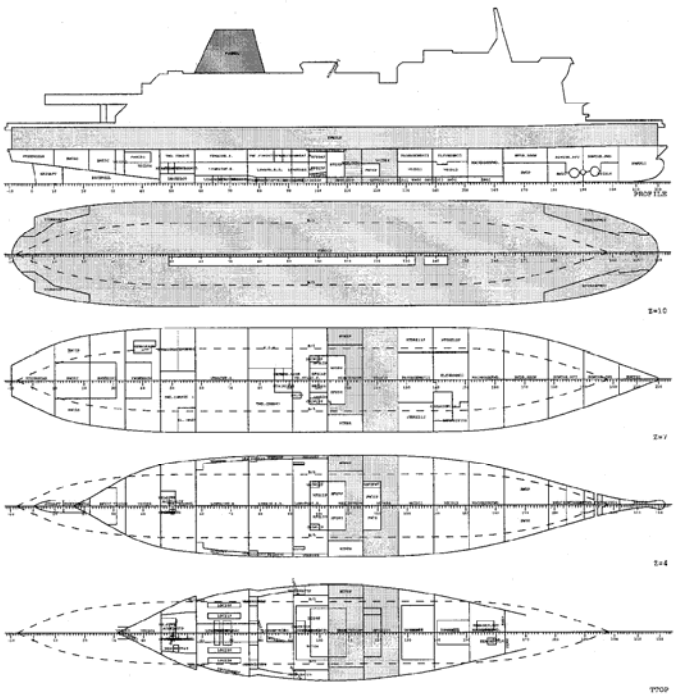

Figure 9.2: General arrangement of PRR1 (from ITTC report (2002)).

9.2 Roll Decay Test

9.2.1 Case for Intact Ship

The roll decay of PRR1 in intact condition is first simulated using the seakeeping solver PROTEUS3. Note that only 4-DOF of the ship (sway, heave, roll and pitch) is considered in the numerical simulations presented in this chapter. The ferry, without forward speed, is initially heeled to 7° on the port side. The comparison of numerical and experimental results is shown in Figure 9.3. The natural frequencies of roll motion obtained with the computation and experiment are consistent, both of which are approximately 0.483 rad/s. On the other hands, good agreement of computed and measured roll amplitude decaying with the time indicates that the hydrodynamics due to viscous effects and ship radiation motion are effectively treated in PROTEUS3 for the test ship.

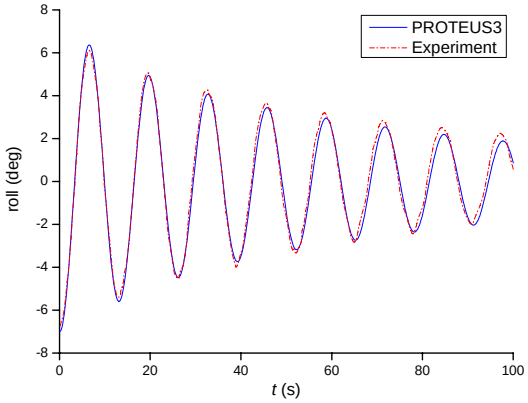

Figure 9.3: Comparison of the roll decay history of PRR1 in intact condition.

9.2.2 Case for Damaged Ship

The hybrid method (CFD + PROTEUS3) is applied to simulate the roll decay of PRR1 in damaged condition. Figure 9.4 shows the computational domain for the CFD simulation. On the top boundary, the pressure is set to be the atmospheric

pressure. The hydrostatic pressure corresponding to the initial water height is imposed on the bottom boundary. On the left, right, front and back boundaries, the initial water height and hydrostatic pressure are imposed. The no-slip wall condition is imposed on the surfaces of hull and compartments. A 1:40 scale model of PRR1 was used in the experiment, so the cross-section dimensions of the floodable compartments in model scale are close to those of the tank investigated in Section 7.2. Referring to the grid dependence study of the tank sloshing, two meshes listed in Table 9.2 are generated for the present case. In the floodable compartments, grid elements are uniformly arranged in the *x*-, *y*- and *z*-directions. Note that the sizes of 0.4 m and 0.283 m in actual scale correspond to the sizes of 0.01 m and 0.007 m in model scale, respectively. The computed results on the coarse grid show that the water can not reach the car deck. Therefore, the mesh in the car deck compartment is not generated for the fine grid. Because the hydrostatic pressure is imposed on the side boundaries, the reflection of ship-motion-induced wave (radiation wave) occurs at these non-physical boundaries and subsequently affects the flow field around the hull. To reduce the effect of wave reflection on the numerical accuracy, the radiation wave must be dissipated by introducing moderate numerical damping before it reaches the non-physical boundaries. For this purpose, the mesh arranged outside the compartment is gradually coarsened away from the damaged opening with a coarsened factor of approximately 1.1. The time steps for the computations on the coarse and fine grids are 0.02 s and 0.01 s, respectively, to ensure that the cell Courant number is within the limit of 0.5 (referring to Section 8.2). In the experiment, the ferry was initially heeled to 1.8° and rolled around the equilibrium angle of −3.2°. Its lower compartments were partially filled with water, the level of which is equal to the external water. In the numerical simulation, the initial and equilibrium roll angles are 1.8° and −3.25°, respectively. The draft of the ferry in damaged condition is 7.02 m. The numerical simulation runs up to 100 s, which spends 42 and 85 CPU hours on the computation with coarse and fine grids, respectively.

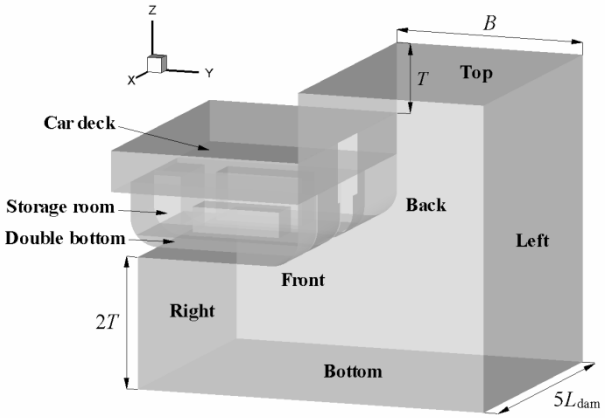

Figure 9.4: CFD simulation domain for the case of PRR1 in damaged condition.

Table 9.2: Meshes employed for the roll decay test of PRR1 in damaged condition.

Grid	Size of the elements inside compartments	Number of elements				
		Double bottoms	Storage rooms	Car deck	Outside compartments	Total
Coarse	0.400 m	11,808	46,944	99,990	80,300	239,042
Fine	0.283 m	30,954	143,774	null	115,830	290,558

The comparison of ship roll motions obtained on the coarse and fine grids is shown in Figure 9.5. The two computed results are nearly identical. Figure 9.6 shows the mass centre position of internal water predicted with the two meshes (expressed in the ship-fixed coordinate system). The maximum error between the numerical results is less than 0.05 m, which is very small compared to the ship breadth of 27.8 m and is acceptable concerning the mesh size. To clearly demonstrate the behaviour of floodwater in the compartments, two slices illustrated in Figure 9.7 are extracted from the compartment domain. The motions of internal water at the position of the two slices are shown in Figures 9.8 and 9.9. It is apparent that there is no water ingress on the car deck. The internal water demonstrates quasi-static behaviour under the current slow roll motion. The water surfaces computed on the coarse and fine grids are similar, which are nearly flat and horizontal. The above comparisons confirm that the mesh resolution based on the coarse grid arrangement is sufficient for this roll decay simulation.

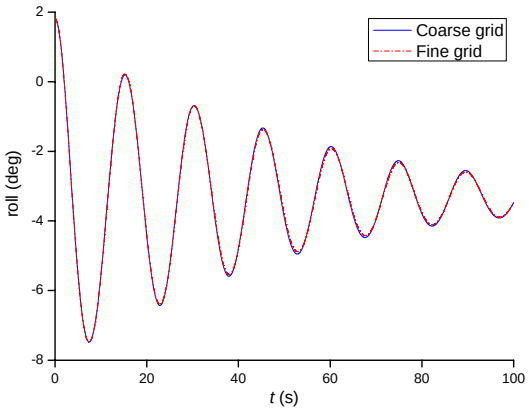

Figure 9.5: Comparison of the computed roll decay of PRR1 in damaged condition.

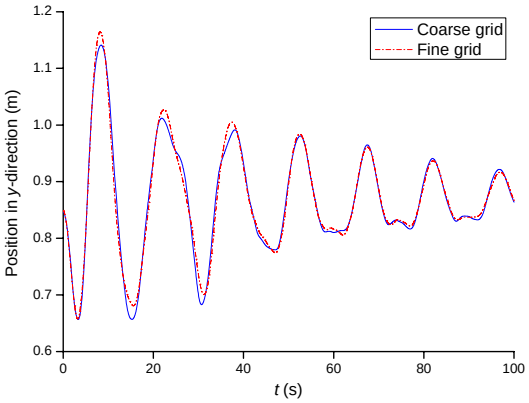

Figure 9.6: Comparison of the mass centre position in *y*-direction of internal water.

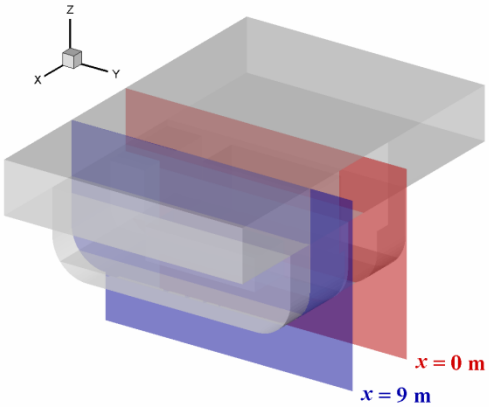

Figure 9.7: Sketch of the two slices extracted from the compartment domain.

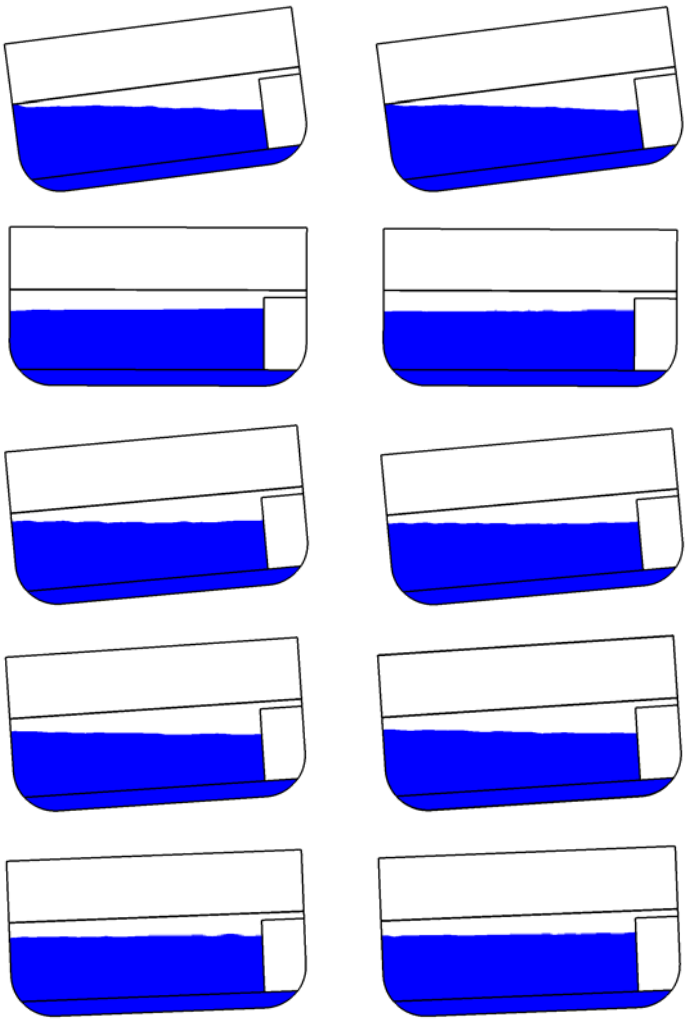

Figure 9.8: Snapshots of the water motion inside compartments at x=0 m (t=7.5, 15, 25, 50, 75 s) (Left: coarse grid, right: fine grid).

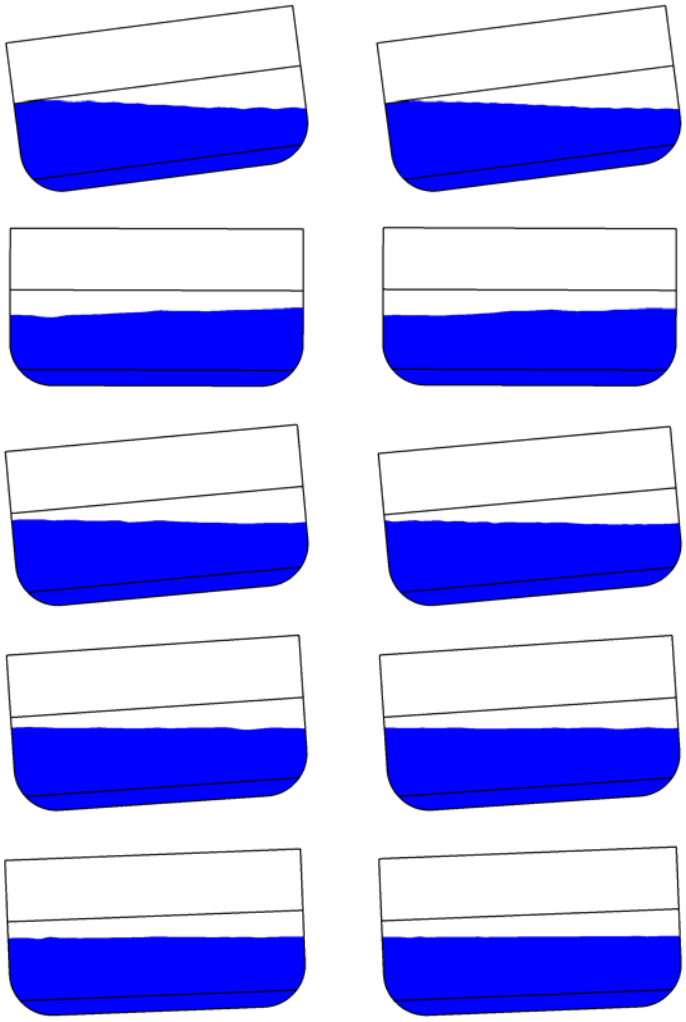

Figure 9.9: Snapshots of the water motion inside compartments at x=9 m (t=7.5, 15, 25, 50, 75 s) (Left: coarse grid, right: fine grid).

The comparison of ITTC benchmarking results (ITTC report, 2002) and the numerical results obtained by the hybrid method (on coarse grid) and by PROTEUS3 is shown in Figure 9.10. The model for floodwater motion adopted in PROTEUS3 is based on the empirical Bernoulli's equation plus the concept of moving lump mass (Jasionowski, 2001). In the ITTC benchmarking study, the adopted numerical tools are all based on the conventional method described in Section 3.1. The computed ship's natural roll frequencies are generally in good agreement with the experimental measurement except for the result of Participant 2, but the roll amplitudes in the numerical simulations differ largely with those in the model test. In the present

computation, the roll decay of the ship is reproduced reasonably well both by the hybrid method and by PROTEUS3 in comparison with the experimental data. The equilibrium roll angles in the two computations are −3.25°, which is in good agreement with the experimental measurement of −3.2°. The natural roll frequencies obtained by the hybrid method, PROTEUS3 and model test are 0.415, 0.403 and 0.432 rad/s, respectively, all of which shift from 0.483 rad/s in the case of an intact ship. Compared to the hybrid method, the roll amplitudes computed by PROTEUS3 are closer to the experimental measure in the first three periods. After four periods, the amplitudes are better predicted by the hybrid method compared to PROTEUS3 results. In the current test case, the ship's roll motion is slow and decays over time. Thus, the flooding process is quasi-static and the internal water surface is nearly flat and horizontal (see Figures 9.8 and 9.9). The simplified model for floodwater motion in PROTETS3 can yield satisfactory results. The improvement of numerical accuracy by the hybrid method is small.

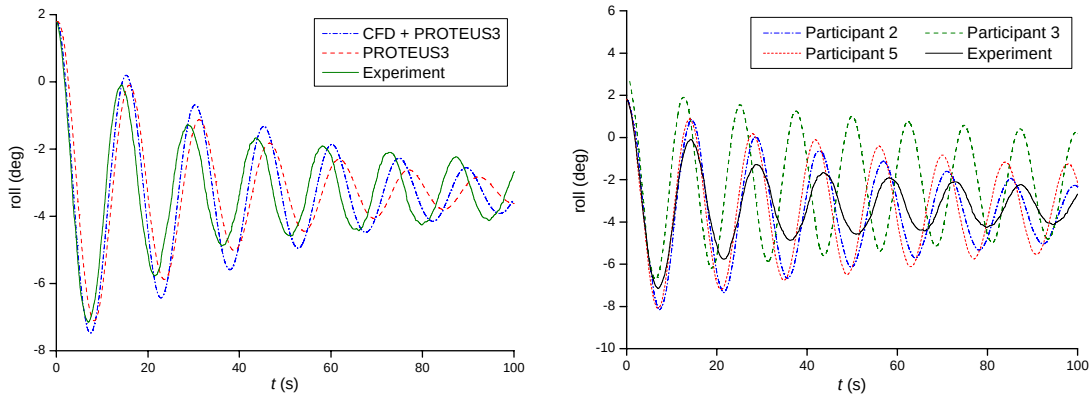

Figure 9.10: Comparison of the roll decay history of PRR1 in damaged condition (Left: present computation, right: ITTC benchmarking results).

Compared to the experimental data, the roll amplitudes computed with the hybrid method are over-predicted in the first 60 s. In the CFD simulation, wave reflection occurs and subsequently influences the motion of internal water once the radiation wave reaches the boundary. The non-physical perturbation can be reduced by

extending the simulation domain in the *x*- and *y*-directions. However, this treatment is not implemented in the present study considering the computational cost. Consequently, the roll amplitudes computed with the hybrid method become smaller than their experimental counterparts after 70 s. Besides the numerical error of CFD simulation, the discrepancy of numerical and experimental results is also attributed to the use of simplified mathematical model for the ship seakeeping calculation in damaged condition. In our study, the calculations of damaged ship hydrodynamics, which arise from external wave and viscous effect, are still based on the intact ship assumption, i.e., the effect of damaged opening on the flow around the hull is not considered in these calculations. The error due to this simplification can not be quantified at the time of present study; further investigation on this uncertainty is needed in future.

9.3 Ship Motion in Beam Seas

9.3.1 Case for Intact Ship

Before applying the hybrid method to the damaged ship flooding in waves, we first test the ability of PROTEUS3 to predict the motion of an intact ship in waves. The case of PRR1 without forward speed undergoing regular beam seas is tested. The selected wave heights (H_w) are 1.2 m and 2.4 m, respectively. Figures 9.11 and 9.12 show the comparisons of roll response amplitude operators (RAO) obtained by PROTEUS3 and model test (ITTC report, 2002). The computed RAOs are over-predicted at wave frequencies close to the natural roll frequency of the ship (0.483 rad/s). With the restriction of linear theory, the range of frequency for such discrepancy expands as the wave height increases. It is from 0.45 to 0.55 rad/s for the wave height of 1.2 m and from 0.4 to 0.6 rad/s for the wave height of 2.4 m. In the range of other frequencies, good agreement between the numerical and experimental

results is observed. Generally, the trends of computed RAOs changing with frequencies are consistent with the experimental data. The above comparisons demonstrate that the seakeeping solver PROTEUS3 can effectively predict the behaviour of an intact ship subjected to small amplitude wave.

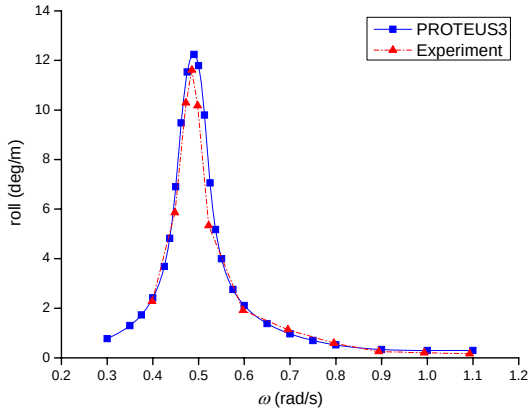

Figure 9.11: Comparison of the roll RAO of PRR1 in intact condition (H_w=1.2 m).

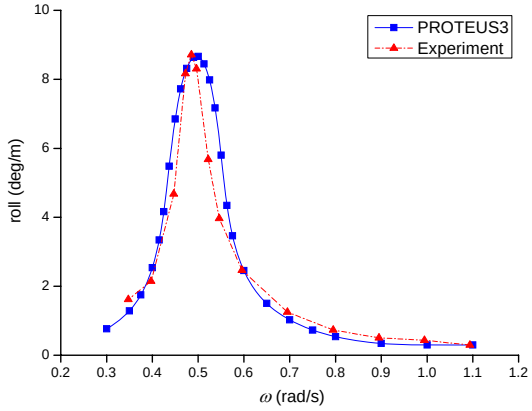

Figure 9.12: Comparison of the roll RAO of PRR1 in intact condition (H_w=2.4 m).

9.3.2 Case for Damaged Ship

The behaviour of damaged PRR1 subjected to waves without forward speed has also been extensively studied by several participants of the ITTC benchmarking study (ITTC report, 2002). However, all numerical tools developed by the participants are based on the conventional method described in Section 3.1. They can not properly

model the floodwater dynamics at the damaged opening and in the compartments. The benchmarking result, as shown in Figure 9.13, shows that neither the peak response frequency nor its magnitude in the computations agrees with the experimental values. To assess its performance in damaged ship flooding in waves, we apply our hybrid method to the same case.

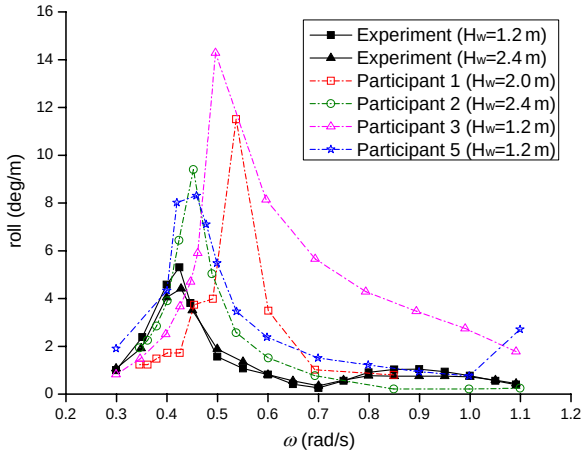

Figure 9.13: Results of ITTC benchmarking study for PRR1 in damaged condition.

A regular wave with a height of 1.2 m and a heading angle of $3\pi/2$ is selected in the numerical study. The wave frequencies range from 0.3 to 1.1 rad/s. Table 9.3 summarizes the wave parameters for different frequencies. A sketch of computational domain for the CFD simulation is shown in Figure 9.4. On the top boundary, the pressure is set to be the atmospheric pressure. The hydrostatic pressure corresponding to the initial water height is imposed on the bottom boundary. On the right, front and back boundaries, the initial water height and hydrostatic pressure are imposed. The elevation and velocity of incident wave are imposed on the left boundary. The no-slip wall condition is imposed on the surfaces of hull and compartments. Two meshes that are listed in Table 9.4 are generated for the current case. In the floodable compartments, the grid elements are uniformly arranged in the *x*-, *y*- and *z*-directions. Outside the compartments, the element size in the *z*-direction (wave height direction) should not exceed 5% of the wave height near the free

surface region to accurately capture the wave profile. However, this measure of element distribution consumes considerable computational cost and is not adopted in the present study. To reduce the computational cost, the following mesh arrangement outside the compartments is employed. In the *z*-direction, the element size near the free surface is 0.4 and 0.283 m for the coarse and fine grids, respectively. It becomes larger with an expansion factor of approximately 1.2 in the region away from the free surface. In the *y*-direction (wave propagation direction), the element size is 2.5% of the wavelength corresponding to a wave frequency of 1.1 rad/s. In the *x*-direction (ship length direction), the element size gradually expands away from the damaged opening with an expansion factor of approximately 1.1. Table 9.3 shows that the wave steepness is very small for the wave height of 1.2 m, which indicates that the effect of the selected sea wave on the floodwater motion is small. Additionally, the ship hydrodynamic forces outside the compartments are obtained using the seakeeping solver. Thus the mesh arrangement outside the compartments has limited influence on the numerical solution and the one we employ herein is reasonable. The computational time step should not exceed 5‰ of the wave period and should ensure the cell Courant number within the limit of 0.5. According to these criteria, two constant time steps of 0.02 s and 0.01 s are adopted for the computations on the coarse and fine grids, respectively. For each wave frequency, the simulation runs up until the ship motion becomes stable. Approximately 88 and 317 CPU hours are required to complete a 200-s simulation with the coarse and fine grids, respectively.

Table 9.3: Wave parameters for different frequencies (H_w=1.2 m).

Wave frequency (rad/s)	Wave period (s)	Wavelength (m)	Wave steepness
0.3	20.94	684.87	0.002
0.5	12.57	246.55	0.005
0.7	8.98	125.79	0.010
0.9	6.98	76.10	0.016
1.1	5.71	50.94	0.024

Table 9.4: Meshes employed for the flooding of PRR1 in waves.

Grid	Size of the elements inside compartments	Number of elements				
		Double bottoms	Storage rooms	Car deck	Outside compartments	Total
Coarse	0.400 m	11,808	46,944	99,990	93,720	252,462
Fine	0.283 m	30,954	143,774	284,177	144,180	603,085

Because the wave frequency significantly influences both the ship and floodwater motions, a study of the grid dependence is performed to check the mesh validity for different wave frequencies. Three frequencies of 0.415, 0.65 and 0.9 rad/s, which respectively represent the low, medium and high frequencies, are selected for the test. Figures 9.14 through 9.16 compare the ship roll motions obtained on the coarse and fine grids. It is apparent that the results computed with the two grids are in good agreement. Note that the computational cost on the coarse grid is much lower than that on the fine grid. Thus, the coarse grid is employed in the subsequent numerical simulations for the wave frequencies ranging from 0.3 to 1.1 rad/s.

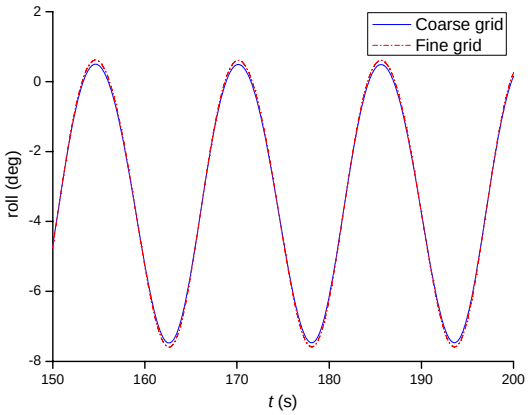

Figure 9.14: Comparison of the damaged behaviour of PRR1 in wave (ω=0.415 rad/s).

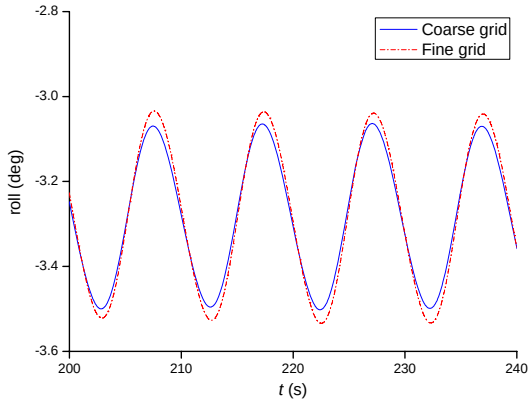

Figure 9.15: Comparison of the damaged behaviour of PRR1 in wave (ω=0.65 rad/s).

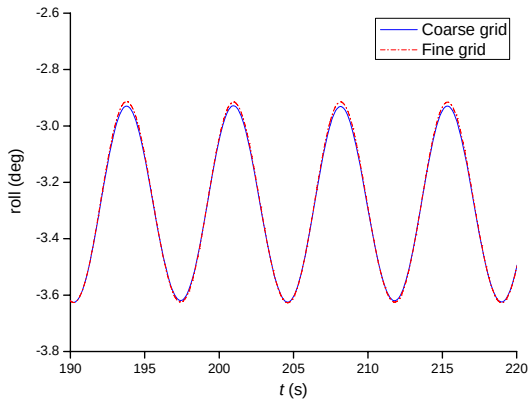

Figure 9.16: Comparison of the damaged behaviour of PRR1 in wave (ω=0.9 rad/s).

For different wave frequencies, the roll RAOs obtained by the hybrid method, PROTEUS3 and the model test are shown in Figure 9.17. The frequencies of peak response obtained by these three methods are approximately 0.415, 0.41 and 0.42 rad/s, respectively, all of which coincide with the natural frequencies obtained in the roll decay test and shift from 0.49 rad/s in the intact condition. Compared to the case of an intact ship (see Figure 9.11), the peak response for the damaged ship is weakened significantly both in the experiment and in the computation based on the hybrid method. However, the decrease of peak response is slight in the computation based on PROTEUS3. Generally, the roll RAOs obtained by PROTEUS3 are dissatisfactory in comparison with the experimental data. At the presence of consecutive excitation force, the dynamic effect of internal water cannot be ignored.

The behaviour of internal water is various along with the change of wave frequency and change of ship's motion amplitude. These variations will be discussed later. Thus, it is unlikely to describe the free surface motion based on simple assumptions as used in PROTEUS3. Compared to PROTEUS3 results, it is clear that the numerical accuracy is greatly improved by the hybrid method. The ship's roll motions predicted with the two numerical methods at wave frequency of 0.4 are shown in Figure 9.18. Except for different roll amplitudes, the ship shows similar behaviours in the two simulations.

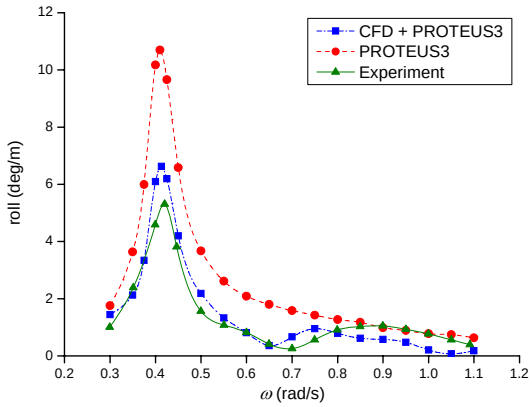

Figure 9.17: Comparison of the roll RAO of PRR1 in damaged condition.

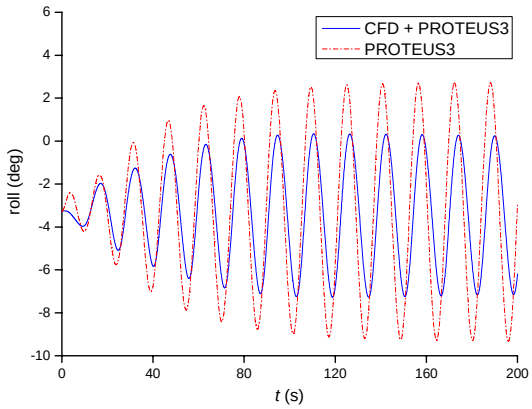

Figure 9.18: Comparison of the time history for roll motions of PRR1 in wave obtained by different numerical method (ω=0.4 rad/s).

For the wave frequencies that are lower than 0.6 rad/s, although the peak magnitude is over-predicted by the hybrid method, the change trend of computed RAOs is

consistent with its experimental counterpart. As the wave frequency increases further, a second peak of RAO is observed both in the experiment and computation based on the hybrid method. Its magnitude predicted with our method (approximately 1.0 deg/m) agrees well with the experimental measurement. The later discussion will show that the presence of this small peak is related to the floodwater motion in the damaged compartments. When the roll moment induced by internal water motion is large and in phase with the one excited by external sea wave, a larger resultant moment originates and excites the ship to roll with larger amplitude. In the computation, the frequency corresponding to the second peak response is 0.75 rad/s, which disagrees with the response at 0.85 rad/s in the experiment.

The disagreement between computation based on the hybrid method and experiment is, on one hand, due to the neglect of damaged opening effect on calculation of diffraction force, added mass and damping coefficient using the seakeeping solver. On the other hand, the disagreement is attributed to the boundary reflection in the CFD simulation. On the left boundary, the wave properties (wave elevation and fluid velocity) should include the components of incident, diffraction and radiation waves. Because the damaged opening is not considered in solving the diffraction and radiation problems, the corresponding hydrodynamics can not be accurately predicted. As a result, we only specify the properties of incident wave on the left boundary of CFD simulation domain. If the boundary is located far enough from the ship (generally two times of ship length), numerical error due to this boundary definition is negligible. However, to reduce the computational cost, the distance between the left boundary and the ship is not taken too long herein. In such a case, the perturbation from the non-physical boundary influences the pressure distribution around the damaged opening and consequently changes the behaviour of floodwater inside the compartments.

To reveal the mechanism behind the phenomena observed in Figure 9.17, the

interactive dynamics between the damaged ship, external sea wave and floodwater will be analyzed based on the numerical simulation. We first demonstrate the behaviour of floodwater inside the compartments. For this purpose, four slices illustrated in Figure 9.19 are extracted from the compartment domain. Figures 9.20 through 9.23 show the motions of internal water at the position of the four slices. For the wave frequency of 0.415 rad/s, a small amplitude wave is generated inside the lower compartments. Its pattern mainly varies along the transverse direction, indicating that the change of compartment geometry (internal layout and damaged opening) in the longitudinal direction has little effect on the free surface motion. On the car deck, there is only a very small amount of water accumulating around the damaged opening. For the wave frequencies of 0.65 and 0.9 rad/s, it is apparent that no water floods into the compartment above car deck. Since the amplitude of ship roll motion is relatively small, the free surface in the lower compartments varies little along the transverse and longitudinal directions. It looks like a horizontal plane. For the wave frequency of 0.75 rad/s, which is close to the natural frequency of internal water motion, the phenomenon of resonant sloshing occurs in the compartments. Although the amplitude of ship roll motion is small, the nonlinear behaviour of internal water becomes notable. It is apparent that the elevation of free surface changes abruptly both along the transverse and longitudinal directions.

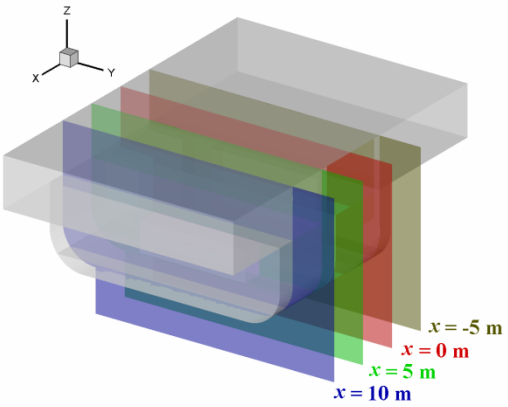

Figure 9.19: Sketch of the four slices extracted from the compartment domain.

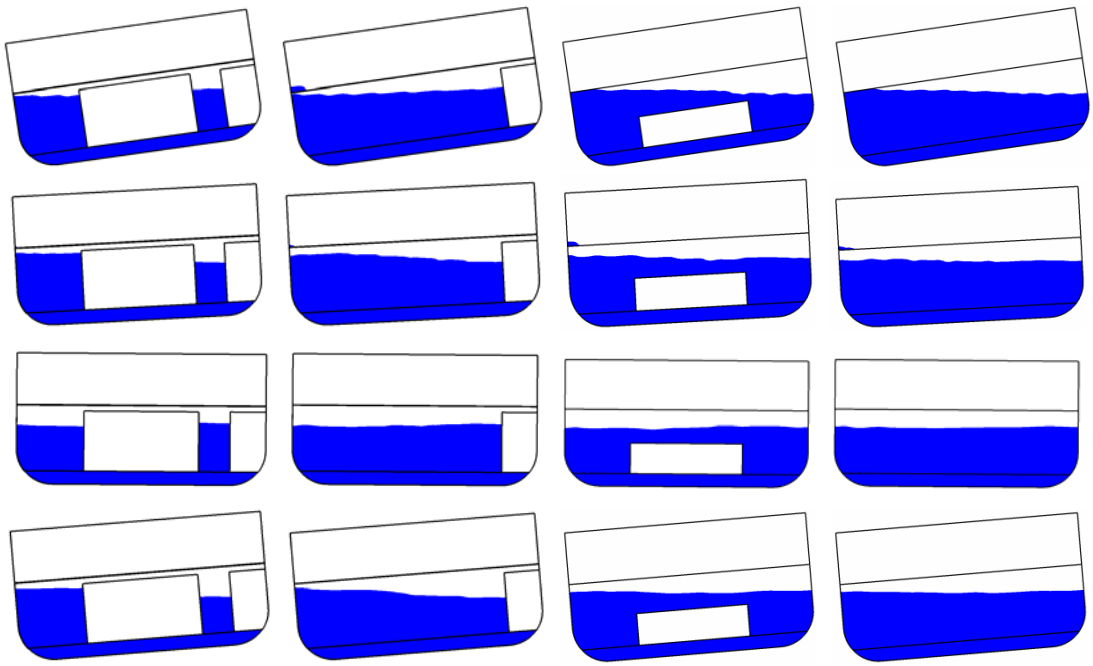

Figure 9.20: Snapshots of the internal water motion in damaged condition for the wave frequency of 0.415 rad/s
(From left to right: x=−5, 0, 5, 10 m) (From up to down: t=177.5, 182.5, 185, 190 s).

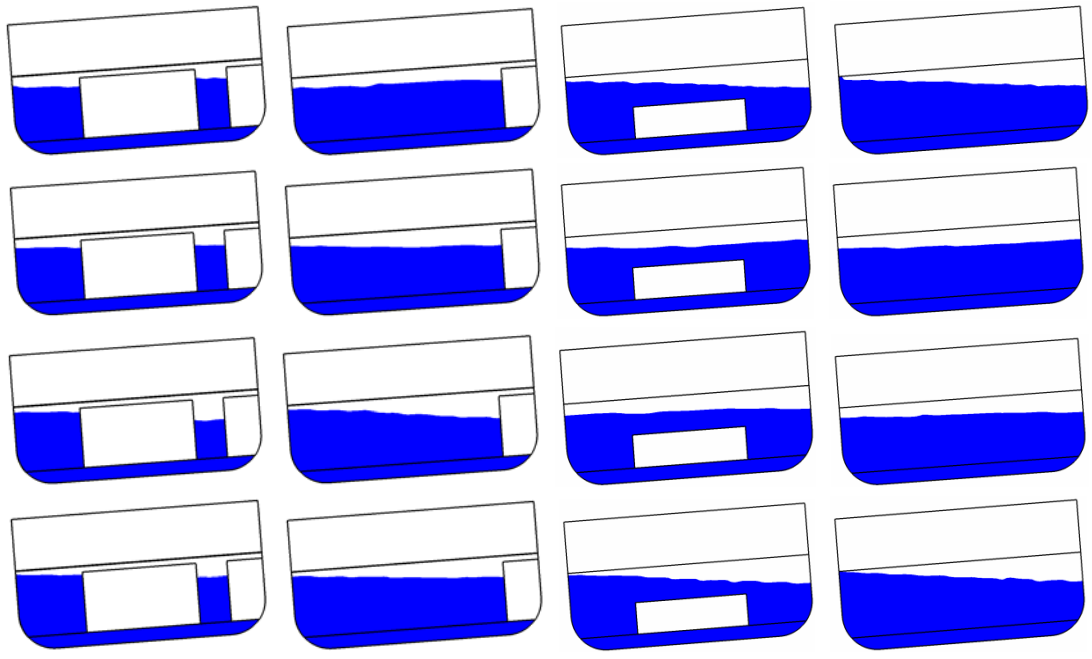

Figure 9.21: Snapshots of the internal water motion in damaged condition for the wave frequency of 0.65 rad/s
(From left to right: x=−5, 0, 5, 10 m) (From up to down: t=205, 207.5, 210, 212.5 s).

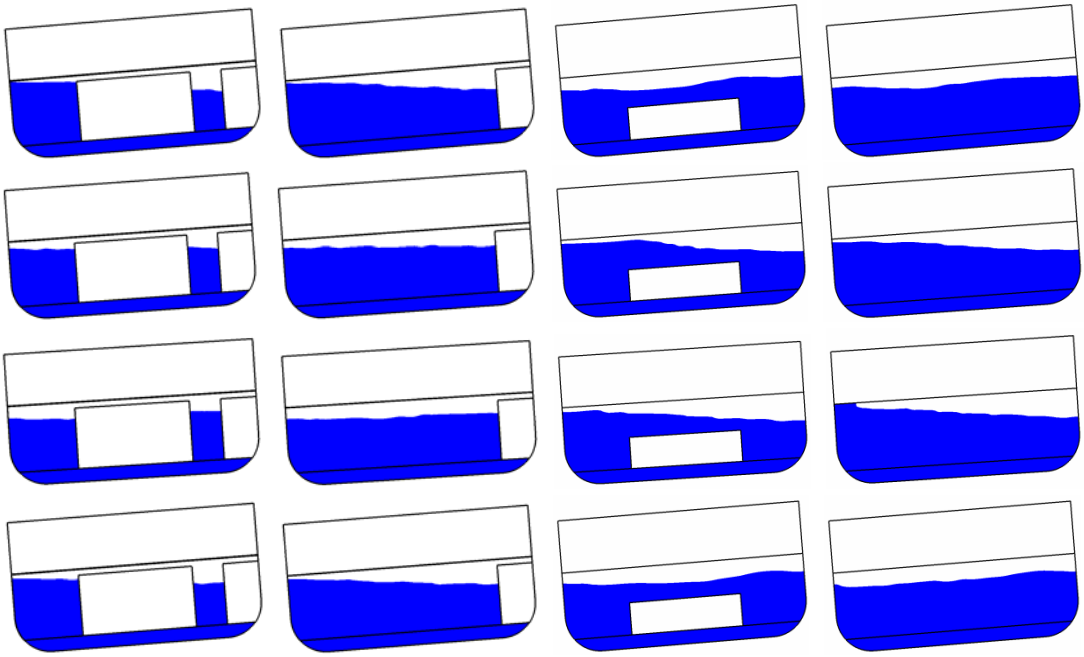

Figure 9.22: Snapshots of the internal water motion in damaged condition for the wave frequency of 0.75 rad/s
(From left to right: x=−5, 0, 5, 10 m) (From up to down: t=192.5, 195, 197.5, 200 s).

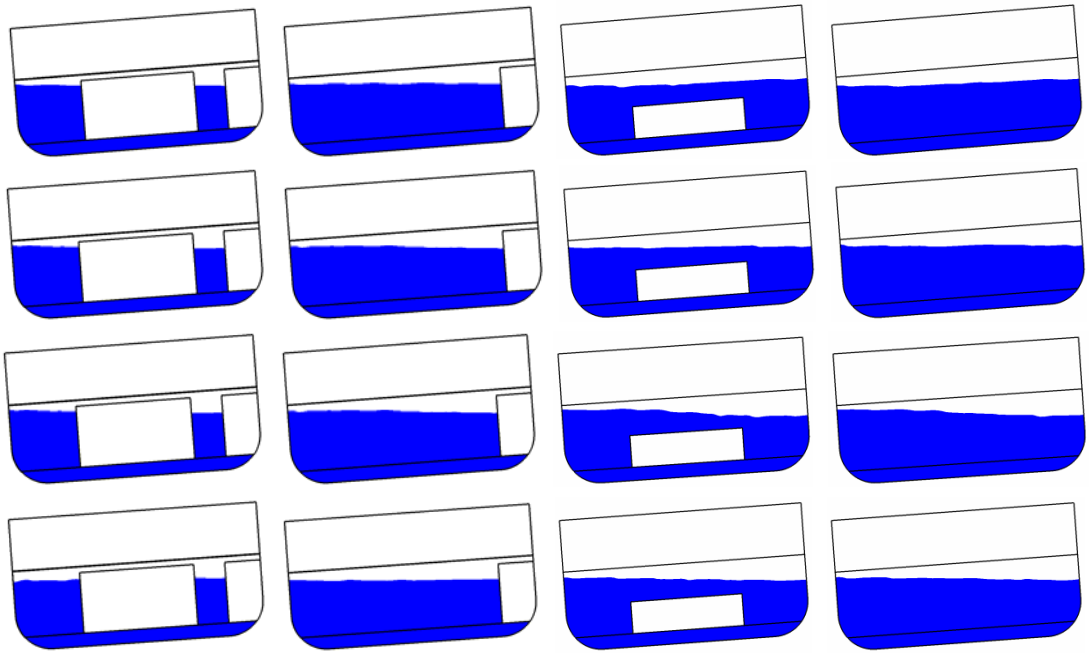

Figure 9.23: Snapshots of the internal water motion in damaged condition for the wave frequency of 0.9 rad/s
(From left to right: x=−5, 0, 5, 10 m) (From up to down: t=197.5, 199, 201, 202.5 s).

The hydrodynamic roll moments acting on a damaged ship and the corresponding roll motion are shown in Figures 9.24 through 9.27, in which the wave excitation moment includes the Froude-Krylov and diffraction components; the radiation moment includes the viscous correction based on the Ikeda's method; the dynamic sloshing moment is obtained by deducting the hydrostatic component from the total sloshing moment, while the internal water surface is considered flat and horizontal in the computation of hydrostatic component. The resultant roll moment of wave excitation and sloshing components, which has significant influence on the ship roll amplitude, is also shown in these figures. Because the Froude-Krylov force is calculated on the instantaneous wetted surface of the hull, the change in wave excitation force is not sinusoidal. For the wave frequency of 0.415 rad/s, the roll moment of sloshing is much larger than the other two roll moments. The sloshing moment is approximately 20° phase lag relative to the ship roll motion and radiation moment; whereas it is nearly 120° phase lag relative to the wave excitation moment. The resultant excitation moment is large. Around the natural roll frequency of the ship, the hydrodynamic roll moments demonstrate similar characteristic. For the wave frequency of 0.65 rad/s, the three components of roll moment appear roughly sinusoidal. The sloshing moment is almost in phase with the ship roll motion. Compared to the wave excitation moment, the sloshing moment is nearly 180° phase lag, whereas their amplitudes are close. Therefore, the resultant moment is relatively small, and the ship roll response becomes very small. For the wave frequency of 0.75 rad/s, because the internal water exhibits nonlinear behaviour (see Figure 9.22), its impact load on the compartments differs clearly with that in the case of wave frequency of 0.65 rad/s. The amplitude of sloshing moment is larger than that of the wave excitation moment, whereas the phase difference between the two moments is approximately 105°. It is clear that an even larger resultant roll moment is produced. This moment excites roll motion of the ship in this frequency range and results in the presence of a second peak of the roll response (see Figure 9.17). The sloshing

moment is nearly 150° phase lag relative to the ship roll motion. As the wave frequency increases further to 0.9 rad/s, the three components of roll moment and the resultant moment decrease. The motion response of the ship decreases as well. The phase difference between the sloshing moment and ship roll motion approaches 180°.

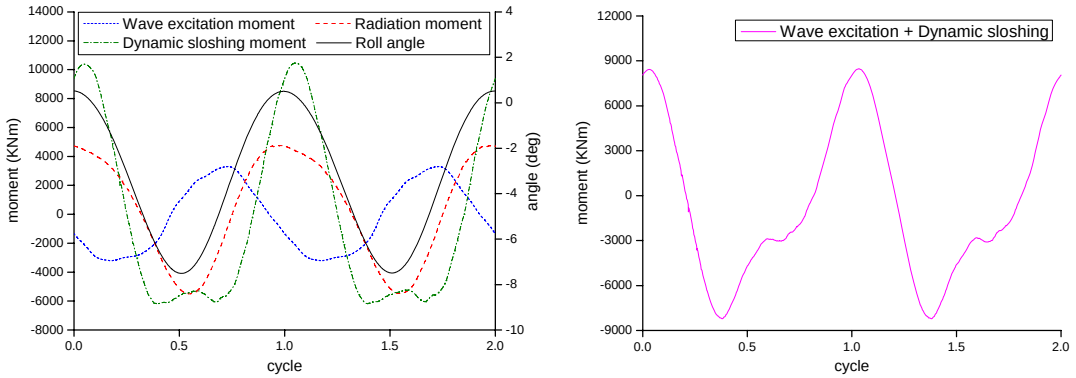

Figure 9.24: The hydrodynamic roll moment acting on a damaged ship and the corresponding roll motion (ω=0.415 rad/s).

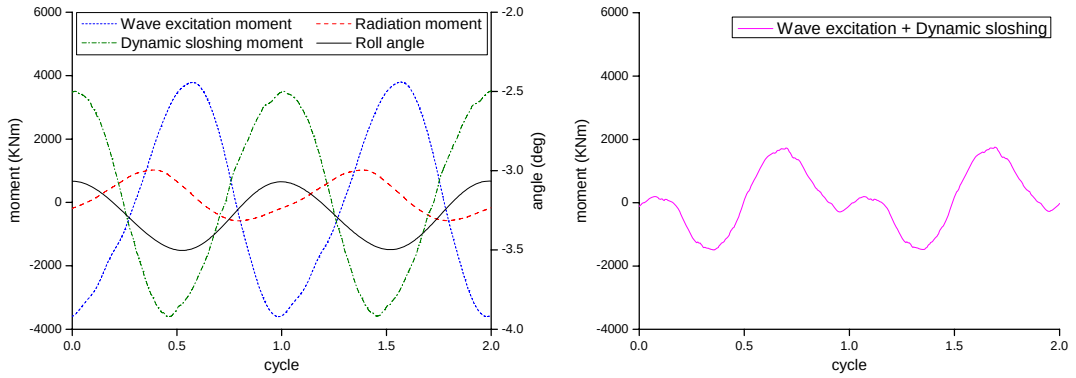

Figure 9.25: The hydrodynamic roll moment acting on a damaged ship and the corresponding roll motion (ω=0.65 rad/s).

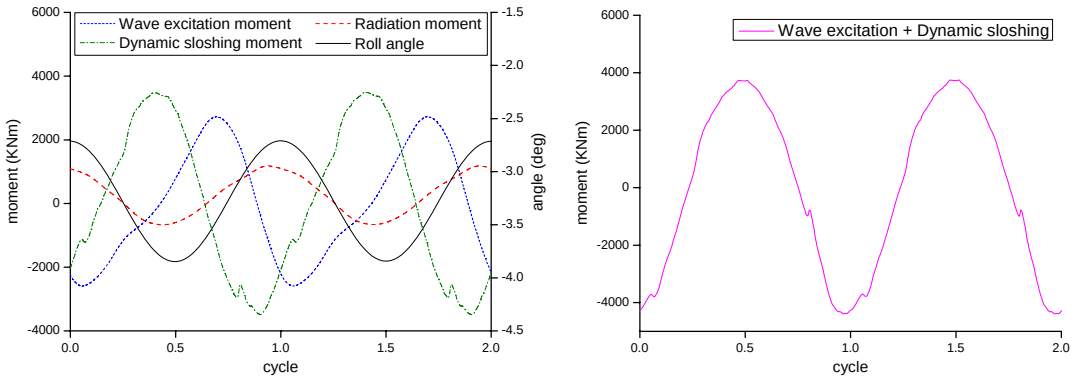

Figure 9.26: The hydrodynamic roll moment acting on a damaged ship and the corresponding roll motion (ω=0.75 rad/s).

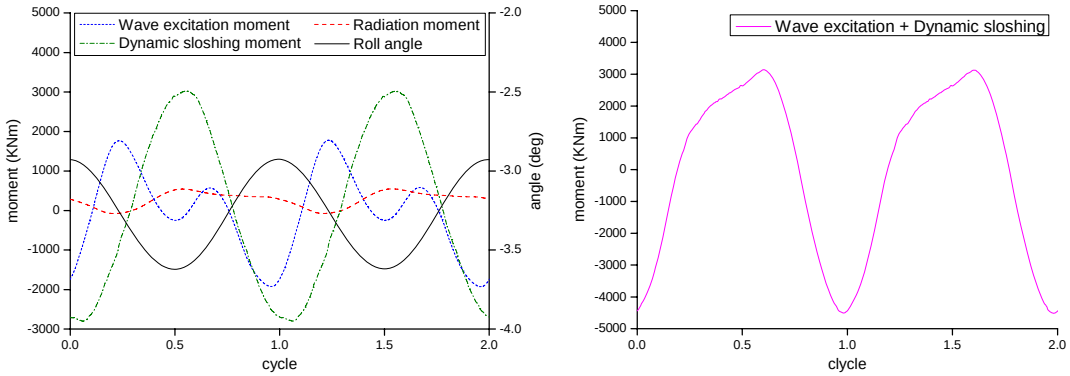

Figure 9.27: The hydrodynamic roll moment acting on a damaged ship and the corresponding roll motion (ω=0.9 rad/s).

The flow rates through the damaged opening for wave frequencies of 0.415, 0.65 and 0.9 rad/s are shown in Figure 9.28, where a positive quantity represents the ingression of water into the compartments. It is shown that the amplitude of flow rate decreases as the frequency increases. Their phase angles relative to the ship roll motion are approximately 105°, 110° and 140°, respectively. Figure 9.29 shows the mass centre position of internal water (expressed in the ship-fixed coordinate system). The motion of mass centre almost follows the sinusoidal movement for wave frequencies of 0.65 and 0.9 rad/s; whereas the motion is complex for wave frequency of 0.415 rad/s due to free surface motion on car deck and large amount of water ingress/egress. Figure 9.30 shows the mass of water ingress during a wave period for frequencies ranging from 0.3 to 1.1 rad/s. At frequency of 0.3 rad/s, the mass of water ingress is approximately 6% of the average mass of internal water; whereas it is less than 2% of the average mass for the frequencies higher than 0.7 rad/s. Since the flow rate depends on the ship behaviour, internal water motion and external wave motion, the three of which vary largely for different wave frequencies. Thus, although the amount of water ingress decreases as the wave frequency increases, fluctuations are observed at around the natural frequency of ship motion and at high frequencies. The above comparisons indicate that the use of simple hydraulic model in the conventional method for driving water ingress/egress can lead to large numerical error.

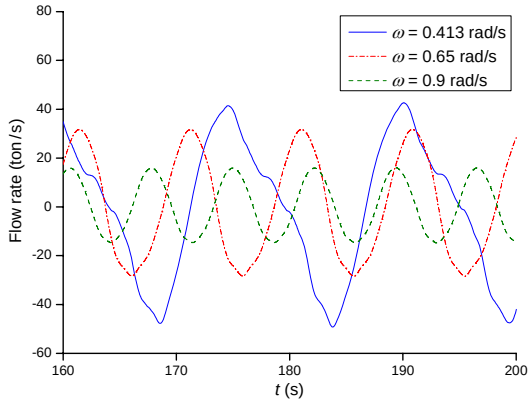

Figure 9.28: Flow rate through the damaged opening (ω=0.415, 0.65, 0.9 rad/s).

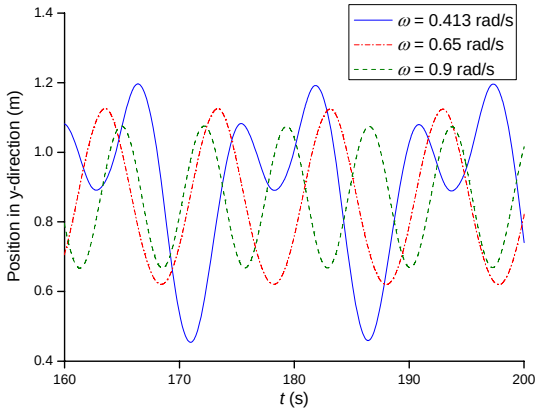

Figure 9.29: Mass centre position of the internal water in y-direction (ω=0.415, 0.65, 0.9 rad/s).

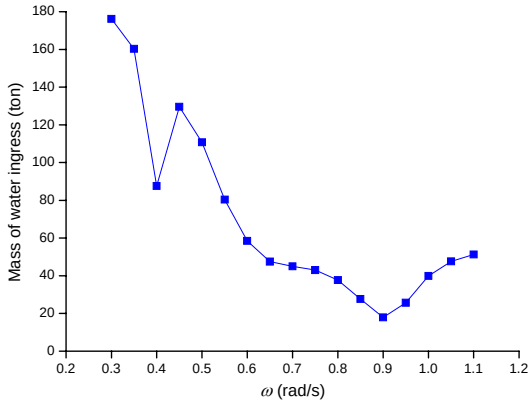

Figure 9.30: Mass of water ingress into the compartments during a wave period for different frequencies.

9.3.3 Effect of Water Ingress/Egress

The above numerical analysis shows that water flooding is highly coupled with ship motion and water sloshing inside the compartments. To investigate the effect of water ingress/egress on the behaviours of the ship and internal water, another numerical test is carried out by using the present hybrid method. In this test, the Ro-Ro ferry PRR1 is considered intact and undergoing regular beam seas without forward speed. Its compartments are partially filled with water, the level of which is 7.02 m above the base. The height of external sea wave is selected as 1.2 m. The main difference between the current test case and the case discussed in Section 9.3.1 is whether there is water inside the compartments or not, whereas that between the current case and the one discussed in Section 9.3.2 is whether the ship is damaged or not.

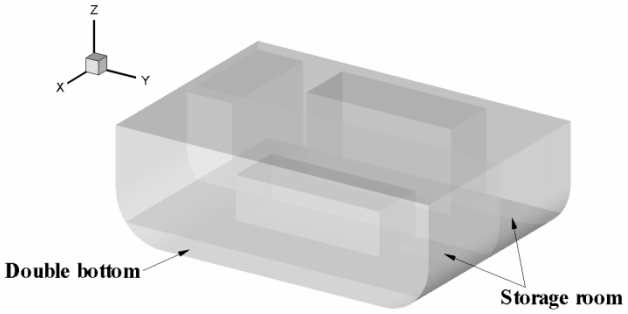

Figure 9.31: CFD simulation domain for the case of PRR1 in intact condition.

Since water exchange between the compartments and external flow field does not exist in the current test case, there is no need to calculate the flow field inside the compartment above car deck and outside the hull using the NS solver. Figure 9.31 shows the CFD simulation domain that just includes the lower compartments of the ferry. The no-slip wall condition is imposed on the surface of compartments. Referring to the coarse grid arrangement listed in Table 9.2, a uniform mesh with sizes of 0.4 m in the *x*-, *y*- and *z*-directions is generated herein and the total number of elements is 58,752. A constant computational time step of 0.02 s is used to ensure the cell Courant number within the limit of 0.5. It takes 20 CPU hours to complete a

200-s simulation.

The comparison of computed roll RAO for the current test case (intact ship with internal water) and the two previous cases (intact ship without internal water and damaged ship with internal water) is shown in Figure 9.32. For the two cases with internal water, the frequencies of first peak response (natural roll frequency of the ship) agree perfectly, both of which are 0.415 rad/s and shift from 0.49 rad/s in the case without internal water. This comparison demonstrates that the shift of natural roll frequency of the ship is attributed to the presence of water in the lower compartments but has little relationship with water ingress/egress. On the other hand, the peak magnitudes in the cases with internal water decrease clearly compared to the case without internal water, which indicates that the decrease of ship response is mainly attributed to the water motion inside compartments. Note that the decrease of peak response for the damaged ship is larger than that for the intact ship, allowing the conclusion that water ingress/egress further weakens the ship response. As the wave frequency increases, a second peak of roll response at around wave frequency of 0.75 rad/s is observed in the cases with internal water. The magnitude of this peak for the intact ship is nearly three times as large as that for the damaged ship. At this range of frequency, resonant sloshing in the compartments occurs, as discussed in Section 9.3.2. The large difference between the magnitudes of these two peaks indicates that water ingress/egress has significant influence on the sloshing of internal water and consequently influences the ship motion significantly. These influences will be discussed later. For the wave frequency higher than 1.0 rad/s, the ship responses in the three test cases are close, indicating that the influence of floodwater motion on the ship behaviour becomes small.

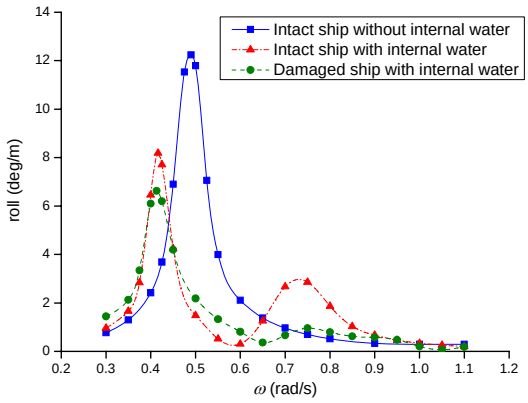

Figure 9.32: Comparison of the computed roll RAO of PRR1 in different test conditions (H_w=1.2 m).

The previous comparisons show that the effect of water ingress/egress on the ship motion cannot be neglected, in particular when the oscillation frequency of the ship (wave frequency) is close to the natural frequency of internal water motion (resonant sloshing frequency). To distinguish the effect of water ingress/egress on the motion of internal water, four slices illustrated in Figure 9.33 are extracted from the compartment domain. Figures 9.34 through 9.37 show the motions of internal water at the position of the four slices. For the wave frequency of 0.415 rad/s, the elevation of free surface inside the compartments varies smoothly along the transverse direction; whereas its variation along the longitudinal direction is inappreciable. Generally, the profile of water surface in the current case of intact ship is similar to that in the case of damaged ship (see Figure 9.20), which indicates that the effect of water ingress/egress on the free surface motion inside the compartments is small. For the wave frequency of 0.6 rad/s, sloshing phenomenon inside the compartment starts to become notable. The free surface appears no longer flat and horizontal compared to that in the damaged ship case (see Figure 9.21). As the wave frequency increases to 0.75 rad/s, the motion of internal water shows strong non-linearity. A large deformation of the water surface is observed along the transverse and longitudinal directions. In a motion period, the sloshing water impacts on the vertical wall of compartment, climbs up the obstacle and hits the compartment's ceiling. Then, the water overturns and flows violently towards the opposite wall. Compared to the case

of damaged ship (see Figure 9.22), it is apparent that the sloshing phenomenon is much stronger in the current case. The above comparisons demonstrate that water ingress/egress largely suppress the sloshing effect around the resonant sloshing frequency. As the wave frequency further increases to 0.9 rad/s, the notable sloshing phenomenon disappears. The water surface tends to be flat and horizontal. These characteristics of internal water are similar to those in the case of damaged ship (see Figure 9.23). It can be concluded that the effect of water ingress/egress on the free surface motion inside compartments becomes insignificant as the wave frequency increases further away from the resonant sloshing frequency.

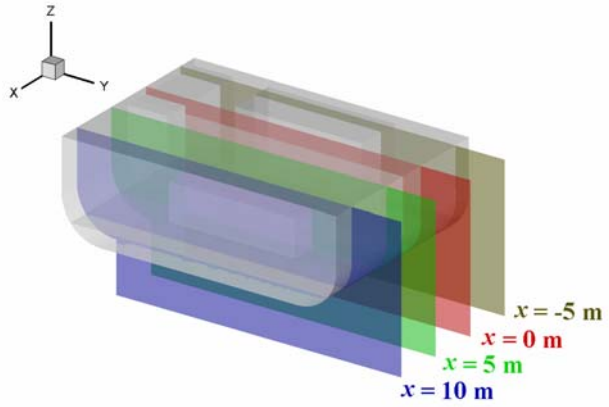

Figure 9.33: Sketch of the four slices extracted from the compartment domain.

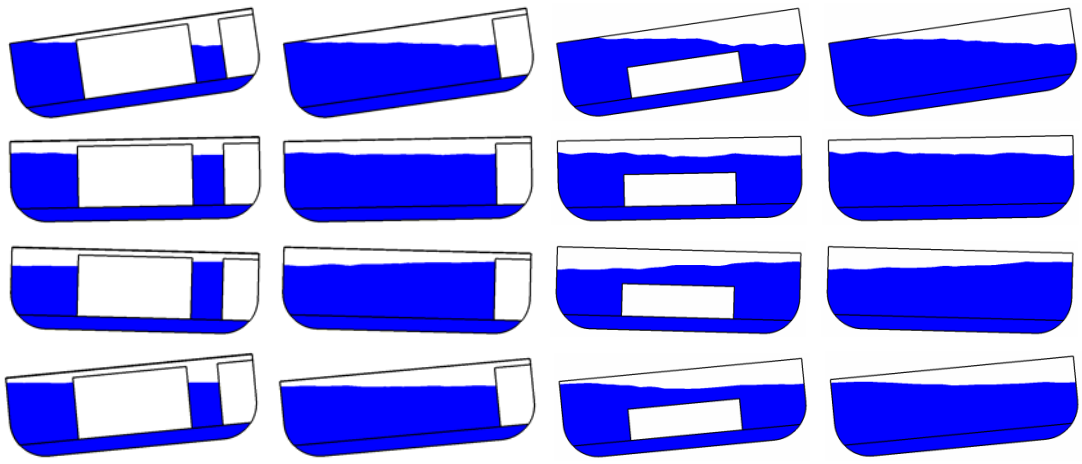

Figure 9.34: Snapshots of the internal water motion in intact condition for the wave frequency of 0.415 rad/s
(From left to right: x=−5, 0, 5, 10 m) (From up to down: t=220, 225, 227.5, 232.5 s).

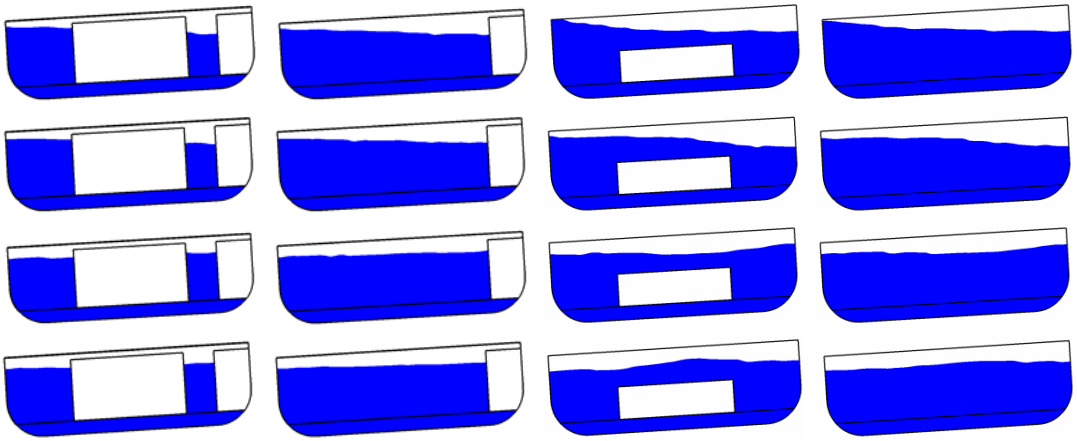

Figure 9.35: Snapshots of the internal water motion in intact condition for the wave frequency of 0.6 rad/s
(From left to right: x=−5, 0, 5, 10 m) (From up to down: t=280, 282.5, 285, 287.5 s).

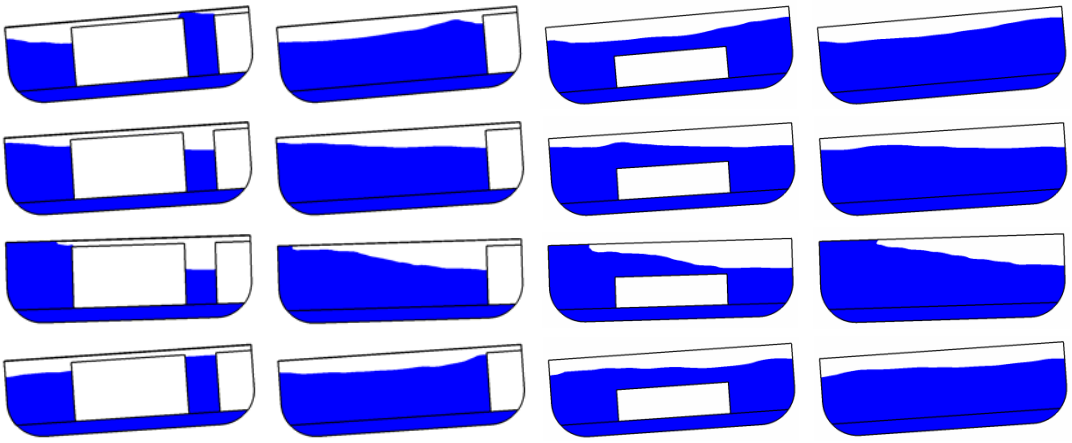

Figure 9.36: Snapshots of the internal water motion in intact condition for the wave frequency of 0.75 rad/s
(From left to right: x=−5, 0, 5, 10 m) (From up to down: t=235, 237.5, 240, 242.5 s).

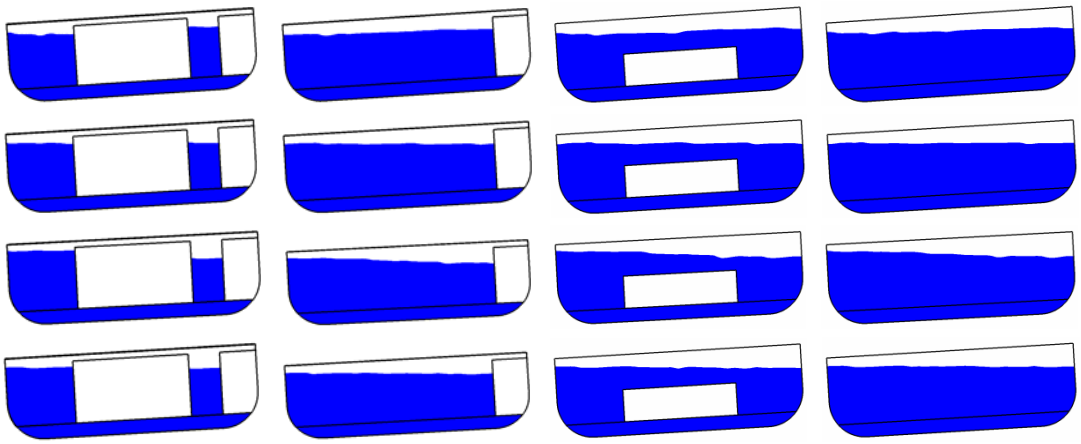

Figure 9.37: Snapshots of the internal water motion in intact condition for the wave frequency of 0.9 rad/s
(From left to right: x=−5, 0, 5, 10 m) (From up to down: t=225, 226.5, 228, 230 s).

The hydrodynamic components of roll moment acting on an intact ship and the corresponding roll motion are shown in Figures 9.38 through 9.41, in which the meaning of each component has been specified in Section 9.3.2. For the wave frequency of 0.415 rad/s, the sloshing moment is close to the radiation moment. These two moments are almost in phase with the ship roll motion. The sloshing moment is much larger than the wave excitation moment and approximately 90° phase lag relative to the later one. The sloshing moment in the current case is totally different from that in the damaged ship case (see Figure 9.24), which indicates that water ingress/egress significantly influences the liquid load on the compartments. For the wave frequency of 0.6 rad/s, the sloshing moment is nearly 180° phase lag relative to the wave excitation moment. The phase difference results in a comparatively small resultant moment, which leads to the small amplitude motion of the ship. Due to the sloshing effect, its induced moment is approximately 150° phase lag relative to the ship roll motion; whereas they are almost in phase in the damaged ship case (see Figure 9.25). Such discrepancy between the intact and damaged ship cases is attributed to the influence of water ingress/egress on the sloshing effect as discussed previously. For the wave frequency of 0.75 rad/s, the sloshing moment is much larger than the other two moments due to the strong sloshing effect. The local

peaks observed in the curve of sloshing moment are due to water impact on the compartment ceiling. The sloshing moment is approximately 180° phase lag relative to the ship roll motion and radiation moment; whereas it is nearly 85° phase lag relative to the wave excitation moment. Because the sloshing moment is dominant compared to the wave excitation moment, its characteristic is almost retained in the resultant moment that excites the ship near this frequency. The amplitude of resultant excitation moment in the current case is approximately four times as large as that in the damaged ship case (see Figure 9.26). Thus, in these two cases the ship responses around the resonant sloshing frequency differ largely, as shown in Figure 9.32. The comparison indicates that the effect of water ingress/egress largely weakens the sloshing motion of internal water and consequently reduces its impact load. For the wave frequency of 0.9 rad/s, the radiation moment is negligible in comparison with the sloshing moment, whose amplitude is nearly twice as large as that of the wave excitation moment. Except for the amplitude, the characteristics of sloshing moment in the current case are similar to those in the damaged ship case (see Figure 9.27). In these two cases, the change trends of sloshing moment are almost sinusoidal and their phase angles relative to the ship roll motion are approximately 180°. The comparison demonstrates that the effect of water ingress/egress on the motions of ship and internal water becomes small as the wave frequency further increases.

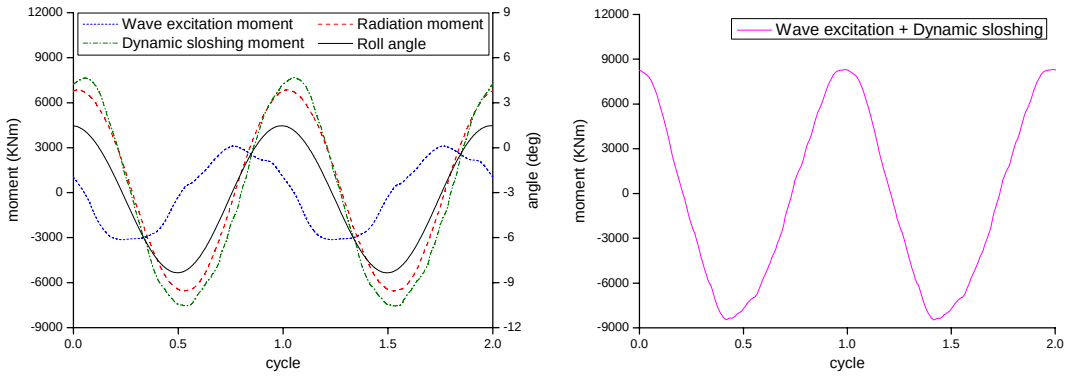

Figure 9.38: The hydrodynamic roll moment acting on an intact ship and the corresponding roll motion (ω=0.415 rad/s).

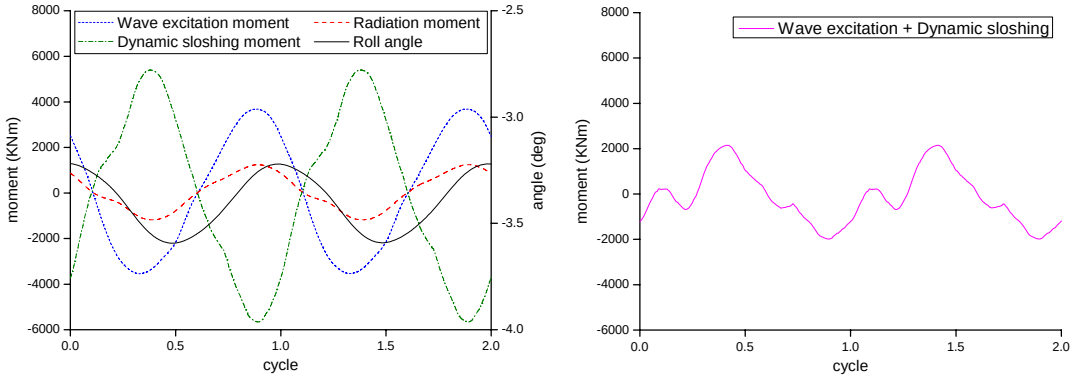

Figure 9.39: The hydrodynamic roll moment acting on an intact ship and the corresponding roll motion (ω=0.6 rad/s).

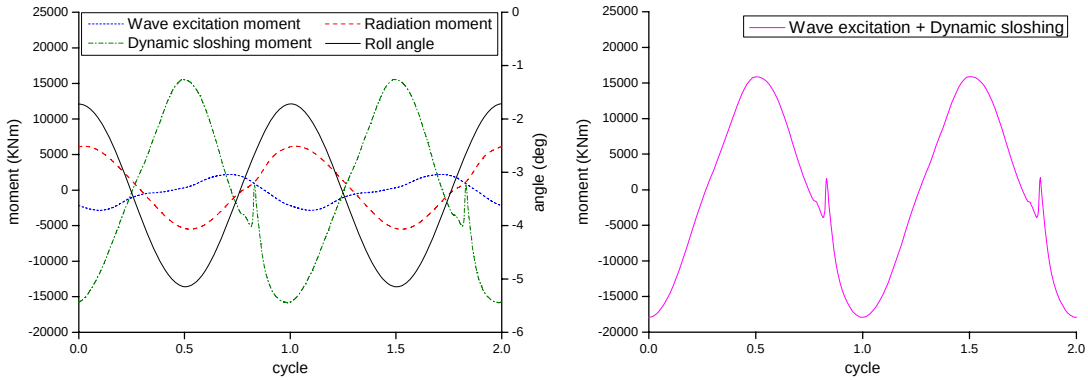

Figure 9.40: The hydrodynamic roll moment acting on an intact ship and the corresponding roll motion (ω=0.75 rad/s).

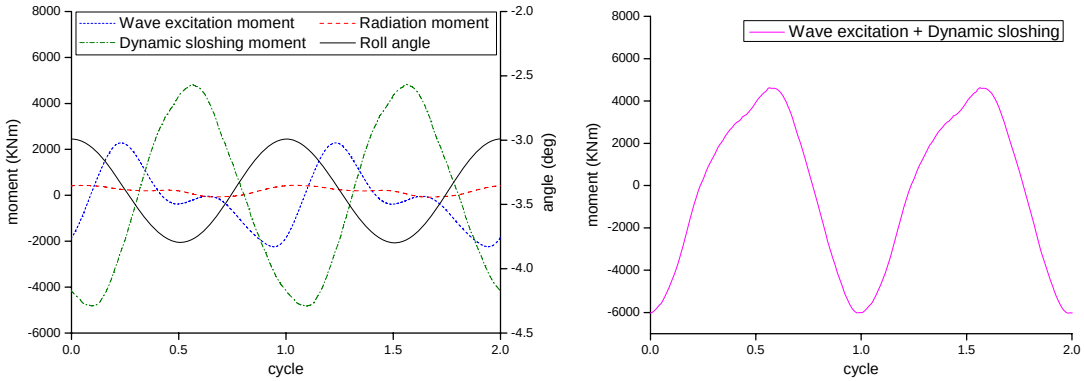

Figure 9.41: The hydrodynamic roll moment acting on an intact ship and the corresponding roll motion (ω=0.9 rad/s).

9.4 Closure

This chapter demonstrates the application of the hybrid method coupling an NS and a seakeeping solver to the damaged ship flooding in waves. The benchmarking study includes the roll decay of a damaged Ro-Ro ferry and the free motion of the ferry in regular beam seas. Information such as flow rate, profile of water surface in the compartment, water impact load on the structure and various components of hydrodynamic force was obtained in the numerical simulation. Compared to the conventional method, the present hybrid method improved the numerical accuracy especially for the flooding case in waves. The peculiar phenomena due to floodwater motion, e.g., the shift of the ship's natural roll frequency, the decrease of the peak response and the presence of a second peak in the RAO curve, were well reproduced by the present method in comparison with the experimental results. In addition to the encouraging numerical accuracy, the computational cost based on our proposed method is affordable even for an ordinary personal computer.

Based on the analysis of present numerical results, several conclusions can be drawn. (i) For a damaged ship, the shift of natural roll frequency is attributed to the presence of water in the compartments but has little relationship with water ingress/egress through the damaged opening. (ii) The decrease of ship response at its natural roll frequency mainly results from internal water sloshing. (iii) The sloshing effects get significant around the natural frequency of internal water motion. The effect of resonant sloshing leads to the presence of a ship's second peak response at higher frequencies. (iv) Around the resonant sloshing frequency, water ingress/egress largely reduced the sloshing motion of internal water. In the range of other frequencies, this effect is relatively small.

The assessment of the two developed solvers (NS solver and hybrid solver) for damaged ship flooding has been completed. In the next chapter, the main findings are

summarised and some recommendations are given for future research.

Chapter 10

Discussion

This research work has been concerned with the development and application of numerical tool for simulating flooding phenomenon of a damaged ship. This chapter summarized the thesis and is divided into two sections. The first section discusses the main contributions to the initial objectives and the second one makes suggestions for future work.

10.1 Summarizations of Present Work

The initially stated main goal of this study, i.e., developing an accurate and efficient numerical tool for the simulation of damaged ship flooding, has been accomplished. First, an FV-discretisation based NS solver was developed to calculate the interactive dynamics of a damaged ship and floodwater, aiming at reproducing the physical flow characteristics in flooding simulation. In this solver, a VOF family scheme, CICSAM, was applied to capture the fluid interface. A combined dynamic mesh strategy based on OST spring analogy method was implemented to handle the mesh update following transient ship motions. Then, a hybrid method, which couples the present NS solver and a seakeeping solver based on potential flow theory, was developed to predict the behaviour of damaged ship in waves, aiming at ensuring high numerical fidelity while reducing computational cost. The dynamics of water flooding and sloshing in the compartments were calculated by the NS solver, whereas the hydrodynamic forces induced by the sea wave on the external hull surface were

calculated using the seakeeping solver. At each time step, the instantaneous ship motion was applied to the excitation of internal water motion; the corresponding loads inside the compartments were added to the total external forces, which were used to update the ship motion.

To illustrate the capability of the developed NS solver in addressing two-phase flow problems, three test cases of dam break, tank sloshing and compartment flooding were solved. For the dam break case, the strong non-linear motion of free surface (e.g., stretching, overturning and breaking) and water impact pressure on the structure obtained by present method, SPH method and experimental measurement were in good agreement. For the non-resonant sloshing case, the computed free surface elevation agreed well with the linear analytical solution and experimental data. Around the resonant sloshing frequency, the linear analytical solution was invalid; whereas the non-linear characteristic of wave profile observed in the numerical simulation coincided with that in the model test. For the compartment flooding case, the amount of water ingress/egress predicted by our numerical method agreed well with the experimental one. It was found that the internal obstruction had significant blockage effect on the propagation of floodwater. The above three validation tests demonstrate that the developed solver is capable to predict complex free surface motion and water impact loads.

To assess its performance in tackling the coupled motion of a damaged ship and floodwater, the present NS solver was applied to simulate flooding of a damaged barge. In the simulation, the geometry of damaged/internal openings and internal layout of compartment were fully considered. The barge motion was included by introducing the proposed dynamic mesh strategy. Generally, the computed motions of floodwater and barge were in good agreement with their experimental counterparts. For the case of fixed barge flooding, the flooding process was drastic during the initial stage. The floodwater inside the compartments exhibited strongly non-linear

and transient behaviour such as ejecting, overturning and breaking. During later stage, the flooding progressed slowly and steadily. The internal water showed quasi-static behaviour. For the case of floating barge flooding, the flooding process was also drastic during the initial stage, and the barge was forced to sink and pitch rapidly. However, the notable transient dynamics of internal water had a limited effect on the roll motion of the barge due to its high initial stability. In the intermediate and final stages, the flooding flow moved smoothly with a flat interface, and the barge became quasi-static. Furthermore, it was found that air compressibility had considerable effect on the flooding process if ventilation level was insufficient. Although the numerical accuracy of the present solver is satisfactory, the high computational cost may prohibit its further application to practical flooding problems.

To demonstrate its computational accuracy and efficiency, the proposed hybrid method coupling the NS and seakeeping solvers was used to predict the seakeeping behaviour of a damaged Ro-Ro ferry. Compared to the conventional method, our method largely improved the numerical accuracy. The roll decay motion and RAOs of the ferry obtained by the present numerical method were very encouraging in comparison with the experimental data. The peculiar phenomena due to floodwater motion, e.g., the shift of the ship's natural roll frequency, the decrease of the peak response and the presence of a second peak in the RAO curve, were well reproduced in the numerical simulation. Information such as flow rate, profile of internal water surface, floodwater impact load and various hydrodynamic components was available in the numerical simulation. This information greatly facilitates analysis of the interactive dynamics of damaged ship, sea wave and floodwater. It was found that (i) the shift of natural roll frequency of a damaged ship was attributed to the presence of water inside the compartments but had little relationship with water ingress/egress through the damaged opening; (ii) internal water sloshing and water ingress/egress weaken the response of the ship at its natural roll frequency; (iii) the effect of resonant sloshing led to the presence of a ship's second peak response at higher

frequencies; (iv) water ingress/egress largely reduced the sloshing effect around the resonant sloshing frequency. In addition, the acceptable computational expense allows practical application of the present method.

In conclusion, the proposed hybrid method provides another optional tool that can be practically used to analyze the ship's behaviour in damaged condition.

10.2 Recommendations for Future Work

The results of conducted benchmarking studies have hinted the research work in future, which can be classified into three categories: further development of the numerical tool, more benchmarking studies and sophisticated applications.

The study of barge flooding has shown that the air in the compartment has significant blockage effect on water ingress if the level of ventilation is insufficient. To account for this effect in the numerical simulation, extending the present NS solver to model air compression is required. Additionally, when the flooding flow becomes chaotic, the CICSAM scheme is found to introduce moderate numerical diffusion that smears the sharp interface. To improve the numerical accuracy of the NS solver, the so-called interface reconstruction technique (Rider and Kothe, 1998) can be employed to capture the free surface.

In the present hybrid method, the calculations of diffraction and radiation forces using the seakeeping solver are based on the intact ship assumption. The error due to this simplification needs to be quantified in future work. To include the effect of damaged opening in these calculations, the non-penetration condition on the damaged part of the hull should be modified by distributing the actual velocity of flow which is obtained by the NS solver. In order to implement this time-dependent boundary condition, an in-house time domain seakeeping solver developed by Kara (2000) will be used to calculate the hydrodynamic forces acting on the external hull

surface, rather than using the present frequency domain solver PROTEUS3. Once the time-dependant properties (velocity, pressure and wave elevation) of the flow field outside the compartments are obtained by the new seakeeping solver, they are provided as boundary condition to the NS solver. Since the flow properties are composed of incident, diffraction and radiation components, perturbation due to non-physical boundary reflection will be eliminated in the CFD simulation. The numerical accuracy of the hybrid method can be further improved.

Besides the numerical accuracy, the efficiency of the hybrid method needs to be further improved. The efficiency of the NS solver is the bottleneck of the entire computational efficiency and can be improved through the following two means. One is to perform the simulation on parallel computers. To this end, the present code needs to be parallelized by using the MPI message-passing library for communication between the processors. The other is to employ a more advanced algorithm to solve the very large system of Eq. (5.14), the solution of which consumes a majority of computational time. The algebraic multigrid method (Stüben, 1999) may be a good choice.

Due to the restriction of computational resources, some factors associated with numerical accuracy were not investigated in the application of present hybrid method. These factors include the computational time step, size of CFD simulation domain and mesh arrangement outside the hull. They need to be verified through more numerical studies. Furthermore, the developed tool needs to be validated against more experimental data.

The development of numerical model relies on the availability and accuracy of experimental measurements. Only more extensive experimental data can reduce the uncertainty in the numerical model and give evidence of phenomenon currently unaccounted for. However, the data of experiments for validation purpose is very

limited. Thus more effort should be also placed into conducting quality experiments in future.

Once the performance of the developed solver is further enhanced, it can be applied to more practical studies such as survivability of damaged ship in irregular waves, damaged ship flooding in restricted water, transient flooding of damaged ship in waves, effect of ship speed on flooding, effect of appendage on damaged ship's behaviour and load prediction for structure analysis of damaged ship.

Chapter 11

Conclusions

On the basis of the work carried out during this research and presented in the foregoing, it is believed that the set aims of the work have been accomplished. In summary, the main conclusions are drawn as follows:

1) An NS solver that combines the VOF method with dynamic mesh techniques has been developed to calculate three-dimensional, time-dependent, incompressible, viscous, two-phase flow with body motion in 6-DOF. Systematic verification and validation studies confirm that the developed solver is capable to account for the full dynamics of floodwater and damaged ship.

2) A hybrid method that couples the NS and seakeeping solvers has also been developed to study damaged ship flooding in waves. The performed benchmarking study demonstrates that the proposed hybrid method can reliably and efficiently to predict the seakeeping behaviour of a damaged ship.

3) To explain the peculiar phenomena observed in the numerical simulation and model test, the interactions between damaged ship, external sea wave and floodwater have been analyzed using the hybrid method. Additionally, the effect of water ingress/egress on the behaviours of the ship and internal water has also been investigated. The main findings indicate that our developed tool can improve understanding of mechanism of damaged ship flooding.

References

Anderson, A., Zheng, X., Cristini, V., 2005. Adaptive unstructured volume remeshing - I: The method. Journal of Computational Physics 208 (2), 616-625.

Ashgriz, N., Poo J. Y., 1991. Flair: flux line-segment model for advection and interface reconstruction. Journal of Computational Physics 93 (2), 449-468.

Azcueta, R., 2001. Computation of turbulent flow around ships and floating bodies. Ph.D. Thesis, Technischen Universität Hamburg-Harburg.

Blom, F. J., 2000. Considerations on the spring analogy. International Journal for Numerical Methods in Fluids 32 (6), 647-668.

Chan, H., Atlar, M., Incecik, A., 2002. Large-amplitude motion responses of a Ro-Ro ship to regular oblique waves in intact and damaged conditions. Journal of Marine Science and Technology 7 (2), 91-99.

Chang, B. C., 1999. On the damage survivability of ro-ro ships investigated by motion simulation in a seaway. Ship Technology Research 46 (4), 192-207.

Chang, B. C., Blume, P., 1998. Survivability of damaged Ro-Ro passenger vessels. Ship Technology Research 45 (3), 105-117.

Cho, S. K., Hong, S. Y., Kim, Y. H., Lee, K. J., 2005. Investigation of dynamic characteristics of the flooding water of the damaged compartment of an ITTC RORO passenger ship. In: Proceedings of the 8th International Ship Stability Workshop, Istanbul.

Cho, S. K., Hong, S. Y., Kim, J., Park, I. R., 2006. The numerical study on the coupled dynamics of ship motion and flooding water. In: Proceedings of the 9th International Conference on Stability of Ships and Ocean Vehicles, Rio de Janeiro, pp. 599-605.

Colagrossi, A., Landrini M., 2003. Numerical simulation of interfacial flows by smoothed particle hydrodynamics. Journal of Computational Physics 191 (2), 448-475.

Cummins, W. E., 1962. The impulse response function and ship motions. Schifftechnik 9 (47), 101-109.

Dand, I., 1989. Hydrodynamic aspects of the sinking of the ferry Herald of Free Enterprise. Transactions of the Royal Institution of Naval Architects 131, 145-165.

Darwish, M. S., Moukalled, F., 2003. TVD schemes for unstructured grids. International Journal of Heat and Mass Transfer 46 (4), 599-611.

Date, A. W., 2005. Solution of transport equations on unstructured meshes with cell-centered colocated variables. Part I: Discretization. International Journal of Heat and Mass Transfer 48 (6), 1117-1127.

de Kat, J. O., Paulling, J. R., 2001. Prediction of extreme motions and capsizing of ships and offshore marine vehicles. In: Proceedings of the 20th International Conference on Offshore Mechanics and Arctic Engineering, Rio de Janeiro, pp. 1-12.

Demirdžić, I., Perić, M., 1988. Space conservation law in finite volume calculations of fluid flow. International Journal for Numerical Methods in Fluids 8 (9), 1037-1050.

Euler, L., 1776. Formulae generales pro translatione quacunque corporum rigidorum. Novi Commentarii academiae scientiarum Petropolitanae 20, 189-207.

Faltinsen, O. M., 1978. A numerical nonlinear method of sloshing in tanks with two-dimensional flow. Journal of Ship Research 22 (3), 193-202.

Fehlberg, E., 1969. Low-order classical Runge-Kutta formulas with step size control and their application to some heat transfer problems. NASA Technical Report, No. 315.

Fekken, G., 2004. Numerical simulation of free-surface flow with moving rigid bodies. Ph.D. Thesis, University of Groningen.

FLUENT 6.3 User's Guide, 2006. Fluent Inc.

GAMBIT 2.3 User's Guide, 2006. Fluent Inc.

Gao, Q., Gao, Z., Vassalos, D., 2010. Numerical study of damage ship flooding. In: Proceedings of the 4th International Maritime Conference on Design for Safety and 3rd Workshop on Risk-Based Approaches in the Marine Industries, Trieste.

Gao, Q., Kara, F., Shigunov, V., Vassalos, D., 2004. Numerical simulation of damage ship flooding. In: Proceeding of the 7th Numerical Towing Tank Symposium, Hamburg.

Gao, Q., Vassalos, D., 2011. Numerical study of the roll decay of intact and damaged ships. In: Proceedings of the 12th International Ship Stability Workshop, Washington D. C., pp. 277-282.

González, V., Talens, M., Riola, J. M., Valle, J., Quesda, T., Espín, M., 2003. Numerical prediction of the dynamic behaviour of a Ro-Ro ship after a hull side damage. In: Proceedings of the 8th International Conference on Stability of Ships and Ocean Vehicles, Madrid, pp. 215-227.

Gueyffier, D., Li, J., Nadim, A., Scardovelli, R., Zaleski, S., 1999. Volume-of-fluid interface tracking with smoothed surface stress methods for three-dimensional flows. Journal of Computational Physics 152 (2), 423-456.

Harlow, F. H., Welch, J. E, 1965. Numerical calculation of time-dependent viscous incompressible flow of fluid with free surface. Physics of Fluids 8 (12), 2182-2189.

Himeno, Y., 1981. Prediction of ship roll damping - state of the art. University of Michigan, Report No. 239.

Hirt, C. W., Nichols, B. D., 1981. Volume of fluid method for the dynamics of free boundaries. Journal of Computational Physics 39 (1), 201-225.

Ibrahim, R. A., 2005. Liquid sloshing dynamics: theory and applications. Cambridge University Press.

Issa, R. I., 1985. Solution of the implicitly discretised fluid flow equations by operator-splitting. Journal of Computational Physics 62 (1), 40-65.

Jasionowski, A., 2001. An integrated approach to damage ship survivability assessment. Ph.D. Thesis, University of Strathclyde.

Kara, F., 2000. Time domain hydrodynamic & hydroelastic analysis of floating bodies with forward speed. Ph.D. Thesis, University of Strathclyde.

Kim, C. H., Chou, F. S., Tien, D., 1980. Motions and hydrodynamic loads of a ship advancing in oblique waves. Transactions of the Society of Naval Architects and Marine Engineers 88, 225-256.

Kim, Y., 2002. A numerical study on sloshing flows coupled with ship motion – the anti-rolling tank problem. Journal of Ship Research 46 (1), 52-62.

Kim, Y., Nam, B. W., Kim, D. W., Kim, Y. S., 2007. Study on coupling effects of ship motion and sloshing. Ocean Engineering 34 (16), 2176-2187.

Kleefsman, K. M. T., Fekken, G., Veldman, A. E. P., Iwanowski, B., Buchner, B., 2005. A volume-of-fluid based simulation method for wave impact problems. Journal of Computational Physics 206 (1), 363-393.

Kong, X., 2009. A numerical study of a damaged ship in beam sea waves. Ph.D. Thesis, Norwegian University of Science and Technology.

Le Touzé, D., Marsh, A., Oger, G., Guilcher, P. M., Khaddaj-Mallat, C., Alessandrini, B., Ferrant, P., 2010. SPH simulation of green water and ship flooding scenarios. Journal of Hydrodynamics, Ser. B 22 (5), 231-236.

Lee, D., Hong, S. Y., Lee, G. J., 2007a. Theoretical and experimental study on dynamic behavior of a damaged ship in waves. Ocean Engineering 34 (1), 21-31.

Lee, D. H., Kim, M. H., Kwon, S. H., Kim, J. W., Lee, Y. B., 2007b. A parametric sensitivity study on LNG tank sloshing loads by numerical simulations. Ocean Engineering 34 (1), 3-9.

Leonard, B. P., 1979. A stable and accurate convective modelling procedure based on quadratic upstream interpolation. Computer Methods in Applied Mechanics and Engineering 19 (1), 59-98.

Leonard, B. P., 1991. The ULTIMATE conservative difference scheme applied to unsteady one-dimensional advection. Computer Methods in Applied Mechanics and Engineering 88 (1), 17-74.

Letizia, L., 1996. Damage survivability of passenger ships in a seaway. Ph.D. Thesis, University of Strathclyde.

Liu, D., Lin, P., 2008. A numerical study of three-dimensional liquid sloshing in tanks. Journal of Computational Physics 227 (8), 3921-3939.

Liu, R., Liu, X., Zhang, L., Wang, Z., 2004. Tracking and reconstruction methods for moving-interfaces. Applied Mathematics and Mechanics 25 (3), 307-321.

Manderbacka, T. L., Matusiak, J. E., 2011. Ship motions caused by time-varying extra mass on board. In: Proceedings of the 12th International Ship Stability

Workshop, Washington D. C., pp. 263-269.

Markou, G. A., Mouroutis, Z. S., Charmpis, D. C., Papadrakakis. M., 2007. The ortho-semi-torsional (OST) spring analogy method for 3D mesh moving boundary problems. Computer Methods in Applied Mechanics and Engineering 196 (4-6), 747-765.

Mei, C. C., Stiassnie, M., Yue, D. K., 2005. Theory and applications of ocean surface waves. World Scientific Publishing.

Monaghan, J. J., 1992. Smoothed particle hydrodynamics. Annual Review of Astronomy and Astrophysics 30, 543-574.

Muzaferija, S., Peric, M., Sames, P., Schelin, T., 1998. A two-fluid Navier-Stokes solver to simulate water entry. In: Proceeding of the 22nd Symposium on Naval Hydrodynamics, Washington D. C., pp. 638-651.

Nabavi, Y., Calisal, S. M., Akinturk, A., Klaptocz, V., 2006. A computational investigation of the three dimensional geometric parameters' effects on the discharge rate of a ship opening. In: Proceedings of the 9th International Conference on Stability of Ships and Ocean Vehicles, Rio de Janeiro, pp. 617-624.

Nielsen, K. B., 2003. Numerical prediction of green water loads on ship. Ph.D. Thesis, Technical University of Denmark.

Noh, W. F., Woodward, P., 1976. SLIC (simple line interface calculation). In: Proceedings of the 5th International Conference on Numerical Methods in Fluid Dynamics, Enschede.

Ogilvie, T. F., 1964. Recent progress towards the understanding and prediction of ship motions. In: Proceedings of 5th Symposium on Naval Hydrodynamics, Bergen, pp. 3-79.

Osher, S., Sethian, J. A., 1988. Fronts propagating with curvature-dependent speed: Algorithms based on Hamilton-Jacobi formulations. Journal of Computational Physics, 79 (1), 12-49.

Palazzi, L., de Kat, J. O., 2004. Model experiments and simulations of a damaged ship with air flow taken into account. Marine Technology 41 (1), 38-44.

Panahi, R., Jahanbakhsh, E., Seif, M. S., 2006. Development of a VoF-fractional step

solver for floating body motion simulation. Applied Ocean Research 28 (3), 171-181.

Papanikolaou, A., Spanos, D., 2004. The 24th ITTC benchmark study on the numerical prediction of damage ship stability in waves - preliminary analysis of results'. In: Proceedings of the 7th International Workshop on Stability and Operational Safety of Ships, Shanghai.

Patankar, S. V., 1980. Numerical heat transfer and fluid flow. Hemisphere.

Patankar, S. V., Spalding, D. B., 1972. A calculation procedure for heat, mass and momentum transfer in three-dimensional parabolic flows. International Journal of Heat and Mass Transfer 15 (10), 1787-1806.

PROTEUS3 user manual, 2001. Ship Stability Research Center, University of Strathclyde.

Rhie, C. W., Chow, W. L., 1983. Numerical study of the turbulent flow past an airfoil with trailing edge separation. American Institute of Aeronautics and Astronautics Journal 21 (11), 1525-1532.

Rider, W. J., Kothe, D. B., 1998. Reconstructing volume tracking. Journal of Computational Physics 141 (2), 112-152.

Rudman, M., 1997. Volume-tracking methods for interfacial flow calculations. International Journal for Numerical Methods in Fluids 24 (7), 671-691.

Ruponen, P., 2006, Model tests for the progressive flooding of a box-shaped barge. Helsinki University of Technology, Report No. M-292.

Ruponen, P., 2007. Progressive flooding of a damaged passenger ship. Ph.D. Thesis, Helsinki University of Technology.

Saad, Y., Schultz, M. H., 1986. GMRES: A generalized minimal residual algorithm for solving nonsymmetric linear systems. SIAM Journal on Scientific and Statistical Computing 7 (3), 856-869.

Saad, Y. 1994. ILUT: A dual threshold incomplete LU factorization. Numerical Linear Algebra with Applications 1 (4), 387-402.

Saad, Y., 2003. Iterative methods for sparse linear systems (second edition). Society for Industrial and Applied Mathematics.

SAFEDOR, 2005-2009. Design, Operation and Regulation for Safety. Integrated project funded by the European Commission, Project No. IP-516278.

Salvesen, N., Tuck, E. O., Faltinsen, O., 1970. Ship motions and sea loads. Transactions of the Society of Naval Architects and Marine Engineers 78, 250-287.

Santos, T. A., Guedes Soares, C., 2008. Study of damaged ship motions taking into account floodwater dynamics. Journal of Marine Science and Technology 13 (3), 291-307.

Santos, T. A., Guedes Soares, C., 2009. Numerical assessment of factors affecting the survivability of damaged ro-ro ships in waves. Ocean Engineering 36 (11), 797-809.

Santos, T. A., Winkle, I. E., Guedes Soares, C., 2002. Time domain modelling of the transient asymmetric flooding of Ro-Ro ships. Ocean Engineering 29 (6), 667-688.

Sen, P., Konstantinidis, C., 1987. A time simulation approach to the assessment of damage survivability of Ro/Ro cargo ships. Transactions of the Society of Naval Architects and Marine Engineers 95, 337-355.

Shen, L., Vassalos, D., 2009. Applications of 3D parallel SPH for sloshing and flooding. In: Proceedings of the 10th International Conference on Stability of Ships and Ocean Vehicles, St. Petersburg, pp. 723-732.

Skaar, D., Vassalos, D., Jasionowski, A., 2006. The use of a meshless CFD method in modelling progressive flooding and damaged stability of ships. In: Proceedings of the 9th International Conference on Stability of Ships and Ocean Vehicles, Rio de Janeiro, pp. 625-632.

Spalding, D. B., 1972. Novel finite difference formulation for differential expressions involving both first and second derivatives. International Journal for Numerical Methods in Engineering 4 (4), 551-559.

Spanos, D., Papanikolaou, A., 2001. On the stability of fishing vessels with trapped water on deck. Ship Technology Research 48 (3), 124-133.

Spouge, J. R., 1986. The technical investigation of the sinking of the Ro-Ro ferry European Gateway. Transactions of the Royal Institution of Naval Architects 128,

49-72.

St. Denis, M., Pierson, W. J., 1953. On the motion of ships in confused seas. Transactions of the Society of Naval Architects and Marine Engineers 61, 280-332.

Steijl, R., Barakos, G., 2008. Sliding mesh algorithm for CFD analysis of helicopter rotor-fuselage aerodynamics. International Journal for Numerical Methods in Fluids 58 (5), 527-549.

Stern, F., Wilson, R. V., Coleman, H. W., Paterson, E. G., 2001. Comprehensive approach to verification and validation of CFD simulations - part 1: methodology and procedures. Journal of Fluids Engineering 123 (4), 793-802.

Strasser, C., 2010. Simulation of progressive flooding of damaged ship by CFD. Ph.D. Thesis, Universities of Glasgow and Strathclyde.

Stüben, K., 1999. Algebraic multigrid (AMG): an introduction with applications. GMD Report.

Tang, H. S., Casey Jones, S., Sotiropoulos, F., 2003. An overset-grid method for 3D unsteady incompressible flows. Journal of Computational Physics 191 (2), 567-600.

TECPLOT 10 User's Manual, 2003. Amtec Engineering Inc.

The Specialist Committee on Prediction of Extreme Ship Motions and Capsizing, 2002. Final report and recommendations to the 23rd ITTC. In: Proceedings of the 23rd International Towing Tank Conference, Rome, pp. 633-649.

The Specialist Committee on Stability in Waves, 2005. Final report and recommendations to the 24th ITTC. In: Proceedings of the 24th International Towing Tank Conference, Edinburgh, pp. 381-391.

The Specialist Committee on Stability in Waves, 2008. Final report and recommendations to the 25th ITTC. In: Proceedings of the 25th International Towing Tank Conference, Fukuoka, pp. 611-624.

Turan, O., Vassalos, D., 1993. Dynamic stability assessment of damaged passenger ships. Transactions of the Royal Institution of Naval Architects 135, 79-104.

Ubbink, O., 1997. Numerical prediction of two fluid systems with sharp interfaces. Ph.D. Thesis, Imperial College of Science, Technology and Medicine.

Ubbink, O., Issa, R. I., 1999. A method for capturing sharp fluid interfaces on arbitrary meshes. Journal of Computational Physics 153 (1), 26-50.

Valanto, P., 2006. Time dependent survival probability of a damaged passenger ship II - Evacuation in seaway and capsizing. HSVA Report, No. 1661, Hamburg.

Van Doormaal, J. P., Raithby, G. D., 1984. Enhancements of the simple method for predicting incompressible fluid flows. Numerical Heat Transfer, Part A: Applications 7 (2), 147-163.

van't Veer, R., de Kat, J. O., Cojeen, P., 2004. Large passenger ship safety: time-to-flood simulations. Marine Technology 41 (2), 82-88.

Vassalos, D., Turan, O., 1994. A realistic approach to assessing the damage survivability of passenger ships. Transactions of the Society of Naval Architects and Marine Engineers 102, 367-394.

Versteeg, H. K., Malalasekera, W., 1995. An introduction to computational fluid dynamics - The finite volume method. Longman Scientific and Technical.

Vredeveldt, A. W., Journée, J. M. J., 1991. Roll motions of ships due to sudden water ingress, calculations and experiments. In: Proceedings of the International Conference on Ro-Ro Safety and Vulnerability the Way Ahead, London.

Wacławczyk, T., Koronowicz, T., 2006. Modeling of the wave breaking with CICSAM and HRIC high-resolution schemes. In: Proceedings of the European Conference on Computational Fluid Dynamics, Delft.

Wacławczyk, T., Koronowicz, T., 2008. Comparison of CICSAM and HRIC high-resolution schemes for interface capturing. Journal of Theoretical and Applied Mechanics 46 (2), 325-345.

Wood, C. D., Hudson, D. A., Tan, M., 2010. CFD simulation of orifice flow for the flooding of damaged ships. In: Proceedings of the 13th Numerical Towing Tank Symposium, Duisburg.

Woodburn, P., Gallagher, P., Letizia, L., 2002. Fundamentals of damage ship survivability. Transactions of the Royal Institution of Naval Architects 144, 143-163.

Xia, J., Jensen, J. J., Pedersen, P. T., 1999. A dynamic model for roll motion of ships due to flooding. Ship Technology Research 46 (4), 208-216.

Xing-Kaeding, Y., 2006. Unified approach to ship seakeeping and maneuvering by a RANSE method. Ph.D. Thesis, Technischen Universität Hamburg-Harburg.

Xue, S. C., Phan-Thien, N., Tanner, R. I., 2002. Upwinding with deferred correction (UDPC): an effective implementation of higher-order convection schemes for implicit finite volume methods. Journal of Non-Newtonian Fluid Mechanics 108 (1), 1-24.

Yang, X., James, A. J., 2006. Analytic relations for reconstructing piecewise linear interfaces in triangular and tetrahedral grids. Journal of Computational Physics 214 (1), 41-54.

Youngs, D. L., 1982. Time-dependent multi-material flow with large fluid distortion. In: Numerical Methods for Fluid Dynamics, edited by Morton, K. W. and Baines M. J., Academic Press, pp. 273-285.

Zhou, Z. Q., de Kat, J. O., Buchner, B., 1999. A nonlinear 3-D approach to simulate green water dynamics on deck. In: Proceedings of the 7th International Conference on Numerical Ship Hydrodynamics, Nantes, pp. 5.1.1-15.

Appendix A

Rigid Body Rotation Based on Euler's Rotation Theorem

A.1 Euler Angles

According to Euler's rotation theorem (Euler, 1776), the orientation of any coordinate system (G, x, y, z) can be achieved by composing three elemental rotations from a given coordinate system (G, X, Y, Z), as shown in Figure A.1.

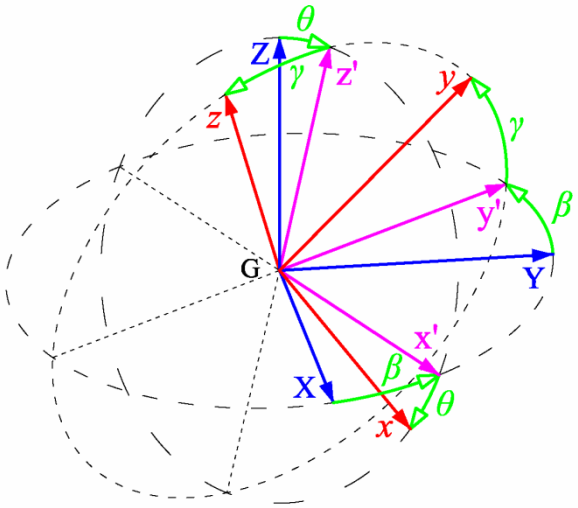

Figure A.1: Definition of Euler angles.

The first rotation is around the vertical axis in the coordinate system (G, X, Y, Z), i.e., around Z-axis, and the rotation angle is denoted as β. The coordinate system has now changed to (G, x', y', Z). The second rotation is around the new transverse axis, i.e. around y'-axis, and the rotation angle is denoted as θ. The coordinate system has

subsequently changed to (G, x, y', z'). The third rotation is around the new longitudinal axis, i.e. around x-axis, and the rotation angle is denoted as γ. The coordinate system has finally changed to (G, x, y, z). The above three angles of rotation (β, θ and γ) are the so-called Euler angles.

A.2 Transformation Matrix

The three elemental rotations mentioned above are separately shown in Figure A.2.

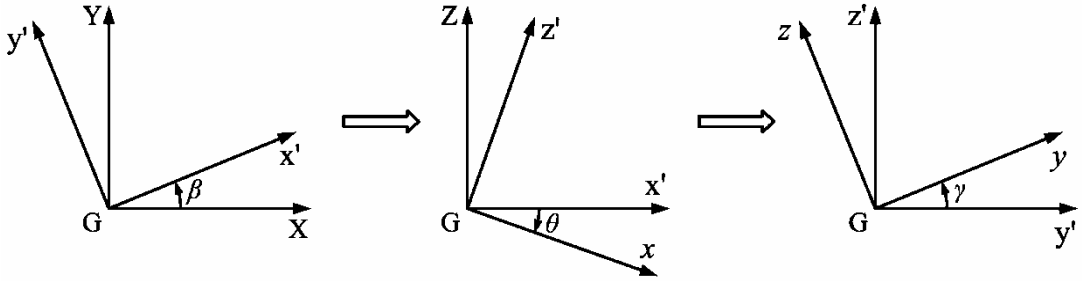

Figure A.2: Decompose of rotation.

The procedure of these rotations is described mathematically as follows:

$$\begin{bmatrix} \mathrm{x}' \\ \mathrm{y}' \\ \mathrm{Z} \end{bmatrix} = [D]_{\beta} \cdot \begin{bmatrix} \mathrm{X} \\ \mathrm{Y} \\ \mathrm{Z} \end{bmatrix} \quad \Rightarrow \quad \begin{bmatrix} x \\ \mathrm{y}' \\ \mathrm{z}' \end{bmatrix} = [D]_{\theta} \cdot \begin{bmatrix} \mathrm{x}' \\ \mathrm{y}' \\ \mathrm{Z} \end{bmatrix} \quad \Rightarrow \quad \begin{bmatrix} x \\ y \\ z \end{bmatrix} = [D]_{\gamma} \cdot \begin{bmatrix} x \\ \mathrm{y}' \\ \mathrm{z}' \end{bmatrix} \tag{A.1}$$

where

$$[D]_{\beta} = \begin{bmatrix} \cos\beta & \sin\beta & 0 \\ -\sin\beta & \cos\beta & 0 \\ 0 & 0 & 1 \end{bmatrix} \tag{A.2}$$

$$[D]_{\theta} = \begin{bmatrix} \cos\theta & 0 & -\sin\theta \\ 0 & 1 & 0 \\ \sin\theta & 0 & \cos\theta \end{bmatrix} \tag{A.3}$$

$$\left[D\right]_{\gamma}=\begin{bmatrix}1 & 0 & 0\\ 0 & \cos\gamma & \sin\gamma\\ 0 & -\sin\gamma & \cos\gamma\end{bmatrix} \tag{A.4}$$

Hence, the relation between coordinate systems (G, x, y, z) and (G, X, Y, Z) reads:

$$\begin{bmatrix}x\\ y\\ z\end{bmatrix}=\left[D\right]_{\gamma}\cdot\left[D\right]_{\theta}\cdot\left[D\right]_{\beta}\cdot\begin{bmatrix}\mathrm{X}\\ \mathrm{Y}\\ \mathrm{Z}\end{bmatrix}=\boldsymbol{T}_{T}^{-1}\cdot\begin{bmatrix}\mathrm{X}\\ \mathrm{Y}\\ \mathrm{Z}\end{bmatrix} \tag{A.5}$$

or

$$\begin{bmatrix}\mathrm{X}\\ \mathrm{Y}\\ \mathrm{Z}\end{bmatrix}=\left[D\right]_{\beta}^{-1}\cdot\left[D\right]_{\theta}^{-1}\cdot\left[D\right]_{\gamma}^{-1}\cdot\begin{bmatrix}x\\ y\\ z\end{bmatrix}=\boldsymbol{T}_{T}\cdot\begin{bmatrix}x\\ y\\ z\end{bmatrix} \tag{A.6}$$

If the BS and GS are designated as coordinate systems (G, x, y, z) and (G, X, Y, Z), respectively, the transformation matrix from the BS to GS has the following expression:

$$\boldsymbol{T}_{T}=\begin{bmatrix}\cos\beta\cos\theta & \cos\beta\sin\theta\sin\gamma-\sin\beta\cos\gamma & \cos\beta\sin\theta\cos\gamma+\sin\beta\sin\gamma\\ \sin\beta\cos\theta & \sin\beta\sin\theta\sin\gamma+\cos\beta\cos\gamma & \sin\beta\sin\theta\cos\gamma-\cos\beta\sin\gamma\\ -\sin\theta & \cos\theta\sin\gamma & \cos\theta\cos\gamma\end{bmatrix} \tag{A.7}$$

The inverse of $\boldsymbol{T}_{T}$, i.e., transformation matrix from the GS to BS, is

$$\boldsymbol{T}_{T}^{-1}=\begin{bmatrix}\cos\beta\cos\theta & \sin\beta\cos\theta & -\sin\theta\\ \cos\beta\sin\theta\sin\gamma-\sin\beta\cos\gamma & \sin\beta\sin\theta\sin\gamma+\cos\beta\cos\gamma & \cos\theta\sin\gamma\\ \cos\beta\sin\theta\cos\gamma+\sin\beta\sin\gamma & \sin\beta\sin\theta\cos\gamma-\cos\beta\sin\gamma & \cos\theta\cos\gamma\end{bmatrix} \tag{A.8}$$

A.3 Time Derivative of Body Orientation

Let vectors $\boldsymbol{i}(t)$, $\boldsymbol{j}(t)$ and $\boldsymbol{k}(t)$ represent the body orientation described in the GS at time level t. Accordingly, the orientation at time level $t+\delta t$ is represented by vectors $\boldsymbol{i}(t+\delta t)$, $\boldsymbol{j}(t+\delta t)$ and $\boldsymbol{k}(t+\delta t)$. Euler angles resulting from the corresponding rotations are denoted as $\delta\beta$, $\delta\theta$ and $\delta\gamma$, respectively. The ratio of change of body orientation and time is defined as:

$$\begin{bmatrix} \dfrac{\delta \boldsymbol{i}}{\delta t} \\ \dfrac{\delta \boldsymbol{j}}{\delta t} \\ \dfrac{\delta \boldsymbol{k}}{\delta t} \end{bmatrix} \equiv \begin{bmatrix} \dfrac{\boldsymbol{i}(t+\delta t)-\boldsymbol{i}(t)}{\delta t} \\ \dfrac{\boldsymbol{j}(t+\delta t)-\boldsymbol{j}(t)}{\delta t} \\ \dfrac{\boldsymbol{k}(t+\delta t)-\boldsymbol{k}(t)}{\delta t} \end{bmatrix} \tag{A.9}$$

Referring to Eq. (A.6), $\boldsymbol{i}(t+\delta t)$, $\boldsymbol{j}(t+\delta t)$ and $\boldsymbol{k}(t+\delta t)$ can be expressed as:

$$\begin{bmatrix} \boldsymbol{i}(t+\delta t) \\ \boldsymbol{j}(t+\delta t) \\ \boldsymbol{k}(t+\delta t) \end{bmatrix} = \left[\boldsymbol{T}_T\right]_{\delta\beta,\delta\theta,\delta\gamma} \cdot \begin{bmatrix} \boldsymbol{i}(t) \\ \boldsymbol{j}(t) \\ \boldsymbol{k}(t) \end{bmatrix} \tag{A.10}$$

Substituting Eq. (A.10) into Eq. (A.9) gives the following equation:

$$\begin{bmatrix} \dfrac{\delta \boldsymbol{i}}{\delta t} \\ \dfrac{\delta \boldsymbol{j}}{\delta t} \\ \dfrac{\delta \boldsymbol{k}}{\delta t} \end{bmatrix} = \frac{\left[\boldsymbol{T}_T\right]_{\delta\beta,\delta\theta,\delta\gamma} - I}{\delta t} \cdot \begin{bmatrix} \boldsymbol{i}(t) \\ \boldsymbol{j}(t) \\ \boldsymbol{k}(t) \end{bmatrix} \tag{A.11}$$

As δt approaches to zero, $\delta\beta$, $\delta\theta$ and $\delta\gamma$ approach to zero; $\sin(\delta\beta)=\delta\beta$; $\sin(\delta\theta)=\delta\theta$; $\sin(\delta\gamma)=\delta\gamma$; and $\cos(\delta\beta)=\cos(\delta\theta)=\cos(\delta\gamma)=1$. The left- and right-hand sides of Eq. (A.11) are subsequently transformed into the following two expressions, respectively.

$$\lim_{\delta t\to 0}\begin{bmatrix}\dfrac{\delta \boldsymbol{i}}{\delta t}\\ \dfrac{\delta \boldsymbol{j}}{\delta t}\\ \dfrac{\delta \boldsymbol{k}}{\delta t}\end{bmatrix}=\begin{bmatrix}\dfrac{d}{dt}\boldsymbol{i}\\ \dfrac{d}{dt}\boldsymbol{j}\\ \dfrac{d}{dt}\boldsymbol{k}\end{bmatrix} \tag{A.12}$$

$$\lim_{\delta t\to 0}\frac{[\boldsymbol{T}_T]_{\delta\beta,\delta\theta,\delta\gamma}-I}{\delta t}=\lim_{\delta t\to 0}\begin{bmatrix}0 & \dfrac{-\delta\beta}{\delta t} & \dfrac{\delta\theta}{\delta t}\\ \dfrac{\delta\beta}{\delta t} & 0 & \dfrac{-\delta\gamma}{\delta t}\\ \dfrac{-\delta\theta}{\delta t} & \dfrac{\delta\gamma}{\delta t} & 0\end{bmatrix}=\begin{bmatrix}0 & -\dfrac{d\beta}{dt} & \dfrac{d\theta}{dt}\\ \dfrac{d\beta}{dt} & 0 & -\dfrac{d\gamma}{dt}\\ -\dfrac{d\theta}{dt} & \dfrac{d\gamma}{dt} & 0\end{bmatrix} \tag{A.13}$$

Then Eq. (A.11) can be rewritten as:

$$\begin{bmatrix}\dfrac{d}{dt}\boldsymbol{i}\\ \dfrac{d}{dt}\boldsymbol{j}\\ \dfrac{d}{dt}\boldsymbol{k}\end{bmatrix}=\begin{bmatrix}0 & -\dfrac{d\beta}{dt} & \dfrac{d\theta}{dt}\\ \dfrac{d\beta}{dt} & 0 & -\dfrac{d\gamma}{dt}\\ -\dfrac{d\theta}{dt} & \dfrac{d\gamma}{dt} & 0\end{bmatrix}\cdot\begin{bmatrix}\boldsymbol{i}\\ \boldsymbol{j}\\ \boldsymbol{k}\end{bmatrix} \tag{A.14}$$

Since $d\gamma/dt=\Omega_X$, $d\theta/dt=\Omega_Y$ and $d\beta/dt=\Omega_Z$, where Ω_X, Ω_Y and Ω_Z are the components of angular velocity of the body. Then Eq. (A.14) is further rewritten as:

$$\begin{bmatrix}\dfrac{d}{dt}\boldsymbol{i}\\ \dfrac{d}{dt}\boldsymbol{j}\\ \dfrac{d}{dt}\boldsymbol{k}\end{bmatrix}=\begin{bmatrix}0 & -\Omega_Z & \Omega_Y\\ \Omega_Z & 0 & -\Omega_X\\ -\Omega_Y & \Omega_X & 0\end{bmatrix}\cdot\begin{bmatrix}\boldsymbol{i}\\ \boldsymbol{j}\\ \boldsymbol{k}\end{bmatrix} \tag{A.15}$$

Eq. (A.15) describes the relation between the body orientation and its angular velocity of rotation. It can be either expressed in the following forms:

$$\frac{d}{dt}\boldsymbol{i} = \boldsymbol{\Omega} \times \boldsymbol{i} \tag{A.16}$$

$$\frac{d}{dt}\boldsymbol{j} = \boldsymbol{\Omega} \times \boldsymbol{j} \tag{A.17}$$

$$\frac{d}{dt}\boldsymbol{k} = \boldsymbol{\Omega} \times \boldsymbol{k} \tag{A.18}$$

A.4 Body Rotation Angles

In the area of ocean engineering, the orientation of a body is usually represented by the angles of roll, pitch and yaw, which are defined as follows:

- **Roll angle** is the angle between the body transverse axis and the horizontal plane.
- **Pitch angle** is the angle between the body longitudinal axis and the horizontal plane.
- **Yaw angle** is the angle of rotation around the axis perpendicular to the horizontal plane.

We define the coordinate system (G, x, y, z) mentioned in Section A.1 to be the BS and XY-plane to be horizontal. Consequently, the longitudinal and transverse axes of a body are respectively equivalent to *x*- and *y*-axes shown in Figure A.1. Because x'- and y'-axes are the projections of *x*- and *y*-axes onto the XY-plane, respectively. According to the definitions of Euler angles and body rotation angles, the Euler angles describe the body orientation. Herein, the angles of roll, pitch and yaw are respectively designated as Euler angles γ, θ and β, which can be expressed as:

$$\gamma = \arccos\left(\frac{\overrightarrow{\mathrm{Gy'}}}{\left|\overrightarrow{\mathrm{Gy'}}\right|} \cdot \frac{\overrightarrow{\mathrm{G}y}}{\left|\overrightarrow{\mathrm{G}y}\right|} \right) \tag{A.19}$$

$$\theta = \arccos\left(\frac{\overrightarrow{\mathrm{Gx'}}}{\left|\overrightarrow{\mathrm{Gx'}}\right|} \cdot \frac{\overrightarrow{\mathrm{G}x}}{\left|\overrightarrow{\mathrm{G}x}\right|}\right) \tag{A.20}$$

$$\beta = \arccos\left(\frac{\overrightarrow{\mathrm{GX}}}{\left|\overrightarrow{\mathrm{GX}}\right|} \cdot \frac{\overrightarrow{\mathrm{Gx'}}}{\left|\overrightarrow{\mathrm{Gx'}}\right|}\right) \tag{A.21}$$

where

$$\overrightarrow{\mathrm{Gx'}} = \overrightarrow{\mathrm{G}x} - \left(\overrightarrow{\mathrm{G}x} \cdot \overrightarrow{\mathrm{GZ}}\right)\overrightarrow{\mathrm{GZ}} \tag{A.22}$$

$$\overrightarrow{\mathrm{Gy'}} = \overrightarrow{\mathrm{GZ}} \times \overrightarrow{\mathrm{Gx'}} \tag{A.23}$$

Appendix B

Spatial Interpolation Schemes

Figure B.1 shows two arbitrary CVs Q and H which are connected with face F. Points q, h and f are the centres of CV Q, CV H and face F, respectively. Points q' and h' are the projections of q and h onto the face normal vector $\boldsymbol{n}$ passing through point f, respectively. For the spatial discretisation conducted on a collocated grid system, all the flow properties (χ) are defined at the centre of the CV. Thus, the values at f need to be evaluated by interpolating the values at q or h. This appendix briefly describes the interpolation schemes adopted in our study.

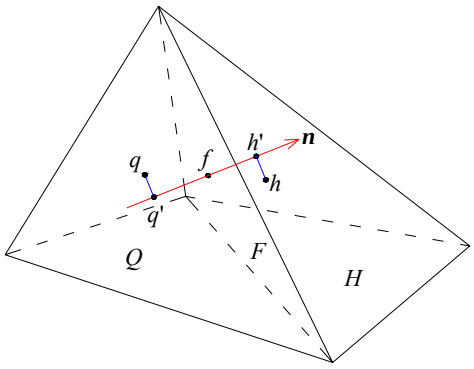

Figure B.1: Control volumes with arbitrary shape.

B.1 Upwind Differencing Scheme

For a strongly convective flow, the value of flow property at CV face should receive much stronger influencing from the upstream CV than that from the downstream CV. The upwind differencing (UD) scheme considers the flow direction when

determining the value at a CV face: the value of χ at a cell face is taken to be equal to the value at the upstream node, i.e.,

$$\chi_f = \begin{cases} \chi_q, & \text{when the flow is from } q \text{ to } h \\ \chi_h, & \text{when the flow is from } h \text{ to } q \end{cases} \tag{B.1}$$

The Taylor serious truncation error of the above UD scheme is first order. The scheme is unconditionally stable for iterative solution when it is used to calculate the face velocity ($\boldsymbol{u}_f$) in the convective term of Eq. (5.11). No oscillations or wiggles occur in the solution. A major drawback of this scheme is that it produces false diffusion when the flow is not aligned with the grid lines. However, refinement of the grid can, in principle, overcome this problem.

B.2 Central Differencing Scheme

The value of χ at a CV face can be expressed by the following central differencing (CD) scheme:

$$\chi_f = \frac{\left|\overrightarrow{hf}\right| \chi_q + \left|\overrightarrow{qf}\right| \chi_h}{\left|\overrightarrow{qf}\right| + \left|\overrightarrow{hf}\right|} \tag{B.2}$$

The Taylor serious truncation error of the CD scheme is second order. For the calculation of $\boldsymbol{u}_f$ in the convective term of Eq. (5.11), this scheme will be stable and accurate only if $Pe<2$; otherwise it produces non-physical solution that appears to wiggle about the exact solution. Here Pe is the Peclet number and is defined as follows:

$$Pe = \frac{\rho_f E_f \Big/ \left|\boldsymbol{A}_f\right|}{\mu_f \Big/ \left|\overrightarrow{q'h'}\right|} \tag{B.3}$$

The definitions of symbols in Eq. (B.3) are identical to those in Eq. (5.11). The

numerator and denominator of *Pe* represent the convective mass flux per unit area and diffusion conductance at the CV face, respectively, which indicates that the value of *Pe* reflects the intensity proportion of convection and diffusion to a certain extent.

B.3 Hybrid Differencing Scheme

Spalding (1972) proposed a hybrid differencing scheme to calculate the value of χ at a CV face. The scheme switches between the aforementioned CD and first-order UD schemes according to the value of *Pe*:

$$\chi_f = \begin{cases} \text{UD scheme (Eq. (B.1)), for } |Pe| \geq 2 \\ \text{CD scheme (Eq. (B.2)), for } |Pe| < 2 \end{cases} \tag{B.4}$$

Because the hybrid scheme makes the best of the advantages of UD and CD schemes, so it is highly computationally stable and can always obtain physically acceptable solution. Moreover, it is easy to implement for arbitrary meshes. In this study, the hybrid scheme is used to calculate $\boldsymbol{u}_f$ in the convective term of Eq. (5.11).

B.4 Calculation of Diffusive Term

The diffusive term in Eq. (5.11) is transformed to the following form:

$$\mu_f \boldsymbol{A}_f \cdot (\nabla \chi)_f = \mu_f |\boldsymbol{A}_f| \left| \frac{\partial \chi}{\partial n} \right|_f \tag{B.5}$$

The above normal derivative at point *f* of CV face can be approximated as:

$$\left| \frac{\partial \chi}{\partial n} \right|_f = \frac{\chi_{h'} - \chi_{q'}}{\left| \overrightarrow{q'h'} \right|} \tag{B.6}$$

where $\chi_{q'}$ and $\chi_{h'}$ denote the values of χ at points *q*' and *h*', respectively, and they are

calculated as follows:

$$\chi_{q'} = \chi_q + \overrightarrow{qq'} \cdot \nabla \chi_q \tag{B.7}$$

$$\chi_{h'} = \chi_h + \overrightarrow{hh'} \cdot \nabla \chi_h \tag{B.8}$$

Substituting Eqs. (B.6) to (B.8) into Eq. (B.5), the diffusive term in Eq. (5.11) is finally written as:

$$\mu_f \boldsymbol{A}_f \cdot (\nabla \chi)_f = \mu_f \left| \boldsymbol{A}_f \right| \frac{\chi_h - \chi_q}{\left| \overrightarrow{q'h'} \right|} + \mu_f \left| \boldsymbol{A}_f \right| \frac{\overrightarrow{hh'} \cdot \nabla \chi_h - \overrightarrow{qq'} \cdot \nabla \chi_q}{\left| \overrightarrow{q'h'} \right|} \tag{B.9}$$

The gradient of χ at point q is estimated as:

$$\nabla \chi_q = \frac{1}{V_q} \sum_{i=1}^{k} \boldsymbol{A}_{f_i} \chi_{f_i} \tag{B.10}$$

where the symbol definitions are identical to those in Eq. (5.11); χ_f is calculated by using the CD scheme (Eq. (B.2)). $\nabla \chi_h$ has the similar form of Eq. (B.10). $\nabla \chi_q$ and $\nabla \chi_h$ in Eq. (B.9) are treated explicitly based on the values obtained at the previous iteration. This treatment never brings any influence on the final solutions when using the SIMPLE algorithm for pressure-velocity coupling.

B.5 Calculation of Face Pressure

If the density ratio of two fluids is large (e.g., water and air), using the common linear interpolations for calculation of CV face pressure (P_f) results in severe oscillations in velocity field. Panahi et al. (2006) proposed a piecewise linear interpolation, the weighting factor of which accounts for the influence of fluid density, to better estimate the face pressure. The interpolation form is given as

follows:

$$P_f = \frac{\rho_h \left|\overrightarrow{hf}\right| P_q + \rho_q \left|\overrightarrow{qf}\right| P_h}{\rho_q \left|\overrightarrow{qf}\right| + \rho_h \left|\overrightarrow{hf}\right|} \tag{B.11}$$

In our study, Eq. (B.11) is used to calculate P_f which appears in Eq. (5.11) and the evaluation of pressure gradient.

B.6 Momentum Interpolation Method

In the incompressible flow calculations, to couple the pressure field properly with the velocity field, the continuity equation (Eq. (5.12)) is commonly transformed into a pressure-correction equation according to the SIMPLE-type algorithms, e.g., SIMPLE (Patankar and Spalding, 1972), SIMPLER (Patankar, 1980), SIMPLEC (Van Doormaal and Raithby, 1984) and PISO (Issa, 1985). For collocated variable arrangement, special care needs to be taken in the prediction of $\boldsymbol{u}_f$ in Eq. (5.12) to avoid the decoupling of the velocity and pressure. The momentum interpolation method proposed by Rhie and Chow (1983) is adopted in the present study to calculate this face velocity. The momentum equation (5.11) can be rewritten in the form of Eq. (5.14):

$$a_q \boldsymbol{u}_q^{t_{n+1}} + \sum_{nb=1}^{NK} a_{nb} \boldsymbol{u}_{nb}^{t_{n+1}} = b_{\boldsymbol{u}_q} - \left(\nabla P\right)_q^{t_{n+1}} \tag{B.12}$$

The contribution of pressure is isolated from the source term and still treated explicitly. Then the velocity at a CV centre is expressed as:

$$\boldsymbol{u}_q^{t_{n+1}} = \frac{\boldsymbol{D}(\boldsymbol{u})_q}{a_q} - \frac{1}{a_q}\left(\nabla P\right)_q^{t_{n+1}} \tag{B.13}$$

where

$$\boldsymbol{D}(\boldsymbol{u})_q = -\sum_{nb=1}^{NK} a_{nb}\boldsymbol{u}_{nb}^{t_{n+1}} + b_{\boldsymbol{u}_q} \tag{B.14}$$

Referring to Eq. (B.13), the value of the velocity at a CV face can be therefore expressed as follows:

$$\boldsymbol{u}_f^{t_{n+1}} = \left(\frac{\boldsymbol{D}(\boldsymbol{u})_q}{a_q}\right)_f - \left(\frac{1}{a_q}\right)_f \left(\nabla P\right)_f^{t_{n+1}} \tag{B.15}$$

On the right-hand side of Eq. (B.15), the face values other than the pressure gradient are calculated by using the CD scheme, i.e.,

$$\left(\frac{\boldsymbol{D}(\boldsymbol{u})_q}{a_q}\right)_f = \frac{\left|\overrightarrow{hf}\right|\left(\frac{\boldsymbol{D}(\boldsymbol{u})_q}{a_q}\right)_q + \left|\overrightarrow{qf}\right|\left(\frac{\boldsymbol{D}(\boldsymbol{u})_q}{a_q}\right)_h}{\left|\overrightarrow{qf}\right| + \left|\overrightarrow{hf}\right|} \tag{B.16}$$

$$\left(\frac{1}{a_q}\right)_f = \frac{\left|\overrightarrow{hf}\right|\left(\frac{1}{a_q}\right)_q + \left|\overrightarrow{qf}\right|\left(\frac{1}{a_q}\right)_h}{\left|\overrightarrow{qf}\right| + \left|\overrightarrow{hf}\right|} \tag{B.17}$$

Substituting Eq. (B.15) into Eq. (5.12), the following equation holds:

$$\sum_{i=1}^{k}\left(\frac{1}{a_q}\right)_{f_i} \boldsymbol{A}_{f_i} \cdot \left(\nabla P\right)_{f_i}^{t_{n+1}} = \sum_{i=1}^{k} \boldsymbol{A}_{f_i} \cdot \left(\frac{\boldsymbol{D}(\boldsymbol{u})_q}{a_q}\right)_{f_i} \tag{B.18}$$

Similarly to the diffusive term of momentum equations (see Eq. (B.9)), the term in Eq. (B.18) containing the pressure gradient over the faces is calculated directly from the pressure values at the CV centres sharing the face:

$$\left(\frac{1}{a_q}\right)_f \boldsymbol{A}_f \cdot \left(\nabla P\right)_f = \left(\frac{1}{a_q}\right)_f \left|\boldsymbol{A}_f\right| \frac{P_h - P_q}{\left|\overrightarrow{q'h'}\right|} + \left(\frac{1}{a_q}\right)_f \left|\boldsymbol{A}_f\right| \frac{\overrightarrow{hh'} \cdot \nabla P_h - \overrightarrow{qq'} \cdot \nabla P_q}{\left|\overrightarrow{q'h'}\right|} \tag{B.19}$$

∇P_q and ∇P_h in Eq. (B.19) are treated explicitly and evaluated by using Eq. (B.10) in which the corresponding face value P_f is obtained with Eq. (B.11). Substituting Eq. (B.19) into Eq. (B.18) gives the following algebraic equation in terms of the pressure values at CV centres:

$$a_q P_q^{t_{n+1}} + \sum_{nb=1}^{NK} a_{nb} P_{nb}^{t_{n+1}} = b_{P_q} \tag{B.20}$$

Eq. (B.20) is eventually transformed into a pressure-correction equation following the SIMPLE algorithm. The transformation procedure is not amplified herein and can be referred to the literature (Patankar and Spalding, 1972). Furthermore, Eq. (B.15) is also employed for the calculation of $\boldsymbol{u}_f$ in the volumetric flux (E) defined in Eq. (5.11).

B.7 CICSAM Scheme

When solving the transport equation for the volume fraction (Eq. (5.3)), a critical problem arises: how to advect the interface without being diffused, dispersed, or wrinkled. A kind of method to overcome this problem is using the so-called interface reconstruction techniques with Eulerian or Lagrangian advection of the reconstructed interface, such as the SLIC method (Noh and Woodward, 1976), donor-acceptor method (Hirt and Nichols, 1981), PLIC method (Youngs, 1982) and FLAIR method (Ashgriz and Poo, 1991), etc. An extensive review of this type of methods can be found in the literature (Rider and Kothe, 1998). Methods based on these ideas can give good approximation of the interface shape and allow for proper calculation of the flux through the CV faces. However, the shape of CV is implicitly included in the reconstruction of the interface. Consequently, implementations of these methods on a simple-shape hexahedron mesh even need a substantial number of numerical operations (Gueyffier et al., 1999). Their extensions to meshes with arbitrary CV

shapes further increase the computational effort (Yang and James, 2006).

An alternative approach to the problem of preserving interface resolution is to solve the discretized transport equation for the volume fraction (e.g., Eq. (5.13)) with a high resolution differencing scheme, such as the CICSAM scheme (Ubbink, 1997), FCT scheme (Rudman, 1997), HRIC scheme (Muzaferija et al., 1998) and TVD-based scheme (Darwish and Moukalled, 2003). Among these schemes, the CICSAM scheme outperforms the others and its performance is even close to Youngs's PLIC method, as show in the studies of Ubbink and Issa (1999), Liu et al. (2004), Wacławczyk and Koronowicz (2006, 2008). Moreover, the CICSAM scheme can be easily implemented on unstructured meshes where it likewise performs well. Therefore, the CICSAM scheme is employ to calculate the face volume fraction (α_f) in our study.

The CICSAM scheme is derived from the normalized variable diagram (NVD) concept (Leonard, 1991). Figure B.2 shows three consecutive CVs based on structured mesh arrangement. Points *U*, *D* and *A* denotes the centres of upwind, donor and acceptor CVs, respectively. Point *f* denotes the centre of CV face which connects the donor and acceptor CVs.

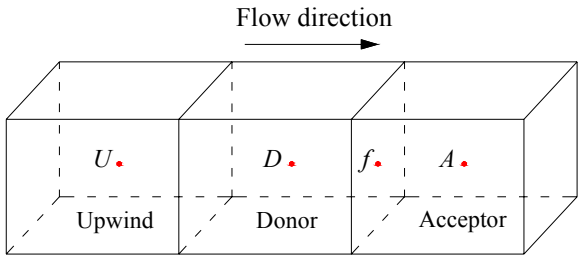

Figure B.2: Control volumes based on structured mesh arrangement.

The normalised variable for volume fraction α_D and α_f are defined as:

$$\tilde{\alpha}_D = \frac{\alpha_D - \alpha_U}{\alpha_A - \alpha_U} \tag{B.21}$$

$$\tilde{\alpha}_f = \frac{\alpha_f - \alpha_U}{\alpha_A - \alpha_U} \tag{B.22}$$

Following some algebraic manipulations of Eqs. (B.21) and (B.22), the expression for the face value of volume fraction reads:

$$\alpha_f = \left(1 - \kappa_f\right)\alpha_D + \kappa_f \alpha_A \tag{B.23}$$

where

$$\kappa_f = \frac{\tilde{\alpha}_f - \tilde{\alpha}_D}{1 - \tilde{\alpha}_D} \tag{B.24}$$

The only unknown variable in the above weighting factor κ_f is $\tilde{\alpha}_f$, which is calculated by the following blended differencing scheme:

$$\tilde{\alpha}_f = \varpi_f \tilde{\alpha}_{f_{CBC}} + \left(1 - \varpi_f\right)\tilde{\alpha}_{f_{UQ}} \tag{B.25}$$

$$\tilde{\alpha}_{f_{CBC}} = \begin{cases} \min\left(1,\ \dfrac{\tilde{\alpha}_D}{Co_D}\right), & \text{for } 0 \le \tilde{\alpha}_D \le 1 \\ \tilde{\alpha}_D, & \text{for } \tilde{\alpha}_D < 0,\ \tilde{\alpha}_D > 1 \end{cases} \tag{B.26}$$

$$\tilde{\alpha}_{f_{UQ}} = \begin{cases} \min\left[\tilde{\alpha}_{f_{CBC}},\ \dfrac{8Co_D\tilde{\alpha}_D + \left(1 - Co_D\right)\left(6\tilde{\alpha}_D + 3\right)}{8}\right], & \text{for } 0 \le \tilde{\alpha}_D \le 1 \\ \tilde{\alpha}_D, & \text{for } \tilde{\alpha}_D < 0,\ \tilde{\alpha}_D > 1 \end{cases} \tag{B.27}$$

where $\tilde{\alpha}_{f_{CBC}}$ and $\tilde{\alpha}_{f_{UQ}}$ are the HYPER-C and ULTIMATE-QUICKEST schemes (Leonard, 1991), respectively; Co_D is the cell Courant number of the donor CV and is already defined in Eq. (5.15). The weighting factor ϖ_f in Eq. (B.25) is based on the angle ψ_f between $\nabla\alpha_D$, the vector normal to the interface, and $\overrightarrow{DA}$, the vector connecting the centres of the donor and acceptor CVs, i.e.,

$$\varpi_f = \min\left\{\frac{1+\cos\left(2\psi_f\right)}{2},\ 1\right\} \tag{B.28}$$

$$\psi_f = \arccos\left|\frac{\nabla\alpha_D}{\left|\nabla\alpha_D\right|}\cdot\frac{\overrightarrow{DA}}{\left|\overrightarrow{DA}\right|}\right| \tag{B.29}$$

$\nabla\alpha_D$ in Eq. (B.29) is treated explicitly and evaluated by using Eq. (B.10) in which the corresponding face value α_f is obtained with Eq. (B.23).

Note that the upwind value α_U is not readily available on arbitrary meshes and can be estimated by using the following formulation:

$$\alpha_U = \min\left\{\max\left[\alpha_A - 2\left(\nabla\alpha_D\right)\cdot\overrightarrow{DA},\ \alpha_{\min}\right],\ \alpha_{\max}\right\} \tag{B.30}$$

where $\alpha_{\min}$ and $\alpha_{\max}$ are the lower and upper bounds of α, respectively.

Appendix C

Relation between Coefficients in Equations of Time and Frequency Domains

Let us consider a ship oscillating under a sinusoidal excitation force. If the dynamic system is wholly linear, the oscillatory motion of the ship will be sinusoidal. For a given excitation force (F_{ex}) with fixed frequency (ω), the equation for the ship motion can be written in the following form (Salvesen et al., 1970):

$$\sum_{k=1}^{6}\left\{\left[\Lambda_{jk}+A_{jk}\left(\omega\right)\right]\ddot{x}_{G,k}+B_{jk}\left(\omega\right)\dot{x}_{G,k}+C_{jk}x_{G,k}\right\}=F_{\text{ex},j},\quad j=1,2,\ldots,6 \tag{C.1}$$

where Λ is the generalized mass matrix for the ship; A and B are the frequency-dependent added mass and damping coefficient, respectively; C is the restoring coefficients; and x_G is the linear or angular displacement of the ship.

Although Eq. (C.1) has the appearance of a differential equation, it is not a real differential equation for the ship motion. In fact, x_G and F_{ex} can be expressed as follows:

$$x_{G,j}=\text{Re}\left(\bar{x}_{G,J}e^{i\omega t}\right),\quad j=1,2,\ldots,6 \tag{C.2}$$

$$F_{\text{ex},j}=\text{Re}\left(\bar{F}_{\text{ex},j}e^{i\omega t}\right),\quad j=1,2,\ldots,6 \tag{C.3}$$

where $\bar{x}_G$ and $\bar{F}_{\text{ex}}$ are, respectively, the complex amplitude of ship motion and

excitation force, in which the phase angles for different modes are included. Substituting Eqs. (C.2) and (C.3) into Eq. (C.1) gives the following equation:

$$\sum_{k=1}^{6}\left\{-\omega^2\left[\Lambda_{jk}+A_{jk}\left(\omega\right)\right]+i\omega B_{jk}\left(\omega\right)+C_{jk}\right\}\overline{x}_{G,k}=\overline{F}_{\mathrm{ex},j},\quad j=1,2,\ldots,6 \tag{C.4}$$

It is clear that Eq. (C.4) is a set of algebraic equations for the solution of complex amplitude of the ship motion at a fixed frequency. Therefore, Eq. (C.1) just describes the response of ship motion to the excitation force associated with one specific frequency and amplitude; it does not reflect the relation between the instantaneous ship motion and forces acting on the ship. Eqs. (C.1) or (C.4) is customarily referred to as ship motion equation in the frequency domain.

Actually, the radiation wave generated by a ship at time t will persist, in principle, for an infinite time thereafter. In other words, the radiation force is time-dependant on the previous history of the fluid motion. Consequently, these "memory effects" should be implied in the ship motion equation. Cummins (1962) employed the impulse response concept, in which the motion history of a ship is considered as the composition of a series of instantaneous impulse motions, to deduce the ship motion equation in the time domain:

$$\sum_{k=1}^{6}\left[\left(\Lambda_{jk}+A_{jk}^{*}\right)\ddot{x}_{G,k}+\int_{-\infty}^{t}K_{jk}\left(t-\tau\right)\dot{x}_{G,k}\left(\tau\right)d\tau+C_{jk}^{*}x_{G,k}\right]=F_{\mathrm{ex},j},\ j=1,2,\ldots,6 \tag{C.5}$$

where A^* is the added mass which is only associated with the ship geometry while depending neither on the frequency nor on the time; $K(t)$ is the so-called retardation function which accounts for the "memory effects" of fluid motion; and C^* is the restoring coefficients.

To obtained A^* and $K(t)$ directly from their definition is far from easy. Alternatively,

Ogilvie (1964) has shown how these coefficient and function are related to the frequency-dependent added mass $A(\omega)$ and damping coefficients $B(\omega)$ appearing in Eq. (C.1). The time domain equation (C.5) can describe motions of any kind, also harmonic motions. Let the ship perform a simple harmonic oscillation:

$$x_{G,j} = \cos(\omega t), \quad j = 1,2,\ldots,6 \tag{C.6}$$

Substituting Eq. (C.6) into Eq. (C.5) and replacing τ by $t-\tau$ in the integral gives:

$$\begin{aligned} \sum_{k=1}^{6}\Big[& -\omega^2\left(\Lambda_{jk} + A_{jk}^*\right)\cos(\omega t) + \omega\int_0^\infty K_{jk}(\tau)\sin(\omega t - \omega\tau)\,d\tau \\ & + C_{jk}^*\cos(\omega t)\Big] = F_{\mathrm{ex},j}, \qquad j = 1,2,\ldots,6 \end{aligned} \tag{C.7}$$

Eq. (C.7) can be rearranged as:

$$\begin{aligned} \sum_{k=1}^{6}\Big\{ & -\omega^2\left[\left(\Lambda_{jk} + A_{jk}^*\right) - \frac{1}{\omega}\int_0^\infty K_{jk}(\tau)\sin(\omega\tau)\,d\tau\right]\cos(\omega t) \\ & - \omega\int_0^\infty K_{jk}(\tau)\cos(\omega\tau)\,d\tau\sin(\omega t) \\ & + C_{jk}^*\cos(\omega t)\Big\} = F_{\mathrm{ex},j}, \qquad j = 1,2,\ldots,6 \end{aligned} \tag{C.8}$$

On the other hand, substituting Eq. (C.6) into Eq. (C.1) gives:

$$\begin{aligned} \sum_{k=1}^{6}\Big\{ & -\omega^2\left[\Lambda_{jk} + A_{jk}(\omega)\right]\cos(\omega t) \\ & - \omega B_{jk}(\omega)\sin(\omega t) \\ & + C_{jk}\cos(\omega t)\Big\} = F_{\mathrm{ex},j}, \qquad j = 1,2,\ldots,6 \end{aligned} \tag{C.9}$$

By comparing the terms in Eqs. (C.8) and (C.9), the following relations hold:

$$A_{jk}^* = A_{jk}(\omega) + \frac{1}{\omega}\int_0^\infty K_{jk}(\tau)\sin(\omega\tau)\,d\tau \tag{C.10}$$

$$\int_0^\infty K_{jk}(\tau)\cos(\omega\tau)\,d\tau = B_{jk}(\omega) \tag{C.11}$$

$$C_{jk}^* = C_{jk} \tag{C.12}$$

Eq. (C.10) must be valid for all ω, and hence the expression for A^* is obtained by choosing $\omega=\infty$:

$$A_{jk}^* = A_{jk}(\infty) \tag{C.13}$$

Function $K(t)$ is obtained by taking the inverse Fourier transform of Eq. (C.11):

$$K_{jk}(t) = \frac{2}{\pi}\int_0^\infty B_{jk}(\omega)\cos(\omega t)\,d\omega \tag{C.14}$$

Appendix D

Strip Theory for Ship Hydrodynamics

The theories and formulations presented in this appendix are mainly referred to the work of Salvesen et al. (1970) and Kim et al. (1980).

D.1 Added Mass and Damping Coefficient

If the ship is considered as a slender body (i.e., the beam and draft of the ship are much smaller that its length), in accordance with the variant of Stokes' theorem, the following relation for a differentiable scalar function ϕ holds:

$$\int_{S_H} n_j \frac{\partial \phi}{\partial x} dS = \int_{S_H} m_j \phi dS - \int_{C_A} n_j \phi dl, \quad j = 1, 2, \ldots, 6 \tag{D.1}$$

$$\left(n_1, n_2, n_3\right) = \boldsymbol{n}; \quad \left(n_4, n_5, n_6\right) = \left(\boldsymbol{r} - \boldsymbol{r}_G\right) \times \boldsymbol{n} \tag{D.2}$$

$$\left(m_1, m_2, m_3, m_4, m_5, m_6\right) = \left(0, 0, 0, 0, n_3, n_2\right) \tag{D.3}$$

In Eq. (D.1), the ship is assumed to have a stern transom plate with contour C_A. If the bow section is also blunt, the corresponding contour integral will be present. Additionally, the contour integral along the waterline has been ignored based on the slender assumption of the ship. By utilizing Eq. (D.1), the expression of added mass, Eq. (6.14), can be rewritten as:

$$A_{jk}(\omega) = -\frac{\rho}{\omega^2}\mathrm{Re}\left[\int_{S_H}\left(i\omega n_j - U_0 m_j\right)\phi_{\mathrm{R},k}\,dS + U_0\int_{C_A} n_j\phi_{\mathrm{R},k}\,dl\right] \qquad j,k = 1,2,\ldots,6 \tag{D.4}$$

The surface integral in Eq. (D.4) can be evaluated by integrating firstly along the contour $C(x)$ of the hull's cross section and secondly along the hull length L. Therefore,

$$A_{jk}(\omega) = -\frac{\rho}{\omega^2}\mathrm{Re}\left[\int_L\int_{C(x)}\left(i\omega n_j - U_0 m_j\right)\phi_{\mathrm{R},k}\,dl\,dx + U_0\int_{C_A} n_j\phi_{\mathrm{R},k}\,dl\right] \qquad j,k = 1,2,\ldots,6 \tag{D.5}$$

Since the hull is assumed to be a slender body, it follows that in the hull neighborhood the change of flow field in the x-direction due to the ship motion is much smaller than those in the y- and z-directions. It also follows that the component of the hull normal in the x-direction is much smaller than those in the y- and z-directions, i.e., $n_1 \ll n_2$ or n_3. Then Eq. (D.5) can be approximated as:

$$A_{jk}(\omega) = -\frac{\rho}{\omega^2}\mathrm{Re}\left[\int_L\int_{C(x)}\left(i\omega n_j^{2D} - U_0 m_j^{2D}\right)\phi_{\mathrm{R},k}^{2D}\,dl\,dx + U_0\int_{C_A} n_j^{2D}\phi_{\mathrm{R},k}^{2D}\,dl\right] \qquad j,k = 2,3,\ldots,6 \tag{D.6}$$

$$\left(n_4^{2D}, n_5^{2D}, n_6^{2D}\right) = \left[\left(y - y_G\right)n_3^{2D} - \left(z - z_G\right)n_2^{2D},\ -\left(x - x_G\right)n_3^{2D},\ \left(x - x_G\right)n_2^{2D}\right] \tag{D.7}$$

$$\left(m_2^{2D}, m_3^{2D}, m_4^{2D}, m_5^{2D}, m_6^{2D}\right) = \left(0,\ 0,\ 0,\ n_3^{2D},\ n_2^{2D}\right) \tag{D.8}$$

where $\phi_{\mathrm{R}}^{2D}(x;y,z)$ is spatial potential for the two-dimensional radiation problem at cross section x; n_2^{2D} and n_3^{2D} are, respectively, the y- and z-components of the normal of the hull's cross section.

Similarly, the damping coefficient can be calculated with the following formulation:

$$B_{jk}(\omega)=\frac{\rho}{\omega}\mathrm{Im}\left[\int_L\int_{C(x)}\left(i\omega n_j^{2D}-U_0 m_j^{2D}\right)\phi_{\mathrm{R},k}^{2D}dldx+U_0\int_{C_A}n_j^{2D}\phi_{\mathrm{R},k}^{2D}dl\right] \qquad j,k=2,3,\ldots,6 \tag{D.9}$$

Based on the slender body assumption, $\partial\phi_{\mathrm{R}}/\partial x$ and $\partial^2\phi_{\mathrm{R}}/\partial x^2$ are much smaller than their counterparts in the *y*- and *z*-directions. The three-dimensional Laplace equation (6.16) that governs the fluid motion in the hull neighborhood reduces to the two-dimensional one by dropping the high order small quantity $\partial^2\phi_{\mathrm{R}}/\partial x^2$. In order to reduce the free surface condition (Eq. (6.17)), it will be necessary to assume that $\omega \gg U_0(\partial/\partial x)$, which requires that the encounter frequency is not too low and the ship's forward speed is not too high. Under these assumptions the two-dimensional boundary-value problem for the cross-sectional radiation potential is stated as follows:

$$\frac{\partial^2\phi_{\mathrm{R},j}^{2D}(x;y,z)}{\partial y^2}+\frac{\partial^2\phi_{\mathrm{R},j}^{2D}(x;y,z)}{\partial z^2}=0, \text{ in the fluid domain} \tag{D.10}$$

$$\omega^2\phi_{\mathrm{R},j}^{2D}-g\frac{\partial\phi_{\mathrm{R},j}^{2D}}{\partial z}=0, \text{ on the undisturbed free surface } (z=0) \tag{D.11}$$

$$\frac{\partial\phi_{\mathrm{R},j}^{2D}}{\partial n}=i\omega n_j^{2D}+U_0 m_j^{2D}, \text{ on the } C(x) \text{ at mean position} \tag{D.12}$$

$$\lim_{y\to\pm\infty}\left(g\frac{\partial\phi_{\mathrm{R},j}^{2D}}{\partial y}\mp i\omega^2\phi_{\mathrm{R},j}^{2D}\right)=0 \tag{D.13}$$

D.2 Diffraction Force

To clarify the characteristic of diffraction potential, we rewrite the expressions of incident wave potential (Eqs. (6.3) and (6.4)) as follows:

$$\Phi_{\mathrm{I}}\left(x,y,z;t\right)=\mathrm{Re}\left[\phi_{\mathrm{I}}^{2D}\left(y,z\right)e^{-iK_0x\cos\varphi}e^{i\omega t}\right] \tag{D.14}$$

$$\phi_{\mathrm{I}}^{2D}\left(y,z\right)=\frac{ig\xi_{\mathrm{I}}}{\omega_0}e^{K_0\left(z+iy\sin\varphi\right)} \tag{D.15}$$

The diffraction wave depends on the incident wave; on the other hand, in the hull neighbourhood it is restricted significantly by the hull geometry. So it is reasonable to express the diffraction potential in the following form:

$$\Phi_{\mathrm{D}}\left(x,y,z;t\right)=\mathrm{Re}\left[\phi_{\mathrm{D}}\left(x,y,z\right)e^{-iK_0x\cos\varphi}e^{i\omega t}\right] \tag{D.16}$$

The influence of incident wave and hull geometry on the characteristic of Φ_{D} in the x-direction has been separated in Eq. (D.16), where $e^{-iK_0x\cos\varphi}$ and ϕ_{D} account for the contributions of incident wave and hull geometry, respectively. Substituting Eq. (D.16) into Eq. (6.2), the diffraction force is expressed as:

$$F_{\mathrm{D},j}\left(t\right)=\mathrm{Re}\left(\overline{F}_{\mathrm{D},j}e^{i\omega t}\right),\quad j=1,2,\ldots,6 \tag{D.17}$$

$$\overline{F}_{\mathrm{D},j}=-\rho\int_{S_H}\left[i\omega n_j\phi_De^{-iK_0x\cos\varphi}-U_0n_j\frac{\partial}{\partial x}\left(\phi_De^{-iK_0x\cos\varphi}\right)\right]dS,\quad j=1,2,\ldots,6 \tag{D.18}$$

By utilizing Eq. (D.1), Eq. (D.18) is further written as:

$$\overline{F}_{\mathrm{D},j}=-\rho\int_{S_H}\left(i\omega n_j-U_0m_j\right)\phi_De^{-iK_0x\cos\varphi}dS-\rho U_0\int_{C_A}n_j\phi_De^{-iK_0x\cos\varphi}dl \qquad j=1,2,\ldots,6 \tag{D.19}$$

The above surface integral is evaluated by integrating first along the contour $C(x)$ of the hull's cross section and then along the hull length L, i.e.,

$$\begin{aligned}\overline{F}_{\mathrm{D},j} &= -\rho\int_L e^{-iK_0x\cos\varphi}\left[\int_{C(x)}\left(i\omega n_j - U_0 m_j\right)\phi_D dl\right]dx \\ &\quad -\rho U_0 e^{-iK_0x\cos\varphi}\int_{C_A} n_j\phi_D dl, \qquad j=1,2,\ldots,6\end{aligned} \tag{D.20}$$

If the ship is considered as a slender body, the change of ϕ_{D} in the *x*-direction will be much smaller compared to those in the *y*- and *z*-directions. Consequently, the three-dimensional potential ϕ_{D} on contour $C(x)$ can be replaced by the sectional two-dimensional potential $\phi_{\mathrm{D}}^{2D}\left(x;y,z\right)$. The diffraction force is finally calculated by

$$\begin{aligned}\overline{F}_{\mathrm{D},j} &= -\rho\int_L e^{-iK_0x\cos\varphi}\left[\int_{C(x)}\left(i\omega n_j^{2D} - U_0 m_j^{2D}\right)\phi_D^{2D} dl\right]dx \\ &\quad -\rho U_0 e^{-iK_0x\cos\varphi}\int_{C_A} n_j^{2D}\phi_D^{2D} dl, \qquad j=1,2,\ldots,6\end{aligned} \tag{D.21}$$

Replacing $\phi_{\mathrm{D}}\left(x,y,z\right)$ in Eq. (6.6) with $\phi_{\mathrm{D}}\left(x,y,z\right)e^{-iK_0x\cos\varphi}$ and dropping the high order small quantities ($2iK_0\cos\varphi\cdot\partial\phi_{\mathrm{D}}/\partial x$ and $\partial^2\phi_{\mathrm{D}}/\partial x^2$), the three-dimension Laplace equation reduces to the two-dimensional Helmholtz equation, which can further reduce to the two-dimensional Laplace equation in the case of beam seas ($\varphi=\pi/2$ or $3\pi/2$). Replacing $\phi_{\mathrm{D}}\left(x,y,z\right)$ in Eq. (6.7) with $\phi_{\mathrm{D}}\left(x,y,z\right)e^{-iK_0x\cos\varphi}$ and assuming $\omega_0 \gg U_0\left(\partial/\partial x\right)$ yields the two-dimensional free surface condition. Similarly, the body surface condition (Eq. (6.8)) can also reduce to the two-dimensional one by applying $n_1 \ll n_2$ and $n_1 \ll n_3$. After implementing these simplifications, the two-dimensional boundary-value problem for the cross-sectional diffraction potential is obtained:

$$\frac{\partial^2\phi_{\mathrm{D}}^{2D}}{\partial y^2}+\frac{\partial^2\phi_{\mathrm{D}}^{2D}}{\partial z^2}=K_0^2\cos^2\varphi\cdot\phi_{\mathrm{D}}^{2D}, \text{ in the fluid domain} \tag{D.22}$$

$$\omega_0^2\phi_{\mathrm{D}}^{2D}-g\frac{\partial\phi_{\mathrm{D}}^{2D}}{\partial z}=0, \text{ on the undisturbed free surface } \left(z=0\right) \tag{D.23}$$

$$\frac{\partial \phi_{\mathrm{D}}^{2D}}{\partial n} = -\frac{\partial \phi_{\mathrm{I}}^{2D}}{\partial n}, \text{ on the } C(x) \text{ at mean position} \tag{D.24}$$

$$\lim_{y \to \pm\infty} \left(g \frac{\partial \phi_{\mathrm{D}}^{2D}}{\partial y} \mp i\omega^2 \phi_{\mathrm{D}}^{2D} \right) = 0 \tag{D.25}$$

D.3 5-DOF Ship Motion Equation

Since the component of surge mode can not be taken into account in the strip theory, the corresponding term should be dropped from the 6-DOF ship motion equation (Eq. (6.24)) and hence the 5-DOF equation reads:

$$\begin{aligned} &\sum_{k=2}^{6} \left\{ \left[\Lambda_{jk} + A_{jk}(\infty) \right] \dot{U}_{G,k}(t) + \int_{-\infty}^{t} K_{jk}(t-\tau) U_{G,k}(\tau) d\tau \right\} \\ &+ \sum_{k=4}^{6} \sum_{l=4}^{6} \left[\lambda_{jkl} U_{G,k} \sum_{q=4}^{6} \left(\Lambda_{lq} U_{G,q} \right) \right] = F_{\mathrm{FK+D+B+W+G},j}, \quad j = 2,3,\ldots,6 \end{aligned} \tag{D.26}$$

Appendix E

Fluid Motion Equation Described in a Non-inertial Reference Frame

A non-inertial body fixed coordinate system (BS) is illustrated in Figure E.1. It is instantaneously rotating with an angular velocity $\boldsymbol{\Omega}$ with respect to point *H* which itself is translating with velocity $\boldsymbol{U}$.

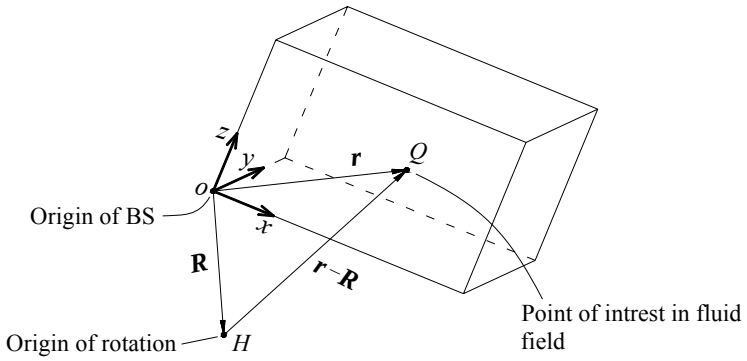

Figure E.1: Sketch of the non-inertial reference frame.

For the incompressible two-phase flow, the NS, continuity and volume fraction transport equations described in the BS are stated as follows:

$$\frac{\partial}{\partial t}\left(\rho \boldsymbol{u}\right)+\nabla\cdot\left(\rho \boldsymbol{u}\otimes \boldsymbol{u}\right)=\nabla\cdot\left(\mu\nabla\otimes \boldsymbol{u}\right)-\nabla P+\rho \boldsymbol{a} \tag{E.1}$$

$$\nabla\cdot \boldsymbol{u}=0 \tag{E.2}$$

$$\frac{\partial \alpha}{\partial t}+\nabla\cdot\left(\alpha \boldsymbol{u}\right)=0 \tag{E.3}$$

where $\boldsymbol{u}$ is the fluid velocity vector defined in the BS; gradient operator ∇ is with respect to the BS; $\boldsymbol{a}$ is the external acceleration vector; and the definitions of other symbols are identical to those in Eqs. (5.1) to (5.3).

The external acceleration, which includes the gravitational, translational and rotational accelerations, takes the following form (Ibrahim, 2005):

$$\boldsymbol{a} = \boldsymbol{g} - \frac{d\boldsymbol{U}}{dt} - \frac{d\boldsymbol{\Omega}}{dt} \times \left(\boldsymbol{r} - \boldsymbol{R}\right) - 2\boldsymbol{\Omega} \times \frac{d\left(\boldsymbol{r} - \boldsymbol{R}\right)}{dt} - \boldsymbol{\Omega} \times \left[\boldsymbol{\Omega} \times \left(\boldsymbol{r} - \boldsymbol{R}\right)\right] \tag{E.4}$$

where $\boldsymbol{r}$ and $\boldsymbol{R}$ denote the position vectors of points Q and H, respectively; $\boldsymbol{g}$ is the gravitational acceleration; the second term of the right-hand side is the translational acceleration; the third, forth and fifth terms are, respectively, angular, Coriolis and centrifugal accelerations, all of which are due to the rotational motion. It should be noticed that these accelerations are defined with respect to the BS.

Appendix F

User Manual of Developed Solver

The developed NS solver, which is based on solving the NS equations with the free surface capturing scheme, can be applied to calculate three-dimensional, time-dependent, incompressible, viscous, two-phase flow with body motion in 6-DOF. Besides its single use, the NS solver can be coupled with a seakeeping solver PROTEUS3 (PROTEUS3 user manual, 2001; Jasionowski, 2001) to predict the motion of intact/damaged ship in sea wave. The theories of the NS and the coupling solvers have been detailed in Chapters 5 and 6. This appendix will give a brief description of the codes and a tutorial for running the solver. In addition, two demonstration cases are also included.

F.1 Code Description

The code of the NS solver is written in standard *FORTRAN 90* and can be compiled with *Compaq Visual Fortran* or *Intel Visual Fortran* on the *Windows* operating system. The main subroutines of the code are summarized in Table F.1.

Table F.1: Summarization of subroutines.

Subroutine	Location	Description
Alloc	Allocate.f90	Allocate the size of arrays of global variables.
Dealloc	Deallocate.f90	Free the storage allocated for allocatable arrays.
Geo	Geo.f90	Define the global variables.
Initiate	Initiate.f90	Initiate the flow field and the body's position and orientation.

Input	Input.f90	Read information from the input file.
Main	Main.f90	Main program of the code.
Mesh_motion	Mesh_motion.f90	Calculate the motions of body and mesh vertices.
Mesh_update	Mesh_update.f90	Update the mesh information.
Momentum	Momentum.f90	Solve the momentum equations.
Monitor	Monitor.f90	Monitor the information of flow field during the computation.
Pressure	Pressure.f90	Correct the pressure and velocity field.
Readcase	Readcase.f90	Read flow field data obtained in the previous computation.
ReadGrid	ReadGrid.f90	Read grid information output from GAMBIT.
Savecase	Savecase.f90	Save flow field data for the current computation.
Savedata	Savedata.f90	Write flow field data in TECPLOT format.
SaveMesh	SaveMesh.f90	Save mesh information for the current computation.
SolverALL	Solver.f90	Manage the entire solution process.
VOF	VOF.f90	Transport the volume fraction.
UDF_bc	UDF.f90	User defined function for boundary condition.
UDF_init	UDF.f90	User defined function for initial condition.

F.2 Guide for Solver Running

F.2.1 Required Input Files

Two input files are basically needed for running the developed solver. One is the mesh file. The other is the parameter setting file which contains the solver's parameters input by the user. If the computation is run following a previous one, a case file which stores the information of previous computation is needed as well. In addition, if the computation is performed with the coupling solver (NS solver + PROTEUS3), the relevant input files for running PROTEUS3 are needed.

F.2.2 Mesh File

The mesh for computation is generated using the pre-processing software GAMBIT (GAMBIT 2.3 User's Guide, 2006). The exported mesh file contains the information of meshes and boundary types. The present NS solver supports all types of 3-D

meshes generated in GAMBIT; while it supports the boundary types of wall, velocity inlet, pressure outlet and symmetry.

F.2.3 Parameter Setting File

This file contains the general setting information of the developed solver, such as mesh input, fluid definition, selection of interpolation scheme, setting of body motion, result monitor, initialization, mesh update setting, iteration setting, etc. In the following, the function of each module will be detailed.

F.2.3.1 Solver Selection

Two solvers can be selected for simulation. If the type is set as 0, the simulation is performed solely with the NS solver. If the type is set as 1, the simulation is performed using a coupling approach (NS solver + PROTEUS3).

```
//---------------------------------//
//         Solver selection        //
// type 0: NS solver               //
//      1: NS solver + PROTEUS3    //
//---------------------------------//
 Solver type: 0
```

Figure F.1: Solver selection.

F.2.3.2 Mesh/Case Reading

If the case type is set as 0, a new computation case will be created and initialization is required before the start of simulation. If the type is set as 1, an old computation case will be loaded and be performed successively. Note that the case type should be always set as 0 when using the coupling solver (see Section F.2.3.1). The name of mesh file must be input. If an old computation case is performed, the name of case file that stores the information of previous computation is required. Additionally, the user can scale the model dimension by specifying the desired value.

```
//--------------------------------//
//        Mesh/Case reading       //
// type 0: start a new case       //
//      1: load a previous case   //
//--------------------------------//
Case type      : 0
Mesh file name : dambreak.msh
Case file name : case 0.0210s.bin
Dimension scale: 1.0
```

Figure F.2: Mesh/case reading.

F.2.3.3 Physical Property Setting

In this module, the gravitational acceleration, fluid density and viscosity for different phases can be defined.

```
//-------------------------------------------------------------------//
//                    Physical property setting                      //
//-------------------------------------------------------------------//
Gravity acceleration in x-, y- and z-direction (m/s2): 0.0 0.0 -9.81
Phase1 density   (kg/m3)                             : 1.225
Phase1 viscosity (Ns/m2)                             : 1.7894e-5
Phase2 density   (kg/m3)                             : 998.2
Phase2 viscosity (Ns/m2)                             : 0.001003
```

Figure F.3: Physical property setting.

F.2.3.4 Interpolation Scheme Selection

Three high-resolution interface-capturing schemes of VOF family, namely HRIC scheme (Muzaferija et al., 1998), modified HRIC scheme (FLUENT 6.3 User's Guide, 2006) and CICSAM scheme (Ubbink, 1997), are provided to capture the free surface. Six differencing schemes, i.e., first order upwind scheme (Versteeg and Malalasekera, 1995), central scheme (Versteeg and Malalasekera, 1995), hybrid scheme (Spalding, 1972) which switches between the first order upwind and central schemes, blending scheme (Azcueta, 2001) which blends the first order upwind and central schemes, second order upwind scheme (FLUENT 6.3 User's Guide, 2006) and QUICK scheme (Leonard, 1979), are provided to calculate the convective term in the momentum equation. The central scheme (Versteeg and Malalasekera, 1995) and PLI scheme (Panahi et al., 2006) can be used to interpolate the pressure value on

the CV faces.

```
//-------------------------------------------------//
//          Interpolation scheme selection         //
//                                                 //
// Volume fraction type 1 : original HRIC scheme   //
//                      2 : modified HRIC scheme   //
//                      3 : CICSAM scheme          //
//                                                 //
// Momentum type 1: first order upwind scheme      //
//               2: central scheme                 //
//               3: hybrid scheme                  //
//               4: blending scheme                //
//               5: second order upwind scheme     //
//               6: QUICK scheme                   //
//                                                 //
// Pressure type 1: central scheme                 //
//               2: PLI scheme                     //
//-------------------------------------------------//
 Volume fraction type: 2
 Momentum type       : 1
 Pressure type       : 1
```

Figure F.4: Interpolation scheme selection.

F.2.3.5 Iteration Setting

Two iteration methods so-called Jacobi and GMRES methods (Saad, 2003) are provided to solve the linear algebraic system. Appropriate value of relaxation factor (from 0 to 1.0) can be specified to enhance the convergence of SIMPLE algorithm. Residual error for the governing equations (5.1) to (5.3) and maximum iteration number per time step should be given. If (i) all of the residual errors fall below the given values or (ii) the iteration number exceeds the specified maximum number, the iteration for current time step stops and computation advances to the next time step.

```
//-------------------------------------------//
//              Iteration setting            //
// type 1: Jacobi method                     //
//      2: GMRES method                      //
//-------------------------------------------//
 Type of iteration method             : 2
 Relaxation factor for volume fraction : 0.7
 Relaxation factor for velocity        : 0.7
 Relaxation factor for pressure        : 0.7
 Residual error for VOF equation       : 1e-4
 Residual error for momentum equation  : 1e-4
 Residual error for continuity equation: 1e-4
 Maximum iteration number per time step: 20
```

Figure F.5: Iteration setting.

The residual errors for the volume fraction and momentum equations are defined as:

$$R_{\chi} = \frac{\sum_{nc,q} \left| \sum_{NK,nb} a_{nb} \chi_{nb} + b_q - a_q \chi_q \right|}{\sum_{nc,q} \left| a_q \chi_q \right|} \tag{F.1}$$

where *nc* is the total number of CV; and the definitions of the other symbols are identical to those in Eq. (5.14).

The definition of residual error for continuity equation reads as follows:

$$R_P = \sum_{nc,q} \left| \text{rate of mass creation in cell } q \right| \tag{F.2}$$

F.2.3.6 6-DOF Motion of Rigid Body

If the body motion is included in the simulation, the model for body motion in 6-DOF should be switched on. The mass and inertia moment of the body should be given if the body motion is unknown. Additionally, the position of mass centre and the initial linear/angular displacements of the body are required. Note that the mass and inertia moment should be specified in the input file of PROTEUS3 when using the coupling solver (see Section F.2.3.1).

```
//------------------------------------------------------------------//
//                   6-DoF motion of rigid body                     //
// switch 0: off                                                    //
//        1: on                                                     //
//------------------------------------------------------------------//
Switch of 6-DoF model                                 : 0
Body's mass (kg)                                      : 0.0
Body's inertia moment along x-, y- and z-axis (kgm2): 0.0 0.0 0.0
Position of mass centre (x,y,z) (m)                   : 0.0 0.0 0.0
Initial displacement of gravity centre (x,y,z) (m)    : 0.0 0.0 0.0
Initial orientation of body (roll,pitch,yaw) (deg)    : 0.0 0.0 0.0
```

Figure F.6: 6-DOF motion of rigid body.

F.2.3.7 Mesh Update Setting

In the NS solver, a combined dynamic mesh strategy is provided to handle the mesh

update when the body motion is included in the simulation (see Section F.2.3.6). The user can specify the frequency of mesh update, residual error for displacement of mesh vertex and maximum iteration number for the solution process. If (i) the residual error falls below the given value or (ii) the iteration number exceeds the specified maximum number, the solution process stops.

```
//-------------------------------------------------------//
//                  Mesh update setting                  //
// Note: if the following region/boundary is not defined, //
//       set the corresponding ID as "100".              //
//-------------------------------------------------------//
Interval of mesh update                 : 1
Residual error for mesh motion          : 1e-4
Maximum iteration number per mesh update: 20
ID for static boundary                  : 100
ID for region of static mesh            : 100
ID for region adopted smoothing method  : 100
ID for boundary of compartment1         : 100
ID for boundary of compartment2         : 100
```

Figure F.7: Mesh update setting.

To specify the three regions illustrated in Figure 5.1, the user should input the region/boundary ID, the information of which can be found in the mesh file, as shown in Figure F.8. The ID of compartment needs to be input in the case of using the coupling solver (see Section F.2.3.1). If the region/boundary whose ID is required to input is not created, the user should set its ID as 100.

```
(0 "Zones:")
(45 ( 2 fluid external)())
(45 ( 3 fluid neighbour)())
(45 ( 4 fluid internal)())
(45 ( 5 wall compartment)())
(45 ( 6 wall hull)())
(45 ( 7 wall tank)())
(45 ( 8 interior default-interior)())
```

ID

Figure F.8: ID information in the mesh file.

The residual error for displacement of mesh vertex ($\delta \boldsymbol{x}$) is defined as follows:

$$R_{\delta x} = \max\left\{\left|\delta \boldsymbol{x}_1^{new} - \delta \boldsymbol{x}_1^{old}\right|,\ \left|\delta \boldsymbol{x}_2^{new} - \delta \boldsymbol{x}_2^{old}\right|,\ \ldots,\ \left|\delta \boldsymbol{x}_{nv}^{new} - \delta \boldsymbol{x}_{nv}^{old}\right|\right\} \tag{F.3}$$

where superscripts new and old denote the value at the current and previous iteration steps, respectively; and subscripts 1, 2, ..., *nv* denote the serial number of mesh vertex.

F.2.3.8 Monitor Setting

The information of fluid field can be monitored during the simulation. Eight numerical sensors are provided, fours for water level measurement and fours for pressure measurement. To enable these sensors, the switch of monitor should be turned on and the positions of the sensors need to be given. Eight files recording the measured data, namely "h1.txt", "h2.txt", "h3.txt", "h4.txt", "p1.txt", "p2.txt", "p3.txt" and "p4.txt", will be output. If the model for body motion is switched on (see Section F.2.3.6), the linear and angular displacements of the body will be also recorded in the file "body_motion.txt".

```
//-------------------------------------------------------//
//                   Monitor setting                     //
// switch 0: off                                         //
//        1: on                                          //
//-------------------------------------------------------//
Switch of monitor                    : 1
Water level sensor1 (x,y,z1,z2) (m): 0.5 0.025 0.0 1.8
Water level sensor2 (x,y,z1,z2) (m): 1.5 0.025 0.0 1.8
Water level sensor3 (x,y,z1,z2) (m): 2.0 0.025 0.0 1.8
Water level sensor4 (x,y,z1,z2) (m): 2.5 0.025 0.0 1.8
Pressure sensor1 (x,y,z) (m)         : 3.22 0.025 0.1
Pressure sensor2 (x,y,z) (m)         : 3.22 0.025 0.3
Pressure sensor3 (x,y,z) (m)         : 3.22 0.025 0.5
Pressure sensor4 (x,y,z) (m)         : 3.22 0.025 0.7
```

Figure F.9: Monitor setting.

F.2.3.9 Autosave Setting

The fluid properties such as density, velocity and pressure can be saved automatically in the simulation. To enable this function, the switch of autosaving should be turned on. The frequency of file output should be given. If the switch is turned on, two files will be output. One file whose name is "*.dat" stores the fluid properties and can be opened together with the mesh file using the post-processing software TECPLOT

(TECPLOT 10 User's Manual, 2003). The other file whose name is "＊.bin" stores the information of fluid field at a specified time step and is the case file loaded by the NS solver (see Section F.2.3.2). Note that the name prefix (＊) of these two files will be automatically chosen according to the time step.

```
//-----------------------------------//
//          Autosave setting         //
// switch 0: off                     //
//        1: on                      //
//-----------------------------------//
 Switch of autosaving   : 1
 Interval of data saving: 250
 Interval of case saving: 20000
```

Figure F.10: Autosave setting.

F.2.3.10 Initialization Setting

If a new computation case is created (see Section F.2.3.2), the fluid field needs to be initialized. The initial velocity and density fields are specified according to specific test cases. If the pressure distribution is unknown, its initial value can be set as 0 Pa. For the cases with simple fluid field distribution, the user can easily initialize the fluid field by inputting information in the module. For complex cases, the user can initialize the fluid field by modifying the code in file "init.inc".

```
//-------------------------------------------------------------//
//                   Initialization setting                    //
//-------------------------------------------------------------//
 Initialize velocity (Ux,Uy,Uz) (m/s)       : 0.0 0.0 0.0
 Initialize pressure (Pa)                   : 0.0
 Region adaption for phase2 (Xmin, Xmax) (m): 0.0 1.2
 Region adaption for phase2 (Ymin, Ymax) (m): -1.0 1.0
 Region adaption for phase2 (Zmin, Zmax) (m): 0.0 0.6
```

Figure F.11: Initialization setting.

F.2.3.11 Time Step Setting

In the NS solver, the computational time step can be kept constant or adjusted automatically. For constant time step, its value needs to be input. For variable time step, its value is automatically adjusted to keep the global Courant number within the

given limit. In such a case, the first time step and limit of Courant number need to be input. The user can specify the upper and lower limits of time step to avoid using an unexpected time step for computation. If the variable time step exceeds the specified limit, the time step will be set as the limit value. Note that the time step must be kept constant when using the coupling solver (see Section F.2.3.1). The simulation terminates if one of the following two conditions is satisfied: (i) the computation step exceeds the specified number; (ii) The simulation time exceeds the specified time duration.

```
//---------------------------------//
//       Time step setting         //
// type 0: constant time step      //
//      1: variable time step      //
//---------------------------------//
Time step type       : 0
Time step (s)        : 0.001
Computation Step     : 1500
Given Courant number : 0.25
Maximum time step (s): 0.005
Minimum time step (s): 0.0005
Time duration (s)    : 3.0
```

Figure F.12: Time step setting.

F.2.4 Case File

The case file that stores the information of fluid field at a specified time step is output from the NS solver and can be loaded by the solver in later computation (see Sections F.2.3.2 and F.2.3.9).

F.2.5 Output Files

The default output file is “report.txt” which is the log of simulation. The information printed on the screen is automatically written into this file. If the switch of monitor or autosaving is turned on, relevant files will be output (see Sections F.2.3.8 and F.2.3.9).

F.3 Demos

Two simple cases are provided for users to make a start of the developed solver. The input files and computed results of the two cases can be found in a separate folder.

F.3.1 Dam Break

The first demo case is the simulation of dam break flow, as illustrated in Figure F.13. After the flap is lifted, the water flows freely. During the simulation, the water height and pressure are measured using four water height probes (H1, H2, H3 and H4) and four pressure gauges (P1, P2, P3 and P4).

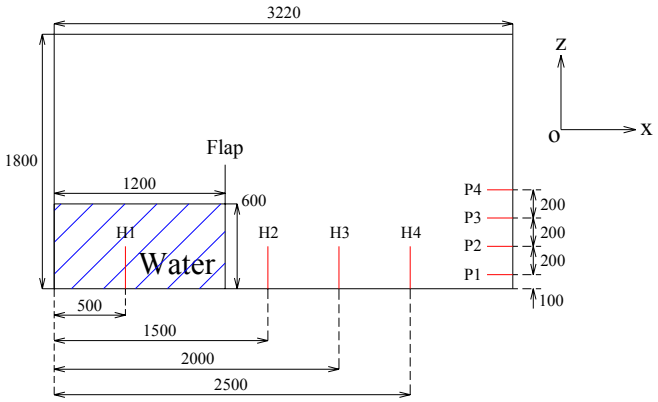

Figure F.13: A sketch of the dam break case (units: mm).

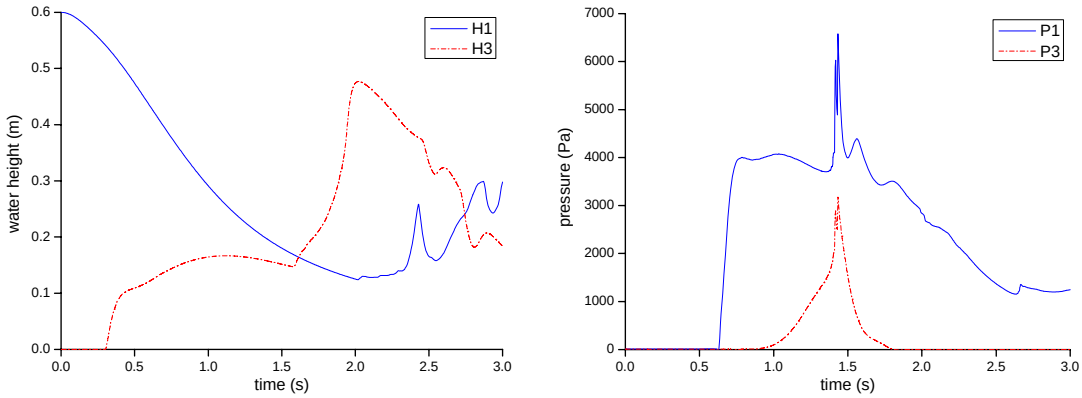

Figure F.14: Time history of water height and pressure
(Left: water height, right: pressure).

The above dam break problem is solved using the NS solver. The simulation runs up to 3.0 s. The computed water heights and pressures are shown in Figure F.14. The snapshots of the dam break process are shown in Figure F.15.

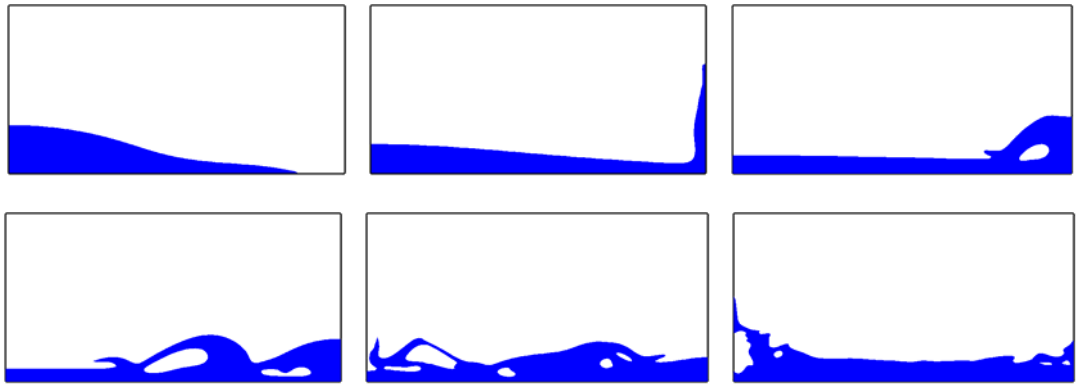

Figure F.15: Snapshots of the dam break process (t=0.5, 1.0, 1.5, 2.0, 2.5, 3.0 s).

F.3.2 Roll Decay of Ro-Ro Ferry

The second demo case is the simulation of roll decay of a Ro-Ro ferry in calm water. The main particulars and body plan of the ferry are given in Table 9.1 and Figure 9.1, respectively. A compartment located at the midship is partially filled with water, the level of which is 7.2 m above the base. The sketch of the compartment is shown in Figure F.16. The ferry is initially heeled to 5° on the starboard side. After it is loosed, the ferry freely rolls around the equilibrium position.

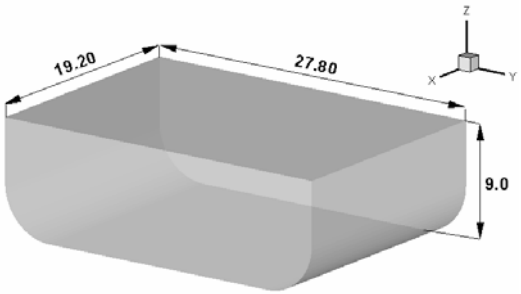

Figure F.16: Internal compartment of the ferry (units: m).

The roll motion of the ferry is simulated using the coupling solver. The motion of

water in the compartment is calculated by the NS solver, while the hydrostatic and hydrodynamic forces induced by external water are calculated using PROTEUS3. Only 4-DOF of the ferry (sway, heave, roll and pitch) is considered in the numerical simulation. The initial draft of the ferry is 7.2 m. The simulation runs up to 100 s. Figures F.17 and F.18 show the time history of roll motion and snapshots of internal water surface, respectively.

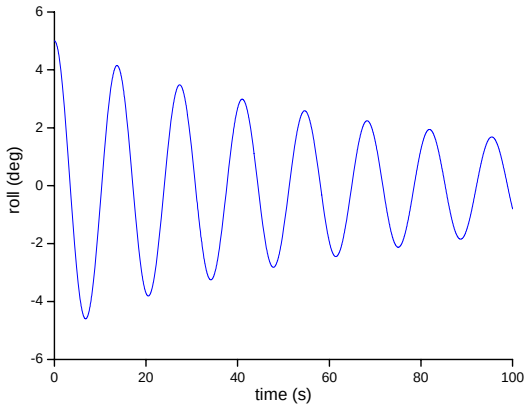

Figure F.17: Time history of roll decay motion.

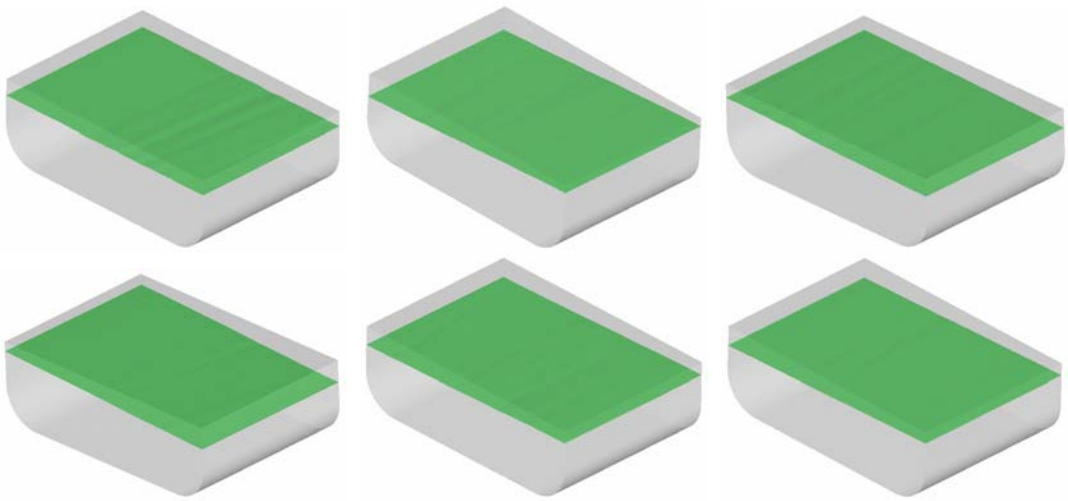

Figure F.18: Snapshots of internal water surface (t=10, 20, 30, 40, 50, 60 s).